Advances in Civil Engineering

Advanced Shotcrete Technology for Underground Engineering Support

Lead Guest Editor: Guoming Liu
Guest Editors: Lianjun Chen, Shengqiang Jiang, Cheng-Long Wang, and Agus Pulung Sasmito

Advanced Shotcrete Technology for Underground Engineering Support

Advances in Civil Engineering

Advanced Shotcrete Technology for Underground Engineering Support

Lead Guest Editor: Guoming Liu
Guest Editors: Lianjun Chen, Shengqiang Jiang, Cheng-Long Wang, and Agus Pulung Sasmito

Contents

Hindawi
Advances in Civil Engineering
Volume 2021, Article ID 2879392, 12 pages
https://doi.org/10.1155/2021/2879392

Research Article

Construction and Application Analysis of Carbon Emission Influence Factor Model of Energy Consumption in Mining Industry

Lili Wei,[1,2] **Xiwen Feng**,[1] **and Guangyu Jia**[2]

[1]*College of Energy and Mining Engineering, Shandong University of Science and Technology, the Ministry of Mine Disaster Prevention and Control Jointly Built the Cultivation Base of the State Key Laboratory, National Demonstration Center for Experimental Mining Engineering Education, Qingdao 266590, China*
[2]*School of Business, Shandong Jianzhu University, Jinan, China*

Correspondence should be addressed to Xiwen Feng; fxw6380@163.com

Received 18 October 2021; Accepted 6 December 2021; Published 29 December 2021

Academic Editor: Qian Chen

With the proposal of China's "double carbon goal," as a high energy-consuming industry, it is urgent for the mining industry to adopt a low-carbon development strategy. Therefore, in order to better provide reasonable suggestions and references for the low-carbon development of mining industry, referring to the methods and parameters of the *2006 IPCC National Greenhouse Gas Inventory Guidelines* and China's *Provincial Greenhouse Gas Inventory Preparation Guidelines (Trial)*, a carbon emission estimation model is established to estimate the carbon emission of energy consumption of China's mining industry from 2000 to 2020. Then, using the extended Kaya identity, the influencing factors of carbon emission in mining industry are decomposed into energy carbon emission intensity, energy structure, energy intensity, industrial structure, and output value. On this basis, an LMDI model is constructed to analyze the impact of five factors on carbon emission from mining industry. The research shows that the carbon emission and carbon emission intensity of energy consumption in China's mining industry first rise and then fall and then rise slightly. The carbon emission intensity in recent three years is about 2 tons/10000 yuan. The increase in output value is the main factor to increase carbon emission. The reduction in energy intensity is the initiative of carbon emission reduction. The current energy structure of mining industry is not conducive to carbon emission reduction.

1. Introduction and Literature Review

China is not only the country with the largest energy production and consumption in the world, but also the country with the largest carbon emissions [1]. Since 2006, China has been the world's largest carbon emitter, with a total carbon emission of 9.9 billion tons in 2020 [2]. In September 2020, China made a solemn commitment to the world and will strive to achieve carbon peak by 2030 and carbon neutralization by 2060 [3]. This has attracted widespread attention all over the world and further accelerated the pace of global carbon emission reduction. After China put forward the goals of "carbon peak" and "carbon neutralization," it puts forward higher requirements for China's mining carbon emission reduction and low-carbon development [4]. According to China's historical statistics, in terms of average energy consumption intensity, nonmetallic ore mining and processing industry, ferrous metal ore mining and processing industry, coal mining and processing industry, nonferrous metal ore mining and processing industry, and petroleum and gas mining industry are all high energy-consuming industries, ranking 2nd, 3rd, 7th, 11th, and 12th among 38 industrial subindustries, respectively [5]. As a high energy-consuming industry, it is of great significance to study the carbon emissions of China's mining energy consumption and the effects of its influencing factors for the green transformation and low-carbon development of mining industry.

The calculation of carbon emissions from energy consumption and its influencing factors are hot issues in recent

years [6]. At present, the carbon emission estimation method basically adopts the method, calculation formula, and basic parameters of the *2006 IPCC National Greenhouse Gas Inventory Guidelines (IPCC Guidelines* for short*)* and gives the specific estimation method in combination with the differences between countries and regions and different research objects [7]. The structural decomposition method or exponential decomposition method is mainly used to analyze the influencing factors of carbon emission [8]. Yoichi Kaya, a Japanese scholar, put forward the famous Kaya identity at an IPCC seminar, which decomposes carbon emission into the product of five factors: energy carbon emission intensity, energy structure, energy efficiency, per capita GDP, and population size, which well explains the influencing factors of carbon emission change and has been widely recognized [9]. Since then, many scholars have carried out a lot of research on the influencing factors of carbon emissions based on Kaya identity [10]. Ang et al. [11] compared the decomposition effects of various methods and found that the logarithmic mean Divisia index method can decompose multiple factors without residual [12]. Since then, this method has been widely used in the field of factor decomposition [13].

Different scholars have different influencing factors on carbon emissions in different regions [14]. Guo Chaoxian [15] believes that the expansion of economic scale is the main reason for the rapid growth of China's carbon emissions, and the reduction in energy consumption intensity makes the greatest contribution to emission reduction. Xie Shouhong et al. [16,17] have shown that technology has a significant effect on emission reduction, while the structure has a small effect on emission reduction [18]. The research on industrial carbon emissions is mainly concentrated in agriculture [19], chemical industry [20], construction [21], transportation [22], tourism [23], etc. By analyzing the relevant literature, it is found that the research on the influencing factors of carbon emission of mining energy consumption is less and not in-depth. Most studies on the types of energy consumption only consider coal, crude oil, and natural gas [24].

To more comprehensively reflect the carbon emission of mining industry, this study considers not only 19 kinds of primary energy, but also 2 kinds of secondary energy. This avoids only considering the direct carbon emissions brought by energy consumption, while ignoring the indirect carbon emissions brought by secondary energy consumption. Fully considering the particularity of carbon emission calculation of secondary energy consumption, an estimation model of carbon emission of energy consumption in mining industry is constructed. At the same time, the particularity of the mining industry is fully considered, and the influencing factors are decomposed using the extended Kaya identity. On this basis, the LMDI model is constructed to analyze the action direction and influence the effect of the five factors on carbon emission, in order to provide an accurate reference for formulating the low-carbon development strategy of the mining industry.

2. Research Methods and Data Sources

2.1. Construction of the Carbon Emission Measurement Model. Referring to the *IPCC Guidelines*, the information indicating the occurrence degree of human activities is called activity data, and the coefficients used to quantify the emissions or removals caused by unit human activities are called emission factors [25].

Therefore, the basic idea of calculating carbon dioxide emissions is that carbon emissions are the product of activity data and emission factors.

2.1.1. Activity Data. In the calculation of energy consumption of carbon emissions, the activity data are the consumption of various energy sources. Based on the principle of no emphasis and no leakage, taking into account the characteristics of energy consumption in China's mining industry, this study selects 21 kinds of energy consumption to calculate carbon emissions. This includes 19 primary energy sources and 2 secondary energy sources.

2.1.2. Emission Factor. Emission factor refers to the CO_2 emission generated by consuming unit energy, which actually refers to CO_2 emission factor here. In order to compare the consumption of different kinds of energy, this study uses standard coal equivalent for all kinds of energy units. Referring to the IPCC Guidelines, CO_2 emission factors have little to do with combustion technology. Assuming that the carbon oxidation rate in energy combustion is 100%, CO_2 emission factors mainly depend on the type of energy, that is, the carbon content of energy and the average low calorific value of energy. The low calorific value of standard coal adopted in China is 29307 kJ (7000 kcal) per kilogram of standard coal, i.e., 0.029307 TJ/*t*. Since the secondary energy consumption does not directly emit carbon dioxide, the outsourcing method is adopted to calculate the carbon emission. In this study, the secondary energy includes heat and electricity. The carbon dioxide emission of purchased heat and electricity is calculated using the emission factor of enterprise accounting carbon emission specified in China's carbon trading market. The emission factor of purchased heat is 0.11 tCO_2/GJ and the emission factor of purchased power grid is 0.6101 tCO_2/MWh [26], as shown in Table 1.

Considering the difference between primary energy and secondary energy in calculating carbon emissions, this study calculates the carbon emissions of primary energy consumption and secondary energy consumption separately and finally adds them together. The sum is the total carbon emissions of energy consumption, which is calculated using formula (1); formula (2) is used to calculate the carbon emission of primary energy consumption alone, formula (3) is used to calculate the thermal carbon emission alone, and formula (4) is used to calculate the carbon emission of electricity consumption alone. The calculation formulas are as follows:

$$T_{CO2} = T^{1}_{CO2} + T_{CO2R} + T_{CO2D}, \quad (1)$$

Table 1: Default carbon content and carbon emission factors.

Code	Energy sources	Carbon content per unit calorific value (tC/TJ)
1	Raw coal	26.37[a]
2	Cleaned coal	25.41[a]
3	Other washed coal	25.41[a]
4	Coke	29.42[a]
5	Coke oven gas	13.58[a]
6	Blast furnace gas	70.80[b]
7	Other gas	12.20[a]
8	Other coking products	29.50[a]
9	Crude oil	20.10[a]
10	Gasoline	18.90[a]
11	Kerosene	19.60[a]
12	Diesel oil	20.20[a]
13	Fuel oil	21.10[a]
14	Liquefied petroleum gas	17.20[a]
15	Refinery gas	18.20[a]
16	Naphtha	20.00[a]
17	Other petroleum products	20.00[a]
18	Natural gas	15.32[a]
19	Liquefied natural gas	17.20[a]
20	Heat	Emission factors: 0.11 tCO_2/GJ[c]
21	Electricity	Emission factors: 0.61 tCO_2/MWh[c]

[a]The data source is the *Provincial Greenhouse Gas Inventory Preparation Guidelines (Trial)* [27]. [b]The data source is the *2006 IPCC National Greenhouse Gas Inventory Guidelines* [25]. [c]The data source is the *Guidelines for Accounting Methods and Reporting of Greenhouse Gas Emissions of Enterprises* [26].

where T_{CO2} refers to the total CO_2 emission caused by all energy consumption, and the unit is tons of carbon dioxide (tCO_2); T^1_{CO2} refers to the total CO_2 emission caused by primary energy consumption, and the unit is tCO_2; T_{CO2R} refers to the total CO_2 emission caused by thermal energy consumption, in tons of carbon dioxide (tCO2); and T_{CO2D} refers to the total CO_2 emissions caused by electricity consumption, in tons of carbon dioxide (tCO_2). In this study, heat and electricity are regarded as secondary energy, and coal, petroleum, and natural gas are regarded as primary energy.

$$T^1_{CO_2} = \sum_k \sum_j E_{kj} \times H \times C_j \times O_{kj} \times \frac{44}{12}, \quad (2)$$

where T^1_{CO2} refers to the total CO_2 emission caused by primary energy consumption, and the unit is tons of carbon dioxide (tCO_2); E_{kj} refers to the consumption of the jth energy in sector k, in tons of standard coal (TCE); C_j refers to the carbon content per unit calorific value of the jth energy, in tc/TJ, as shown in Table 1; H refers to the average low calorific value of unit standard coal, i.e., 0.029307 TJ/t; and O_{kj} refers to the carbon oxidation rate of the jth energy in sector k. Here, the carbon oxidation rate of all energy in all sectors is 100% by default; 12 is the atomic weight of C, and 44 is the molecular weight of CO_2.

$$T_{CO2R} = \sum_k E_{kR} \times O_k \times RF, \quad (3)$$

where T_{CO2R} refers to the total CO_2 emission caused by thermal energy consumption, and the unit is tons of carbon dioxide (tCO_2); E_{kR} refers to the consumption of thermal energy in sector k, in tons of standard coal (tce); and RF refers to thermal emission factor of 0.11 tCO_2/GJ, as shown in Table 1.

$$T_{CO2D} = \sum_k E_{kD} \times DF, \quad (4)$$

where T_{CO2D} refers to the total CO_2 emission caused by the use of electricity, and the unit is tons of carbon dioxide (tCO_2); E_{kD} refers to the consumption of electric energy in sector k, in megawatt hours (MWh); and DF refers to electricity CO_2 emission factor of 0.6101 tCO_2/MWh, as shown in Table 1.

2.2. Constructing the Effect Model of Influencing Factors of Carbon Emission

2.2.1. Introduction of the LMDI Method. The logarithmic mean Divisia index method (LMDI method for short) is a kind of exponential decomposition method. It was proposed by Ang in 1998 to solve the original residual value and zero-value problems of exponential decomposition analysis method [11]. The LMDI method is based on the following functions:

$$L(x, y) = \frac{(x - y)}{\ln(x/y)} \quad x > 0, y > 0,$$
$$L(0, 0) = 0. \quad (5)$$

For any factorization, $C_t = X_t \times Y_t$, the associative function $L(x, y)$ has the following:

$$\begin{aligned} \triangleleft C_X &= L(C_t, C_0) In\left(\frac{X_t}{X_0}\right), \\ \triangleleft C_Y &= L(C_t, C_0) \ln\left(\frac{Y_t}{y_0}\right). \end{aligned} \tag{6}$$

Here, C represents the objective function, X and Y represent the influencing factors, X_t, Y_t, and C_t, respectively, represent the values of X, Y, and C in t period (when $t = 0$, it represents the value of base period), and $\triangle C_X$ and $\triangle C_Y$, respectively, represent the change value of C under the action of X and Y alone. By comparing $\triangle C_X$ and $\triangle C_Y$, the influence weight of X and Y on C can be obtained.

2.2.2. Construction of the LMDI Effect Analysis Model. (1) *Decomposition of Influencing Factors of Carbon Emission.* The original Kaya identity decomposes the influencing factors of carbon emission into five factors: energy carbon emission intensity, energy structure, energy efficiency, per capita GDP, and population size. Considering the particularity of mining industry as a basic industry, this study decomposes the factors affecting the carbon emission of mining energy consumption using the extended Kaya identity, which is expressed by the following formula:

$$\mathrm{C} = \sum_{\mathrm{k}} \sum_{\mathrm{j}} \frac{\mathrm{C_{kj}}}{\mathrm{E_{kj}}} \times \frac{\mathrm{E_{kj}}}{\mathrm{E_k}} \times \frac{\mathrm{E_k}}{\mathrm{GDP_k}} \times \frac{\mathrm{GDP_k}}{\mathrm{GDP}} \times \mathrm{GDP}, \tag{7}$$

where C is the carbon dioxide emission of total energy consumption, C_{kj} is the carbon dioxide emission of class j energy consumption in industry k, E_{kj} is the class j energy consumption in industry k, E_k is the energy consumption of industry k, GDP_k is the output value of industry k, and GDP is the total output value of all industries.

Also, the following are defined:

$T_{kj} = C_{kj}/E_{kj}$ is the carbon emission intensity of energy, indicating the CO_2 emission of j type energy consumed by k industry, which is related to energy production technology.

$S_{kj} = E_{kj}/E_k$ is the energy structure, indicating the proportion of j type energy consumption in total energy consumption in k industry.

$V_k = E_k/GDP_k$ is the energy intensity, indicating the energy consumption per unit output value of k industry.

$M_k = GDP_k/GDP$ is the industrial structure, indicating the proportion of k industry output value in the total output value.

$G = GDP$ is the total output value, which means the total output value of all industries.

(2) Construction of the LMDI Analysis Model. The LMDI method is used to analyze the change in carbon emission of energy consumption caused by the separate action of the above five factors. Assuming that the total carbon emission in t-1 and t period is Ct-1 and Ct, respectively, the comprehensive benefit $\triangle C$ of carbon emission is expressed as follows:

$$\Delta C = \Delta C^t - \Delta C^{t-1} = \Delta C_T + \Delta C_s + \Delta C_V + \Delta C_M + \Delta C_G. \tag{8}$$

Here, $\triangle C_T$, $\triangle C_S$, $\triangle C_V$, $\triangle C_M$, and $\triangle C_G$, respectively, represent the effects of T_{kj}, S_k, V_k, M_k, and G on carbon emission.

According to the LMDI decomposition principle, the effects of five factors on carbon emission $\triangle C_T$, $\triangle C_S$, $\triangle C_V$, $\triangle C_M$, and $\triangle C_G$ can be expressed, respectively:

$$\triangle \mathrm{CT} = \sum_{\mathrm{k}} \sum_{\mathrm{j}} \mathrm{L}\left(\mathrm{C_{kj}^t}, \mathrm{C_{kj}^{t-1}}\right) \ln\left(\frac{\mathrm{T_{kj}^t}}{\mathrm{T_{kj}^{t-1}}}\right), \tag{9}$$

$$\triangle \mathrm{CS} = \sum_{\mathrm{k}} \sum_{\mathrm{j}} \mathrm{L}\left(\mathrm{C_{kj}^t}, \mathrm{C_{kj}^{t-1}}\right) \ln\left(\frac{S_{kj}^t}{S_{kj}^{t-1}}\right), \tag{10}$$

$$\triangle \mathrm{CV} = \sum_{\mathrm{k}} \sum_{\mathrm{j}} \mathrm{L}\left(\mathrm{C_{kj}^t}, \mathrm{C_{kj}^{t-1}}\right) \ln\left(\frac{V_{kj}^t}{V_{kj}^{t-1}}\right), \tag{11}$$

$$\triangle \mathrm{CM} = \sum_{\mathrm{k}} \sum_{\mathrm{j}} \mathrm{L}\left(\mathrm{C_{kj}^t}, \mathrm{C_{kj}^{t-1}}\right) \ln\left(\frac{M_{kj}^t}{M_{kj}^{t-1}}\right), \tag{12}$$

$$\triangle \mathrm{CG} = \sum_{\mathrm{k}} \sum_{\mathrm{j}} \mathrm{L}\left(\mathrm{C_{kj}^t}, \mathrm{C_{kj}^{t-1}}\right) \ln\left(\frac{G_{kj}^t}{G_{kj}^{t-1}}\right). \tag{13}$$

2.3. Data Source and Data Processing

2.3.1. Research Object and Data Scope. The research period is 2000–2020, a total of 21 years.

The research industries are five major sectors in China's mining industry: mining and washing of coal, extraction of petroleum and natural gas, mining and processing of ferrous metal ores, mining and processing of nonferrous metal ores, and mining and processing of nonmetal ores. The reason is that the output value data of " mining of other ores" began to be counted in 2003, the output value accounted for less than 0.1%, and the terminal energy consumption accounted for less than 2%, while the "professional and support activities for mining" appeared only in 2012, and the output value accounted for a very low proportion.

Definition of energy types studied: 21 kinds of energy are considered when calculating carbon emissions. There are 28 kinds of energy in the data of terminal energy consumption after 2010 in the *China Energy Statistics Yearbook*, but the energy consumption of petroleum coke, paraffin, solvent oil, petroleum asphalt, and other energy sources is very small and can be ignored. At the same time, except coke oven gas and blast furnace gas, the remaining gas is classified as other gas, as shown in Table 1. In the LMDI analysis method, energy types are divided into four categories: coal, petroleum, natural gas, and secondary energy. Among them, coal includes raw coal, cleaned coal, other coal washing, coke, coke oven gas, blast furnace gas, other gas, and other coking products. Petroleum includes crude oil, gasoline, diesel oil,

kerosene, fuel oil, liquefied petroleum gas, refinery dry gas, naphtha, and other petroleum products. Natural gas includes natural gas and liquefied natural gas. Secondary energy includes electricity and heat.

2.3.2. Data Source. The industrial output value comes from the main business income of industrial enterprises above designated size by industry in the *China Statistical Yearbook* [28]. The reason is that the statistics of industrial output value in the whole time period is discontinuous, and because there is a certain proportional relationship between the main business income and industrial output value, the main business income is adopted for the consistency of statistical data.

The energy consumption values are all from the end energy consumption of industries in the *China Energy Statistical Yearbook* [29]. To avoid repeated calculation and unclear conversion coefficient of standard coal, the standard coal equivalent in the statistical yearbook is adopted.

2.3.3. Data Processing. In order to make the output value of different years comparable, the industry output value is subject to fixed base treatment, and the base period is based on the ex-factory price index of industrial producers of various industries in 2000.

In the analysis process using the LMDI method, the industry is divided into five industries: mining and washing of coal, extraction of petroleum and natural gas, mining and processing of ferrous metal ores, mining and processing of nonferrous metal ores, and mining and processing of nonmetal ores. Energy types are divided into four categories: coal, petroleum, natural gas, and secondary energy.

As mentioned above, according to the LMDI decomposition principle, the effects of the five factors on carbon emission ΔC_T, ΔC_S, ΔC_V, ΔC_M, and ΔC_G are specifically expressed as follows:

$$\Delta \mathrm{CT} = \sum_{k=1}^{5}\sum_{j=1}^{4} L\left(C_{kj}^{t}, C_{kj}^{t-1}\right) ln\left(\frac{T_{kj}^{t}}{T_{kj}^{t-1}}\right), \tag{14}$$

$$\Delta \mathrm{CS} = \sum_{k=1}^{5}\sum_{j=1}^{4} L\left(C_{kj}^{t}, C_{kj}^{t-1}\right) ln\left(\frac{S_{kj}^{t}}{S_{kj}^{t-1}}\right), \tag{15}$$

$$\Delta \mathrm{CV} = \sum_{k=1}^{5}\sum_{j=1}^{4} L\left(C_{kj}^{t}, C_{kj}^{t-1}\right) ln\left(\frac{V_{kj}^{t}}{V_{kj}^{t-1}}\right), \tag{16}$$

$$\Delta CM = \sum_{k=1}^{5}\sum_{j=1}^{4} L\left(C_{kj}^{t}, C_{kj}^{t-1}\right) \ln\left(\frac{M_{kj}^{t}}{M_{kj}^{t-1}}\right), \tag{17}$$

$$\Delta \mathrm{CG} = \sum_{k=1}^{5}\sum_{j=1}^{4} L\left(C_{kj}^{t}, C_{kj}^{t-1}\right) \ln\left(\frac{G_{kj}^{t}}{G_{kj}^{t-1}}\right). \tag{18}$$

3. Analysis of Calculation Results of Carbon Emissions from Energy Consumption of China's Mining Industry

According to the end energy consumption of industrial subindustries in the *China Energy Statistical Yearbook* from 2000 to 2020, combined with the carbon emission factor in Table 1, the carbon emission of mining energy consumption is calculated using formulas (1)–(4). The calculation results of total carbon emission are shown in Table 1.

From 2000 to 2016, the total carbon emission of energy consumption in China's mining industry increased first and then decreased, as shown in Figure 1. From 24.78089 million tons of carbon dioxide in 2000 to 24.78089 million tons in 2013, the emission in 2013 became the highest in history. It decreased rapidly to 37.17986 million tons in 2014, a decrease of 15.72% compared with 2013, as shown in Table 2. The whole change trend of carbon emission is consistent with the change in energy consumption. Compared with the change in carbon emission, the change in output value lags behind. The highest point of output value was 2 659 354 billion yuan in 2014, but it only decreased slightly in 2015. This may be because this study uses the main business income to replace the industrial output value. Because the market demand has not changed, the enterprise inventory makes up for the reduction in output value. In 2016, the carbon emission was 334.2 million tons, which became the lowest in history. After that, the carbon emission fluctuated slightly and rebounded to 352.1794 million tons by 2020, as shown in Figure 1.

In terms of the industrial structure of the mining industry, mining and washing of coal is the largest contributor to the carbon emission of the mining industry. Since 2003, its carbon emission has accounted for more than 40%. The second is the oil and gas exploitation industry, but the proportion fluctuates greatly. It first decreased and then increased slightly. Its proportion reached 45.37% in 2000 and decreased to 27.57% in 2020. The carbon emission of nonmetallic industry is the third, that of ferrous metal industry is the fourth, and that of nonferrous metal industry is the last, as shown in Figure 2.

The carbon emission intensity of China's mining industry generally showed a downward trend from 2000 to 2020, as shown in Figure 3. From 4.98 tons/10000 yuan in 2000 to 1.34 tons/10000 yuan in 2016, the carbon emission intensity in 2016 was the lowest in history. Compared with 2000, 2016 decreased by 73.1%, and the carbon emission intensity increased slightly after 2017. It is 2.18 tons/10000 yuan in 2020, a decrease of 41.56% compared with 3.73 tons/10000 yuan in 2005. *The National Climate Change Plan (2014-2020)* [30] puts forward the goal of reducing carbon emission intensity by 40%–45% in 2020 compared with 2005. Compared with the national target, the decline of carbon emission intensity of mining industry is still too small. From the perspective of each subindustry, the coal industry has a relatively rapid decline in carbon emission

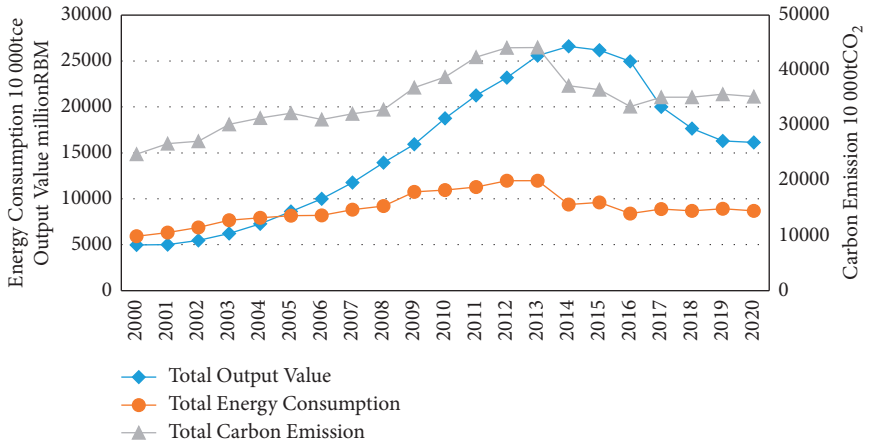

Figure 1: Total output value, total energy consumption, and total carbon emission of China's mining industry from 2000 to 2020.

Table 2: Total carbon emissions of China's mining industry from 2000 to 2020.

Year	Emission (10^4 t)
2000	24780.89
2001	26675.79
2002	27143.31
2003	30176.47
2004	31326.72
2005	32197.38
2006	31047.9
2007	32111.72
2008	32870.6
2009	36881.97
2010	38742.34
2011	42359.86
2012	44099.26
2013	44112.95
2014	37179.86
2015	36451.58
2016	33420
2017	35117.64
2018	35093.41
2019	35670.86
2020	35217.95

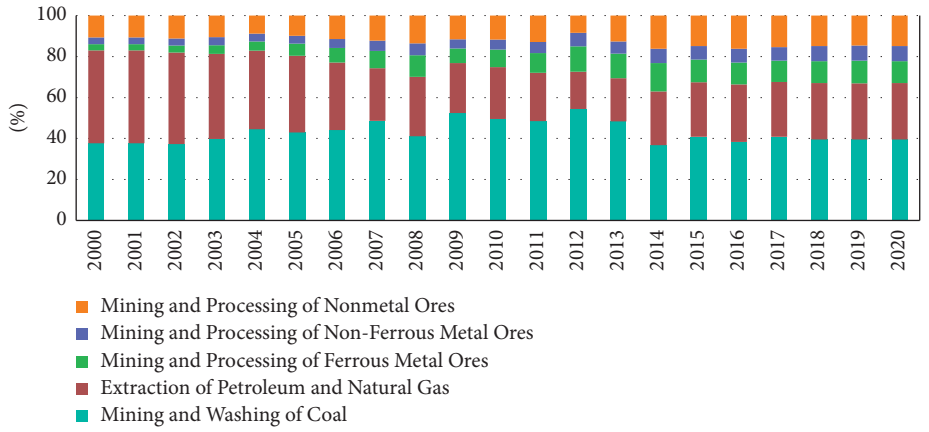

Figure 2: Analysis of the proportion of carbon emissions of various industries from 2000 to 2020.

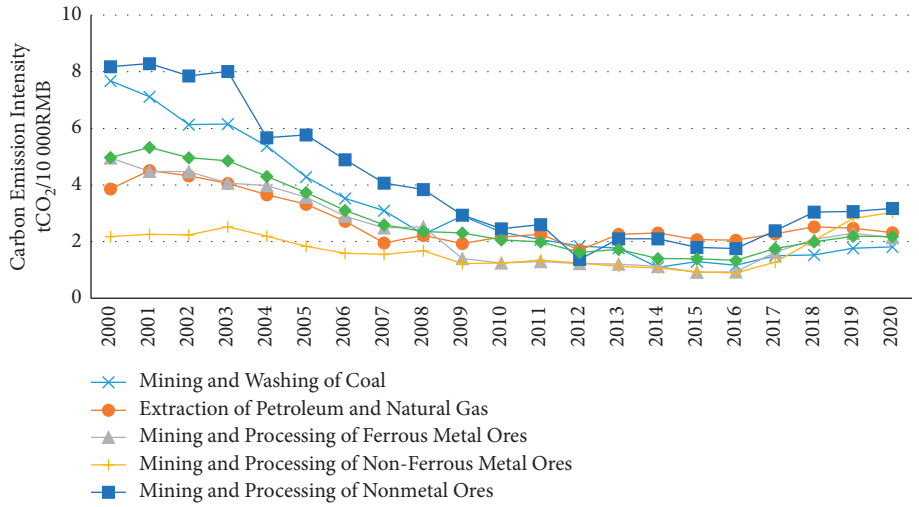

Figure 3: Carbon emission intensity of output value of various industries from 2000 to 2020.

intensity, which decreased from 768 tons/10000 yuan in 2000 to 109 tons/10000 yuan in 2014 and then rebounded to 1.8 tons/10000 yuan in 2020. The nonmetallic industry decreased from 8.18 tons/10000 yuan in 2000 to 1.37 tons/10000 yuan in 2012 and then increased to 3.17 tons/10000 yuan in 2020, becoming the industry with the highest carbon emission intensity in the mining industry. The carbon emission intensity of the nonferrous metal industry increased sharply after a slight decrease in the whole process and finally increased instead of decreasing. The change in carbon emission intensity of the petroleum and natural gas industry is the smallest, which was 3.86 tons/10000 yuan in 2000 and 2.32 tons/10000 yuan in 2020. In comparison, the petroleum and natural gas industry is the industry with the greatest pressure on emission reduction.

In this study, heat and electricity are regarded as secondary energy, and coal, petroleum, and natural gas are regarded as primary energy. According to the analysis of Figure 3, the carbon emission of secondary energy continues to increase. By 2014, the carbon emission of secondary energy exceeds that of primary energy, and the difference is becoming larger and larger. According to the statistical data of energy consumption, the proportion of secondary energy continues to increase, reaching 33.93% in 2014, exceeding the proportion of coal energy. By 2020, the proportion of secondary energy will be 39.28%. The research data show that the carbon emission intensity of secondary energy is higher than that of primary energy, as shown in Figure 4.

4. Decomposition Analysis of Carbon Emission Factors of Energy Consumption in China's Mining Industry

This study uses Stata Software to calculate the carbon emission effects of five factors according to formulas (14)–(18) in the LMDI analysis model. According to the model, the annual effect of each factor is calculated first and then the cumulative effect of each factor every year is calculated.

4.1. Factor Annual Effect Analysis. Using the LMDI method, the change in carbon emission ΔC in the current year is decomposed into the influence effects of five factors by taking the previous year as the base period. ΔC_T represents the energy carbon emission intensity, ΔC_S represents the energy structure, ΔC_V represents the energy intensity, ΔC_M represents the industrial structure, and ΔC_G represents the total output value. The calculation results are shown in Table 3.

From the annual change in total carbon emissions, annual carbon emissions increased from 2001 to 2013, except in 2006. In 2009, the highest value was increased by 40113700 tons. From 2014, carbon emissions in other years were reduced except in 2017 and 2019, as shown in Table 3. The biggest impact on carbon emissions is the output value effect and energy intensity effect. The output value effect is the driving force to increase carbon emissions. It has been a positive effect from 2002 to 2014, and the effect value has been very stable, reaching the highest value of 61.44057 million tons in 2010; the output value effect was negative from 2015 to 2020, and the highest negative effect in 2017 was -76.08057 million tons. The data show that the reduction in carbon emissions in recent five years is mainly due to the reduction in output value.

Energy intensity is the main factor to promote carbon emission reduction. From 2002 to 2016, the energy intensity effect was basically negative and stable. However, the energy intensity effect in 2017–2019 is positive, and the highest value of positive effect in 2017 is 86.9516 million tons, which reflects that the energy consumption per unit output value of mining industry has not decreased but increased in recent years. At the same time, the energy carbon emission intensity factor also has a positive effect on carbon emission reduction. The energy carbon emission intensity effect has been negative from 2001 to 2009, and the positive and negative values fluctuated frequently after 2010. The energy structure effect was basically negative before 2009 and fluctuated greatly in the later period, as shown in Figure 5. The industrial structure effect shows phased changes. The

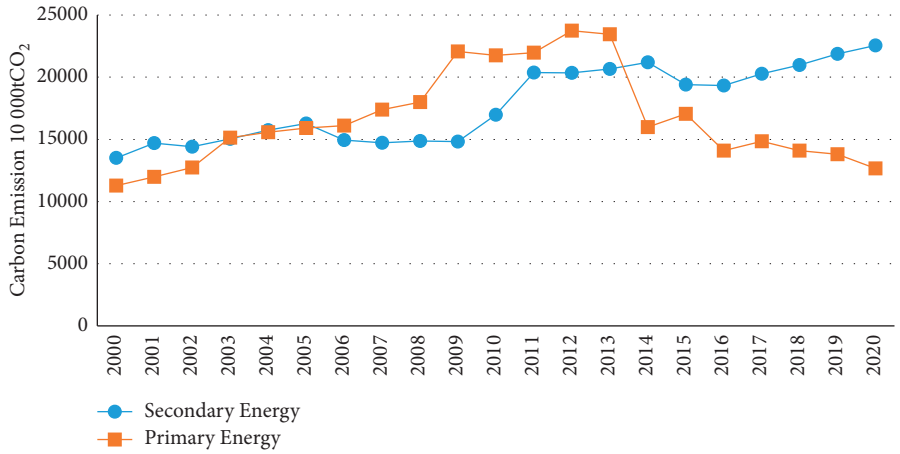

Figure 4: Carbon emissions of primary and secondary energy of China's mining industry from 2000 to 2020.

Table 3: Annual effects of various factors of carbon emission from 2001 to 2020 (10^4 t).

Year	ΔC	Δ_{CT}	ΔC_S	ΔC_V	ΔC_M	ΔC_G
2001	1894.90	−53.50	214.56	1360.03	1143.80	−1839.73
2002	467.52	−1485.03	−338.53	−351.64	274.25	2368.47
2003	3033.14	522.51	−430.01	−735.07	−8.41	3684.12
2004	1150.27	−290.43	1141.88	−5135.43	637.92	4796.33
2005	870.67	−168.64	−17.69	−4463.01	95.64	5424.37
2006	−1149.48	−161.81	−1261.55	−4622.51	269.40	4626.99
2007	1063.82	−854.29	−364.84	v3239.87	316.64	5206.19
2008	758.88	−724.83	−995.66	−3233.41	261.42	5451.35
2009	4011.37	−324.21	57.94	−374.57	−12.11	4664.32
2010	1860.37	419.86	641.49	−5340.95	−4.09	6144.06
2011	3617.52	1088.08	1109.99	−3545.36	−72.53	5037.34
2012	1739.41	−1141.27	−575.45	320.29	−586.63	3722.46
2013	13.69	−342.79	606.51	−4352.68	−233.19	4335.83
2014	−6933.09	787.18	1322.06	−10605.97	3.31	1560.33
2015	−728.29	−688.22	−437.68	348.47	625.55	−576.41
2016	−3031.58	682.62	958.66	−3329.85	296.32	−1639.33
2017	1697.64	42.92	109.99	8695.16	457.62	−7608.06
2018	−24.23	615.56	−339.89	4371.51	-294.52	−4376.88
2019	577.45	−474.16	248.95	3201.67	390.43	−2789.44
2020	−452.91	0.00	468.34	−617.55	67.40	−371.10

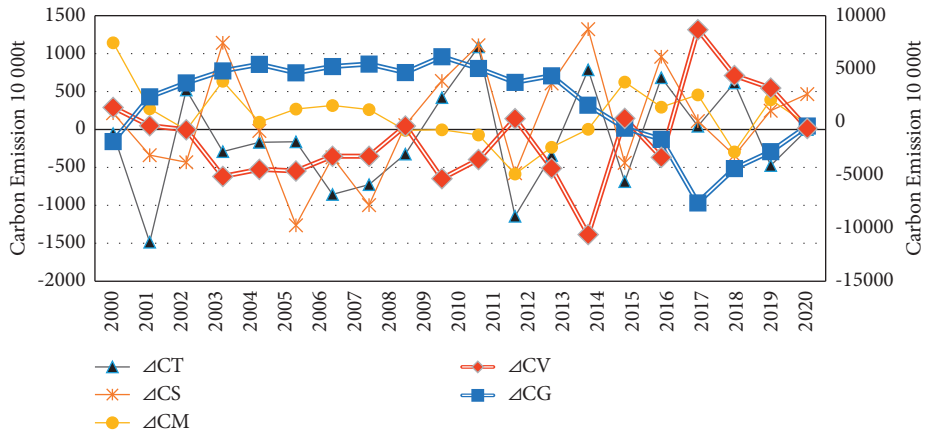

Figure 5: Annual effects of various factors on carbon emission from 2001 to 2020. Note: due to the great difference in the effect values of various factors, in order to intuitively reflect the change in the effect of various factors, the right longitudinal axis coordinates are used for ΔC_V and ΔC_G in Figure 5, and the left longitudinal axis coordinates are used for the other factors.

industrial structure effect was positive from 2001 to 2008, negative from 2009 to 2013, -2945200 tons in 2018, and positive in other years, as shown in Table 3.

4.2. Factor Cumulative Effect Analysis. Taking 2000 as the base period, the effects of various factors each year are accumulated to calculate the cumulative effects of carbon emission factors of energy consumption of China's mining industry from 2001 to 2020, as shown in Table 4. From 2001 to 2020, the cumulative value of carbon emissions increased first, then decreased, and finally reached a stable stage, as shown in Figure 6. The cumulative carbon emission in 2013 was 193.3206 million tons, which became the highest value in history, and the cumulative value decreased to 104.37006 million tons in 2020, indicating that the emission reduction effect of the mining industry in recent ten years is relatively significant.

4.2.1. Analysis of Output Value Effect. From 2001 to 2020, the cumulative value of output value effect increased first and then decreased, as shown in Figure 6. In 2014, the cumulative effect of output value was 55.18242 million tons, which became the highest value. Because the annual effect of output value in 2015–2020 was negative, the cumulative effect of output value in 2020 decreased to 37.82121 million tons, as shown in Table 4. The analysis data show that the increase in output value is the largest contributor to the increase in carbon emissions. The main measure for China's mining industry to reduce carbon emissions after 2015 is to reduce output value.

4.2.2. Analysis of Energy Intensity Effect. It can be seen from Figure 6 that the biggest contributor to the promotion of carbon emission reduction by the mining industry is energy intensity. The cumulative negative effect value of energy intensity also increased first and then decreased from 2001 to 2020. The maximum cumulative negative effect value in 2016 was −473.0154 million tons. The cumulative negative effect value of energy intensity decreased from 2017 to 2019, which proves that the energy intensity has increased in recent years. In summary, reducing energy consumption per unit output value is the key measure of sustainable emission reduction. Therefore, we must attach great importance to the increase in energy intensity.

4.2.3. Analysis of Energy Carbon Emission Intensity Effect. Energy carbon emission intensity is the second factor for the mining industry to reduce carbon emission. The cumulative negative effect of energy carbon emission intensity has steadily increased from −0.535 tons in 2001 to −35.4025 million tons in 2009. In the later stage, the cumulative negative effect has decreased slightly, and the cumulative effect will be −25.5046 million tons by 2020. Generally speaking, the cumulative effect of energy carbon emission is relatively stable. Energy carbon emission intensity is equivalent to carbon emission factor for each specific energy, and the carbon emission factor is usually fixed. Because the energy in this study is divided into four categories for analysis, each type of energy includes many specific energies, such as coal, including raw coal, washed coal, other washed coal, coke, coke oven gas, blast furnace gas, other gas, and other coking products. Therefore, when there is a change in the specific energy in the large category of energy or the improvement of energy development and production technology, it will cause the change in energy carbon emission intensity. Finally, through data research, it is considered that the impact of energy carbon emission intensity on carbon emission is very limited.

4.2.4. Analysis of Energy Structure Effect. The cumulative effect of energy structure has both positive and negative effects on carbon emissions. From 2002 to 2013, it is basically a negative cumulative effect. In 2008, the maximum negative cumulative effect was -20.5183 million tons. From 2014 to 2020, the cumulative effect is positive. In 2020, the cumulative effect of energy structure was 21.191 million tons. Overall, the effect of energy structure on carbon emission reduction is unstable, and in particular after 2009, the effect of energy structure leads to an increase in the carbon emission of mining industry. In 2009, the mining industry reduced the consumption of coal and increased the consumption of natural gas. The consumption of petroleum energy changed little, and the consumption of secondary energy increased. In 2020, the proportion of secondary energy consumption was 39.28%, exceeding the sum of coal and petroleum energy consumption, and the carbon emission of secondary energy in 2014 exceeded that of primary energy, as shown in Figures 2 and 4. It can be seen that the current energy consumption structure of the mining industry relying on increasing secondary energy does not reduce carbon emissions, but increases. Therefore, the mining industry needs to improve the current energy consumption structure to reduce carbon emissions.

4.2.5. Analysis of Industrial Structure Effect. The industrial structure is the second factor to promote carbon emission. The cumulative effect of industrial structure has been positive from 2001 to 2020 and shows an increasing trend. The cumulative effect of industrial structure increased from 11.438 million tons in 2001 to 36.2822 million tons in 2020, as shown in Table 4. In China's mining industry, coal mining and petroleum and gas mining have always accounted for a high proportion, basically reaching more than 70%, but the proportion of other industries has increased in recent ten years, and the carbon emission intensity of other industries is higher than that of the coal industry, as shown in Figure 3, so the industrial structure has always been a factor to promote carbon emission. Because the industrial structure of mining industry is greatly affected by the national macroeconomic environment, the space for industrial structure adjustment is very limited.

Table 4: Cumulative effects of various factors of carbon emission from 2001 to 2020 (10^4 t).

Year	ΔC	ΔC_T	ΔC_S	ΔC_V	ΔC_M	ΔC_G
2001	1894.90	−53.50	214.56	1360.03	1143.80	−1839.73
2002	2362.42	−1538.54	−123.96	1008.39	1418.05	528.74
2003	5395.56	−1016.03	−553.97	273.32	1409.64	4212.86
2004	6545.83	−1306.46	587.91	−4862.11	2047.56	9009.18
2005	7416.49	−1475.10	570.21	−9325.12	2143.20	14433.56
2006	6267.01	−1636.91	−691.33	−13947.64	2412.60	19060.55
2007	7330.83	−2491.21	−1056.17	−17187.51	2729.24	24266.74
2008	8089.71	-3216.04	−2051.83	−20420.92	2990.66	29718.09
2009	12101.08	−3540.25	−1993.89	−20795.49	2978.55	34382.41
2010	13961.45	−3120.39	−1352.40	−26136.44	2974.46	40526.46
2011	17578.96	−2032.31	−242.41	−29681.80	2901.93	45563.80
2012	19318.37	−3173.57	−817.85	−29361.51	2315.31	49286.26
2013	19332.06	−3516.36	−211.34	−33714.19	2082.12	53622.09
2014	12398.97	−2729.18	1110.72	−44320.16	2085.42	55182.42
2015	11670.68	−3417.40	673.04	−43971.69	2710.98	54606.01
2016	8639.10	−2734.78	1631.70	−47301.54	3007.29	52966.69
2017	10336.74	−2691.85	1741.70	−38606.38	3464.91	45358.63
2018	10312.52	−2076.30	1401.81	−34234.87	3170.39	40981.75
2019	10889.97	−2550.45	1650.76	−31033.21	3560.82	38192.31
2020	10437.06	−2550.46	2119.10	−31650.76	3628.22	37821.21

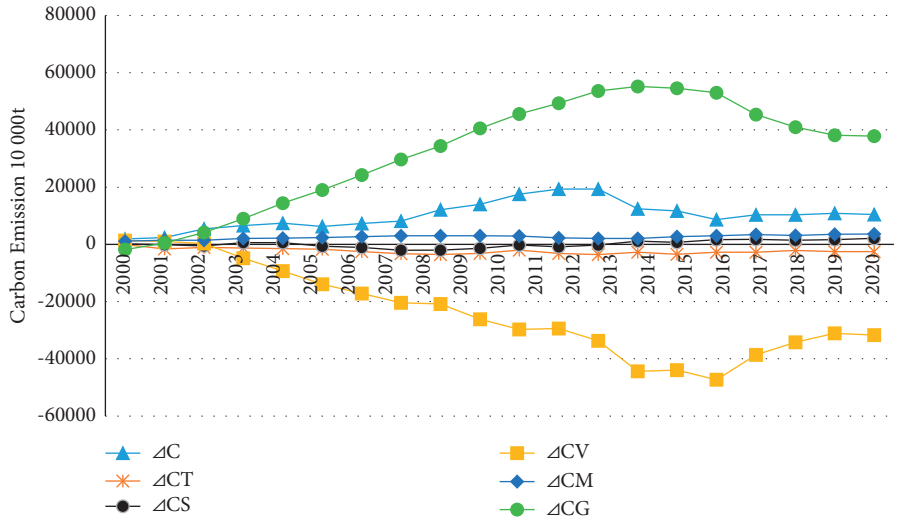

Figure 6: Cumulative effect of various factors of carbon emission from 2001 to 2020.

5. Conclusion

First, from 2000 to 2020, the carbon emissions and carbon emission intensity of energy consumption in China's mining industry increased first, then decreased, and then rebounded slightly. The carbon emission intensity of mining industry has been stable at 2 tons/10000 yuan in recent three years. In recent three years, the carbon emission intensity from high to low is nonmetallic industry, nonferrous metal industry, petroleum and gas industry, ferrous metal industry, and coal mining industry, of which the coal mining industry decreases the fastest and the carbon emission intensity of the nonmetallic industry increases instead of decreasing.

Mining and washing of coal industry is the largest contributor to carbon emission of mining industry, followed by oil and gas mining industry, nonmetallic industry is the third, ferrous metal industry is the fourth, and nonferrous metal industry is the last. From the perspective of energy structure, the carbon emission of secondary energy has always been the highest, and its carbon emission exceeded the total of primary energy in 2014. Coal consumption ranked second in carbon emissions, but it has decreased significantly since 2014. In recent three years, the carbon emission of natural gas consumption ranked third, and the emission of petroleum consumption was the least.

Second, the increase in output value is the largest contributor to the increase in carbon emissions. The cumulative effect of output value in 2014 was 551.8242 million tons, which is the highest value in the history, and the annual effect of output value from 2015 to 2020 was negative. These data show that the main means of reducing carbon emissions in China's mining industry in recent years are to reduce output value.

Third, energy intensity is the biggest driving force for carbon emission reduction. The maximum cumulative negative effect of energy intensity in 2016 was -473.0154 million tons, and the annual effect from 2017 to 2019 was positive, as shown in Table 3. This shows that the increase in energy consumption per unit output value in recent years is very unfavorable to carbon emission reduction. Reducing energy consumption per unit output value is not only an important factor in reducing carbon emissions, but also an important path for low-carbon development of mining industry.

Fourth, the effect of energy structure on carbon emission is unstable. The cumulative effect in 2020 is 21.191 million tons, indicating that the energy structure of mining industry is not conducive to carbon emission reduction in recent years; that is, increasing secondary energy consumption does not reduce carbon emission.

Fifth, energy carbon emission intensity and industrial structure have limited effect on carbon emission of mining industry, because the space for adjustment of these two factors is very limited, and their impact on carbon emission is limited.

Conflicts of Interest

The authors declare that they have no conflicts of interest.

Acknowledgments

This work was financially supported by the 13th Five-Year Plan of Educational Science in Shandong Province (Grant No. 2020ZC225) and the Shandong Social Science Planning and Research Project (Grant Nos. 17CJJJ09 and 18CJJJ25).

References

[1] World Bank, "Mineral Products for Climate Action: mineral Consumption Intensity of Clean Energy Transformation," World Bank, Washington, D.C., USA, 2020.

[2] Geological Publishing House, "Ministry of natural resources," China mineral Resources Report, pp. 15–20, Geological Publishing House, Beijing, China, 2020.

[3] First Finance and Economics, "The path, opportunities and challenges of china's "carbon Neutrality" Goal in 2060," 2020, https://www.yicai.com/news/100843313.html.

[4] H. Qiang and B. Gao, "Options for Sustainable Development of Mining Industry under the Background of Carbon Neutrality," *Natural Resources Economics of China*, vol. 4, pp. 4–11, 2021, (in Chinese).

[5] Q. Wu, "Research on the Total Factor Productivity of Mining Industry and its Influencing Factors Considering Carbon Emissions," pp. 40–45, China University of Geosciences, Beijing, China, 2017, Dissertation.

[6] K. Dong, R. Sun, G. Hochman, and H. Li, "Energy intensity and energy conservation potential in China: a regional comparison perspective," *Energy*, vol. 155, pp. 782–795, 2018.

[7] Z. Wen, Y. Wang, H. Li, Y. Tao, and D. De Clercq, "Quantitative analysis of the precise energy conservation and emission reduction path in China's iron and steel industry," *Journal of Environmental Management*, vol. 246, pp. 717–729, 2019.

[8] M. Chang, J. Zheng, Y. Inoue, X. Tian, Q. Chen, and T. Gan, "Comparative analysis on the socioeconomic drivers of industrial air-pollutant emissions between Japan and China: insights for the further-abatement period based on the LMDI method," *Journal of Cleaner Production*, vol. 189, pp. 240–250, 2018.

[9] Y. Kaya, *Impact of Carbon Dioxide Emission on GNP Growth: Lnterpretation of Proposed Scenarios .Presentation to the Energy and Lndustry Subgroup*, Response Strategies Working Group, IPCC, Paris, France, 1989.

[10] Z. Liao, "Content analysis of China's environmental policy instruments on promoting firms' environmental innovation," *Environmental Science & Policy*, vol. 88, pp. 46–51, 2018.

[11] B. Ang, F. Zhang, and K. Choi, "Factorizing changes in energy and environmental indicators through decomposition," *Energy*, vol. 23, no. 6, pp. 489–495, 1998.

[12] B. W. Ang and F. L. Liu, "A new energy decomposition method: perfect in decomposition and consistent in aggregation," *Energy*, vol. 26, no. 6, pp. 537–548, 2001.

[13] B. W. Ang, "Decomposition analysis for policymaking in energy:which is the preferred method," *Energy Policy*, vol. 32, no. 9, pp. 1131–1139, 2004.

[14] L. Shen and Y. Sun, "Review on carbon emissions, energy consumption and low-carbon economy in China from a perspective of global climate change," *Journal of Geographical Sciences*, vol. 26, no. 7, pp. 855–870, 2016.

[15] C. Guo, "Decomposition of China's carbon emissions: based on LMDl method," *China Population , Resources and Environment*, vol. 20, no. 12, pp. 4–9, 2010, (in Chinese).

[16] S. Xie, L. Wang, and Z. Shao, "Analysis on industrial difference and motivation factor of carbon emission intensity," *Research of Environmental Sciences*, vol. 26, no. 11, pp. 1252–1258, 2013.

[17] K. Li and B. Lin, "How to promote energy efficiency through technological progress in China," *Energy*, vol. 143, pp. 812–821, 2018.

[18] Y. Liu, B. Yan, and Y. Zhou, "Urbanization, economic growth, and carbon dioxide emissions in China: a panel cointegration and causality analysis," *Journal of Geographical Sciences*, vol. 26, no. 2, pp. 131–152, 2016.

[19] L. Zhiguo and L. Zongzhi, "Empirical analysis on decomposition of carbon emission factors of agricultural energy consumption in China: based on lmdl model," *Agricultural technology and economy*, no. 10, pp. 66–72, 2010.

[20] T. Fan, R. Luo, and F. fan, "Study on Influencing Factors of carbon dioxide emission from China's chemical industry," *China soft science*, vol. 27, no. 3, pp. 166–174, 2013, (in Chinese).

[21] Y. Hu and D. Chu, "Decoupling analysis of CO2 emission, output value and energy consumption of China's construction industry," *China's Population, Resources and Environment*, vol. 25, no. 8, pp. 50–57, 2015, (in Chinese).

[22] P. Yin, P. Duan, and C. Chen, "Study on carbon emission pattern of transportation and its relationship with economic growth in China," *Resources and Environment in Arid Areas*, vol. 30, no. 5, pp. 7–12, 2016.

[23] L. Jia, X. Chen, and Z. Zhang, "Carbon emission characteristics and factor decomposition of China's tourism," *Resources and Industry*, vol. 9, no. 3, pp. 67–76, 2017.

[24] Y. Fang, "Research on influencing factors of carbon emissions in China's coal production areas-based on the improved LMDI model," *Coal Economic Research*, vol. 40, no. 12, pp. 40–45, 2020.

[25] Ipcc, "IPCC Guidelines for National Greenhouse Gas Inventories," *Energy*, vol. 2, 2006.
[26] NDRC, *Guidelines for Accounting Methods and Reporting of Greenhouse Gas Emissions of Enterprises*, NDRC, Beijing, China, (in Chinese), 2021.
[27] NBSC, *Provincial Greenhouse Gas Inventory Preparation Guidelines (Trial)*, NDRC, Beijing, China, (in Chinese), 2011.
[28] NDRC, *China Energy Statistical Yearbook(2000- 2020)*, China Statistics Press, Beijing, China, (in Chinese), 2000.
[29] NBSC, *China Statistical Yearbook(2000-2020)*, China Statistics Press, Beijing, China, (in Chinese), 2000.
[30] NDRC, "National Climate Change Plan (2014-2020)," 2014, http://www.scio.gov.cn .(in Chinese).

Hindawi
Advances in Civil Engineering
Volume 2021, Article ID 8124972, 15 pages
https://doi.org/10.1155/2021/8124972

Research Article

Modeling of Tunnel Concrete Lining under Fire and Explosion Damage

Zhaopeng Yang[1], **Linbing Wang**[2] **and Zhifei Gao**[1]

[1]*National Center for Materials Service Safety, University of Science and Technology Beijing, Beijing 100083, China*
[2]*Department of Civil and Environmental Engineering, Virginia Tech, Blacksburg, VA 24061, USA*

Correspondence should be addressed to Linbing Wang; wangl@vt.edu

Received 28 September 2021; Accepted 23 October 2021; Published 13 November 2021

Academic Editor: Guoming Liu

This paper presents studies that focus on fire and explosion-induced damage of tunnel structures by employing the Discrete Element Method (DEM). By assuming a two-dimensional aggregate distribution and reconstructing the digital representation of the experimental concrete blocks, a numerical model of the tunnel lining concrete was established in the PFC^{2D} program. The temperature distribution and the shock wave pressure at the surface of the tunnel lining were obtained by using Fluent and LS-Dyna separately; the final damage simulation of concrete section under different conditions was carried out in PFC^{2D}. The results showed that PFC^{2D} cooperatively provided more accurate and effective modeling and visualization of impact damage of concrete blocks. The visualizations of damage indicated the degree of damage more clearly and more intuitively. These findings also provide a potential method for further study of the damage assessment for entire tunnel lining structures.

1. Introduction

Tunnels have special characteristics such as long longitudinal depth, few entrances and exits, and a semi-closure structure. Thus, a major accident often causes fire and explosion and subsequently leads to serious spalling and secondary disasters [1]. Previous researchers usually simulated and analysed the fire and explosion processes separately when studying the accidents in tunnels [2, 3], but in actual accidents, fire and explosion often occur simultaneously, and different degrees of collaborative damage phenomenon can be observed. Especially when vehicles transporting dangerous chemical materials crash in a tunnel, there will be much higher potential threats to the concrete lining structure of the tunnel due to fire and explosion. Therefore, it is of great significance to evaluate the damage levels of tunnel lining structure caused by both fire and explosion.

Concrete is a porous material exhibiting discontinuity, anisotropy, heterogeneity, and nonlinearity at the same time [4]. The constitutive relation based on the continuum hypothesis reflects the macro response of the system through a specific mathematical model. But this model cannot represent the essential characteristics of local discontinuity of the system, which makes it difficult for the continuum mechanics model to simulate the local instability. Especially, it is hard to describe the meso-scale damage and the discontinuous behaviours of concrete.

Considering the nature of discontinuous structure of concrete, the Discrete Element Method (DEM) provides a new idea for studying the damage behaviour of concrete in meso-scale [2]. In this work, we focus on simulating the impact damage analysis of concrete lining structure at different positions under varied temperatures, including deformation and cracking. The aim of this study was to establish the concrete block model with detailed aggregate shape in PFC^{2D}. To calibrate the different contact parameters between the clustered particles, the stress-strain curves of concrete blocks under different temperatures were evaluated in the following experiments.

2. Simulation of the Temperature Field of the Tunnel Lining Structure under Fire Condition

Simulation is the most feasible method to determine the temperature distribution of a tunnel under fire condition [5]. In this study, we established the combustion model of dangerous chemical-transporting vehicles in the computational fluid dynamics software (FLUENT) to obtain the temperature distribution at critical points of the tunnel.

2.1. The Choice of the Combustion Model and the Turbulence Model. The choice of the combustion model has a great influence on the flue gas flow field. Due to the complexity of combustion, chemical reaction, and thermal radiation, the gas turbulence will be coupled with temperature and the shape of the tunnel. For the choice of fire combustion models, previous scholars mainly adopted the PDFEBU, EDC, PPDF, SHS, and VHS models [6]. The VHS model of volume heat source was used in this study.

The most common hazardous substances in transportation are gasoline, kerosene, and other hydrocarbons. In this simulation, a methane air mixture model was selected in the combustion model, and CO_2, O_2, H_2O, and N_2 were added in the material phase. After the fluid was set as mix phase, the chemical reaction equation was set, and the full combustion was assumed in this simulation. The main flue gas products were carbon dioxide and water vapor, and the heat transfer effect of thermal radiation was considered. Since a large amount of natural gas leakage and deflagration were simulated, the turbulent visibility was not considered here.

2.2. Detailed Geometry of the Tunnel and the Boundary Conditions. The parameters of the tunnel model were referred to full-scale simulation by previous researchers [7]. The cross section size of the tunnel was approximately established as a semicircular structure with a radius of 7.5 m and a longitudinal length of 50 m. According to the fact that drivers often stop beside the wall after an accident, the whole simulation model established the fire source on the side of the tunnel for combustion ($d = 1.5$ m from the lining structure), as shown in Figure 1.

Because the tunnel has a closed and narrow tubular structure, the smoke and dust in the air will diffuse far away after combustion. Considering the critical wind speed, air flow, and the impact of real tunnel fire, this study simulated the longitudinal distance of 50 m.

2.3. Heat Release Rate (HRR). Heat release rate is one of the most important parameters in both experimental and simulative studies. The heat release curve needs to be obtained according to different conditions (vehicle size, tunnel ventilation environment, and obstacles during combustion). In highway tunnels, the mixed traffic flow is composed of cars and various heavy trucks. The fire power of a car is usually between 3 MW and 5 MW. The fire power of large vehicles transporting dangerous goods, especially oil tank trucks, often exceeds 30 MW and can reach a maximum of 100 MW [6]. We obtained the standard RABT heat release curve (GA/T 714-2007) for this simulation as this curve is suitable for the combustion of hydrocarbon materials [7]. The HRR for the RABT curve was huge at the beginning of the accident in Figure 2 as the temperature approached to 1200°C. After the explosion combustion, the oxygen content in the tunnel space dropped down dramatically and the temperature gradually decreased in the following 200 minutes.

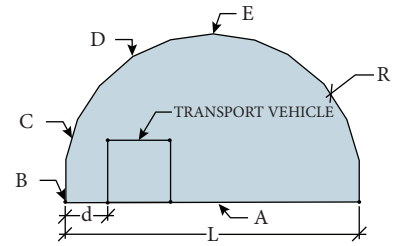

Figure 1: The separation of the tunnel cross-sections. A: the asphalt pavement; B-C: flames-continuous zone; C-D: the flame plume zone; E: the ceiling area.

2.4. Temperature Variation in Different Sections along the Longitudinal Direction. When the concrete lining structure is exposed to the high temperature generated by the vehicle fire, the temperature field inside the lining segment will change greatly and rise to varying degrees. As a thermal inert material, concrete has a large specific heat capacity (1000 J/kg-K) and small thermal conductivity (1 W/m-K), so the heat transfer in concrete is relatively slow. Concrete has obvious thermal inertia, so the heat energy requires time to penetrate the concrete lining. As the average thickness of the concrete lining structure is 500 mm, we placed the monitoring points at the middle layer to acquire the temperature inside of the concrete lining structure. The longitudinal temperature detection section was set every 5 m, and the overall detection distance was 0–30 m. The reason why we choose 30 m is that the temperature in tunnel remains relatively stable after the first 20 m. Also, we focused on the combination of explosion and temperature damage modeling and the damage dominated by the shock wave only remained 10–15 m long.

It can be seen from Figure 3, in the longitudinal temperature distribution of the tunnel, that the section with the highest temperature shown up 5 m away from the rear of the fire vehicle. Under the initial combustion conditions, the oxygen concentration was sufficient, so there was a deflagration phenomenon, and the temperature rose sharply; when the local oxygen at the fire point in the tunnel was exhausted, the combustion intensity decreased; then, the flame developed along the downstream direction of the airflow, and the corresponding maximum temperature position gradually shifted backward. When the combustion was stable, the temperature gradually increased along the longitudinal direction. The peak and stable value of the temperature at the four points illustrated in Figure 1 are recorded in Tables 1 and 2.

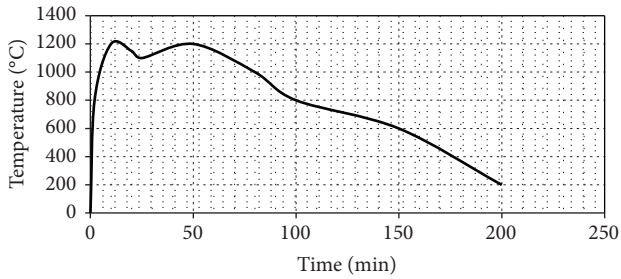

Figure 2: The temperature rise curve of tunnel fire (RABT curve).

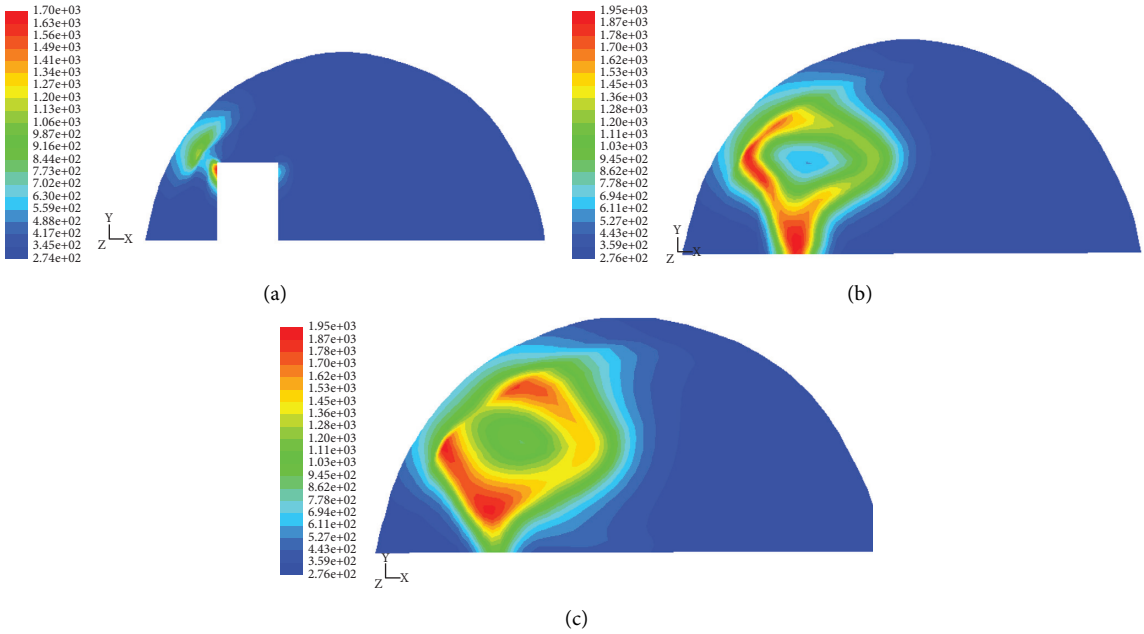

Figure 3: The temperature distribution of different sections in longitudinal direction K. (a): 0 m; (b) 15 m; (c) 30 m.

Table 1: The peak temperature inside of the tunnel lining structure after the first 20 iterations (K).

Longitudinal distance (m)	Point B	Point C	Point D	Point E
0	304	293	287	309
5	710	564.6	453	600
10	859	844	610	966
15	907	987	934	1001
20	1010	951	1293	1145
25	1004	1090	1047	1105
30	1184	1176	1105	1081

Table 2: The stable temperature inside of the tunnel lining structure after 200 iterations (K).

Longitudinal distance (m)	Point B	Point C	Point D	Point E
0	282	282	281.6	281.5
5	411	368.2	290	383
10	552	464	374	394
15	604	445	487	417
20	800	512	346	449
25	661	659	624	471
30	713	626	704	497

Most of the high-temperature regions were at the left side (points B and C) and the right side remained at the ambient temperature. The temperature increased significantly at the downstream (around 10 –5 m) of the fire scenarios. From Table 2, we could find that the maximum temperature of concrete lining at 1 m height is relatively low.

3. The Properties of the Explosion Shock Wave

The chemical explosion is a high-speed dynamic process that takes place in a very short time, and it usually takes only tens of milliseconds or even a few milliseconds from the beginning to the end [8]. Therefore, it is difficult to observe the complete process by using the traditional experimental method, and it is hard to repeat the test due to the influence of various factors. At present, the numerical simulation of tunnel explosion is an effective way to get the pressure curve.

The shock wave is produced by compressing the surrounding air. Because the deflagration and explosion process is too complex, there is no recognized pattern to follow. It is convenient for researchers to use the TNT equivalent method to predict and assess the damage of explosion [9].

3.1. Material Property and the Equation of State (EOS) in LS-Dyna. The summary of the material parameters assigned to the simulation was presented in this section. In the LS-DYNA simulation, the Jones-Wilkins-Lee (JWL) state equation is usually used to describe the relationship between pressure P and energy V per unit volume of the TNT charge. The description equation of pressure was obtained from the isentropic curve of cylinder test and the initial density change of explosive (equation (1)):

$$P = A\left(1 - \frac{\omega}{R_1 V}\right)e^{-R_1 V} + B\left(1 - \frac{\omega}{R_2 V}\right)e^{-R_2 V} + \frac{\omega E_0}{V}. \quad (1)$$

In Table 3, ρ_0 is the density of explosive, E_0 is the internal energy per unit volume of explosive, D is the velocity of explosive wave, and V is the current relative volume. A, B, R_1, R_2, and ω are the parameters of the JWL state equation, which need to be determined in experiments.

In this simulation, the air (Table 4) was simulated as a "MAT-NULL" material and was described by linear polynomial state equation.

$$P = C_0 + C_1 u + C_2 u^2 + C_3 u^3 + \left(C_4 + C_5 + C_6 u^2\right)E, \quad (2)$$

where E is the internal energy of the material, $u = \rho/\rho_0 - 1$, ρ is the current density of the air, ρ_0 is the initial density of the air, and C_1–C_6 are the parameters of the EOS of the air. The specific parameters are shown in Table 4. In order to simplify the calculation, the surrounding rock simulated in this simulation is considered as homogeneous rock-clay material.

The state equations of explosive and air were defined in the multi-material coupling element. For solid elements, the Euler Lagrange coupling method was used to calculate; the Euler grid method was used to describe air element and the Arbitrary Lagrangian Euler (ALE) algorithm was used for element calculation. Lagrange grid and Euler grid were coupled at the interface in the same analysis model, and the boundary field of material in Euler grid was defined through the transfer of mutual force. After the explosion, the shock wave firstly propagated through the fluid medium and then interacted with the lining structure and the carriageway.

3.2. The Explosion Model and Mesh Size. The size of the element will directly affect the accuracy of the computational results. Theoretically, decreasing the grid size can improve the accuracy of numerical results, but at the same time, it can also greatly improve the scale of numerical calculation thus decreasing the computational efficiency. In addition, the affected area is not very large, so it is unnecessary to divide the full-scale model into small grids when considering the influence of grids on the calculation scale.

In most traffic accidents, the explosion source was located at the side of the tunnel carriageway, and the distance between the explosion source and the lining structure was 1.5 m as, shown in Figure 4. For the concrete lining structure around the center explosion area on the left side, the size of the element unit far from the damage area was set to $100 * 200 * 100$ mm; the mesh was divided more finely, with sizes of $20 * 20 * 20$ mm, which are more conducive to obtain more accurate results.

The contact explosion was calculated by adding *LOADSEGMENT and *DEFINESEGMENT to set the equivalent mass of TNT explosive. The TNT equivalent of explosion source was set as 70 kg according to previous research [10]. The tunnel lining structure freely contacted the surrounding rock surface, and the friction and slip were ignored. The damage of lining concrete was expressed by plastic deformation when it was subjected to explosion stress. The element structure of lining concrete was deleted directly because of the failure after exceeding the plastic deformation threshold of the material.

3.3. The Mach Reflection of the Explosive Shock Wave. In real explosion scenes, the shock wave propagates freely in the air in the form of spherical wave. Regular normal reflection will occur when the shock wave front that is perpendicular to the lining structure normally contacts the lining structure; however, with the distance between the explosion center and the normal projection getting farther and farther, the incident angle will increase. When the incident angle is equal to or greater than the critical angle, the reflected wave front and the incident wave front coincide to form the shock wave along the longitudinal direction of the tunnel, and the combined shock wave is called Mach wave.

According to Figure 5, the reflection less than the distance from the explosion center $H * \tan\theta_{1C}$ belongs to normal reflection; as it gradually exceeds the regular normal reflection area, the incident angle between the incident wave and the vertical normal increases continuously, and it belongs to oblique reflection. When the incident angle becomes larger and larger, the angle between the incident wave front and the reflected wave front is smaller, and even overlaps to form a single composite Mach wave wave.

After the explosion, the shock wave expanded in a spherical shape in the center of the explosion. The main propagation mode of air was radial compression, and the shock wave first acted on the projection position of the detonation center at the arch waist. With the increasing time, the front of the shock wave became larger and the energy per unit area decreased gradually. The pressure-time curve at different points is shown in Figure 6.

When the air shock wave encountered the vertical rigid wall, the velocity of air particles on the wall instantly decreased to zero, which made the air particles within the stagnation point rapidly accumulate, and the pressure and density also increased rapidly. As shown in Figure 6, when the air shock wave contacted the rigid wall, the equivalent stress of the wall surface at different observation points increased sharply. When the explosion time was from 0.49 to 0.99 ms, the detonation of explosive had basically completed, the air was the regular positive reflection, and the tunnel lining structure facing the detonation part of the explosive formed the crushing area. When the time was from 0.99 to 13.4 ms, the detonation shape changed from the normal reflection to the Mach wave. The Mach Wave was the compressed reflected air wave, and the propagation

Table 3: TNT explosive material model and parameters of EOS.

ρ_0 (kg $*$ m^{-3})	D (ms^{-1})	A (Pa)	B (Pa)	R_1	R_2	ω	E_0 (J $*$ m^{-3})
1630	6930	$3.74 * 10^{11}$	$7.33 * 10^{9}$	4.15	0.95	0.3	$7.0 * 10^{9}$

Table 4: Air material model and parameters of EOS.

ρ_0 (kg $*$ m^{-3})	E (P_a)	C_0	C_1	C_2	C_3	C_4	C_5	C_6
$1.29 * 10^{-3}$	$2.5 * 10^{5}$	$-1 * 10^{5}$	0	0	0	0.4	0.4	0

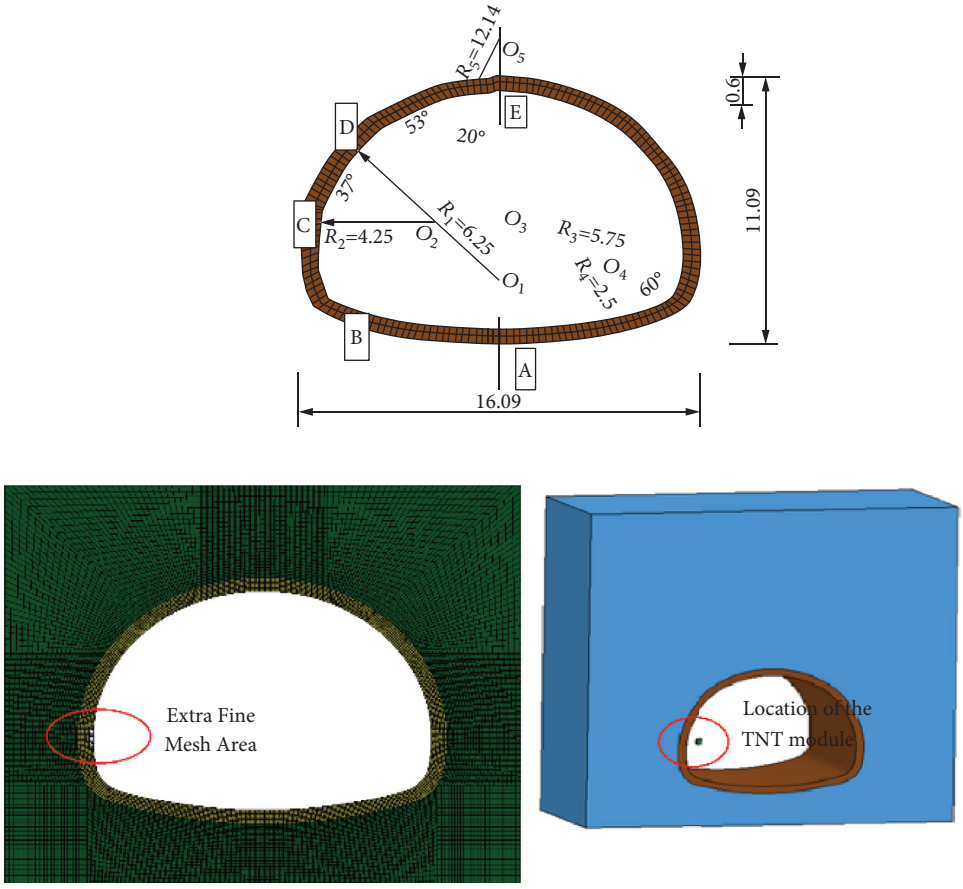

Figure 4: The geometry of the tunnel cross section and the mesh diagram.

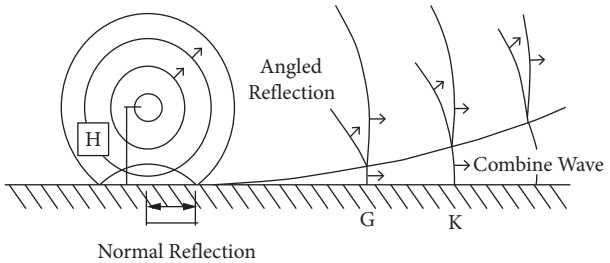

Figure 5: The schematic diagram of the generation of Mach wave reflection [10].

direction changed to the longitudinal propagation along the tunnel lining structure after the air propagated to the free surface of the tunnel lining structure. From 13.4 ms to 20 ms, the shock wave formed by the detonation had declined and the Mach wave propagating along the tunnel lining was attenuated.

4. The PFC^{2D} Numerical Model and Damage Assessment under High-Temperature Explosion Shock Wave

4.1. Information Extraction of the Concrete Aggregate Structure. The Discrete Element Method (DEM) allows the relative motion of the internal elements and does not need to meet the continuous displacement and deformation conditions. It was especially suitable for the calculation of large deformation and large displacement. In recent years, the development direction of discrete element simulation begins

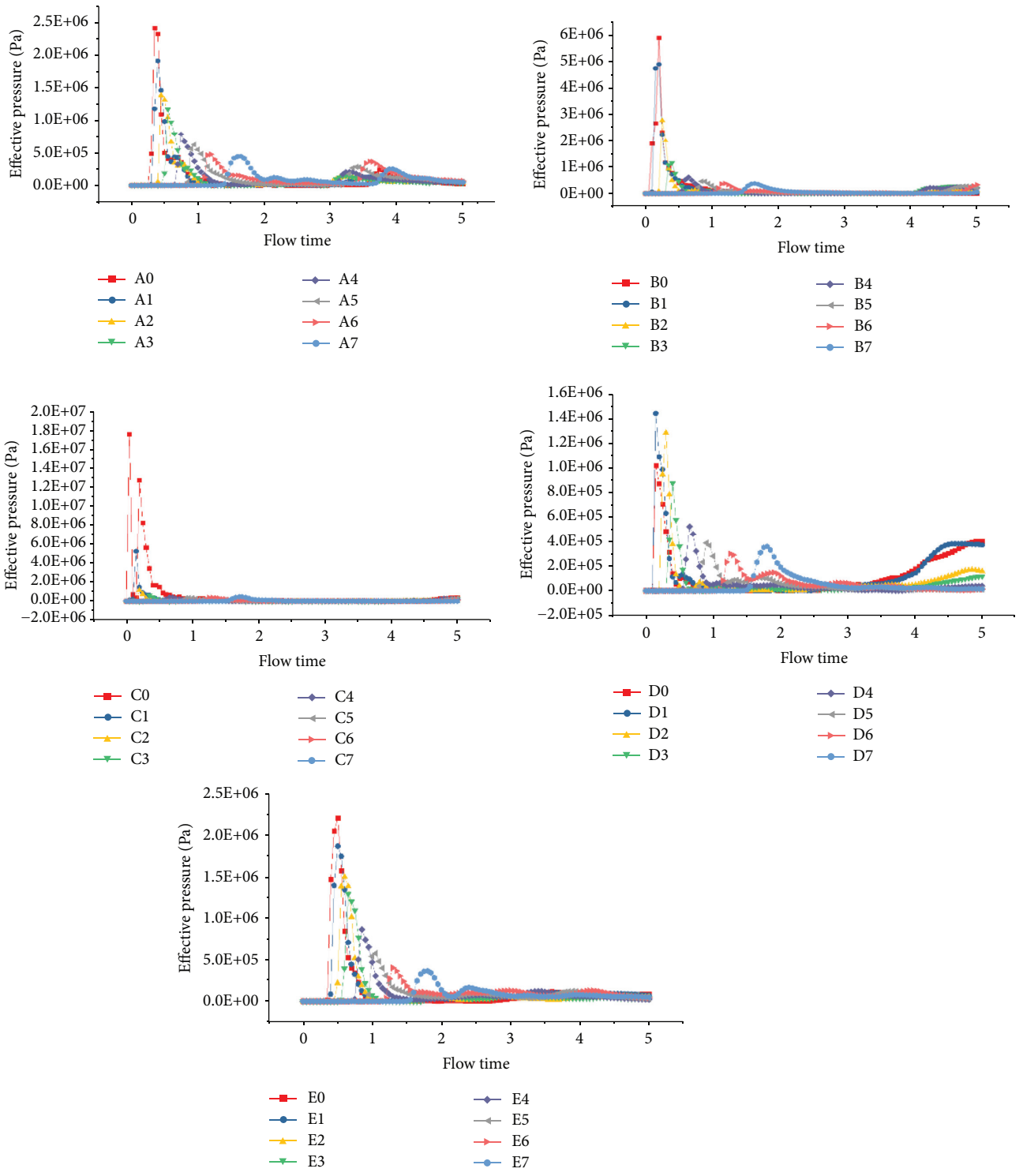

Figure 6: The compressive wave at the monitoring points A–E.

to focus on the transformation from continuous media to discontinuous media. The damage and failure of brittle materials such as concrete with many pores under dynamic load has become the research direction of many scholars [11].

Among the factors that affect the strength of concrete, the shape and distribution of the aggregate are the most important factors [12]. In DEM simulation, the treatment methods of aggregate are divided into two categories: the first is to directly simplify the aggregate into spherical or ellipsoidal particles for stacking, but it cannot simulate the enhancement of concrete strength due to the mutual connection between the aggregates; the second is to construct the polyhedral shape of aggregate, and then fill in spherical

or ellipsoidal particles. Concrete consists of cement mortar, coarse and fine aggregate, and their transition zone [13]. The aggregates in concrete present the characteristics of random distribution. In this study, the digital image processing technology was used to model the particle flow of the concrete test blocks.

The standard concrete test blocks were made in the laboratory and the cement mix parameters are shown in Table 5.

After being stored in a constant temperature conditioning chamber for 28 days, the sections with clear aggregate distribution on the side were selected for photography to generate RGB images (Figures 7–11).

The weight average method was used for the gray binarization of the RGB images. Binarization was used to distinguish the pixels representing aggregate from those representing cement mortar to give them different particle flow parameters.

The purpose of binarization is to transform the structural information of concrete blocks into the modeling information of meso structure. In binary processing, we need to select the local gray threshold T as the judgment standard. After the images were divided into several independent regions, we need to find different gray T values. If the gray level of a pixel is greater than T, it is white; if it is less than T, it is black. However, although this method can be completed automatically by MATLAB, it still needs to deal with the redundant and unreasonable details manually, such as isolated points and pseudo points.

After adopting the binary process through manual intervention and adjusting the contrast ratios, the concrete images were imported into the AutoCAD software and the sizes of the images were scaled to the size required for PFC simulation (150 mm $*$ 150 mm). The reason why this study chose 2D model in PFC is that the deformation of concrete in the longitudinal direction in each section is assumed to be zero. The 2D model also can provide a clear damage assessment of concrete structure under different compressive waves and different temperatures. The closed boundary line was drawn from the beginning to the end along the concrete aggregate edge by using the polyline.

4.2. Formation and Initial Stable State of the Aggregate Particle Clusters. In the PFC^{2D}, the basic computing element was the disk element [14]. In order to distinguish the aggregate from cement mortar, it was necessary to establish different shapes of the particle clusters. In real concrete, it was impossible to have only round particles, so the surface properties should be specified separately according to the actual situations of the aggregates. Particle clusters were independent of each other, but they influenced each other in the process of the mechanical solution. The basic disk particles in the cluster were regarded as the rigid bodies, but the disks were allowed to overlap inside the particle clusters. The irregular arrangement of particles needs to fill the gap with 2D particles in a given area and keep the overall balance of the model. In the PFC^{2D} model, the particles can be divided into regular arrangement and irregular arrangement. Regular arrangement can be used to describe the structural part of simulation, while irregular arrangement can be used to simulate solid and internally irregular granular materials.

Table 5: C30 concrete mixed ratio (kg).

Cement	Fly ash	Water	Standard sand (IOS)	Aggregate
355	85	220	334.5	1138

Figure 7: The side view of the concrete block.

Particle clusters in this simulation were divided into mortar and aggregate which are both composed of irregular particles. Although the aggregate particles were randomly arranged, the structural characteristics of the whole model will still be affected by the existence of anisotropy and weak structural planes.

When producing the aggregate model, if the proportion of the aggregate particles in PFC^{2D} is higher than the actual concrete block, the compression strength of the whole concrete model will not match with the real concrete block and raise up greatly. The aggregate characteristics are used and extracted from the real concrete sections to guarantee that the same area ration of aggregates can effectively avoid this problem [15].

There are two ways to fill particles with specific radius to achieve the required porosity. The first is to establish the boundary of the closed area, and then generate a series of noncontact particles in the closed area. Then, the required porosity can be achieved by moving the boundary. The disadvantages of this method are that the geometry of the boundary will eventually change, and that the distribution trend of the final particles will not be uniform. The second method uses the generate command and Gaussian distribution, which specify the upper and lower limits of particle radius (radius of 0.0008 and 0.001) and assign a standard deviation at the same time, and then select and generate particles. The particles were generated after the sample area size (domain extent −0.5 0.5–0.5 0.5), porosity (0.19), and particle distribution were specified.

$$R_p = \frac{V_p}{V_t} = \frac{V_t - V_a}{V_t} = 1 - \frac{V_a}{V_t}. \quad (3)$$

In equation (3), where n is the number of particles, V_p is the void area, V_t is the total area, V_a is the particle area, and the void ratio R_p is defined as the ratio of the void area to the total area. When we specified the radius and size of particles, we further used equation (4) to determine the number of particles:

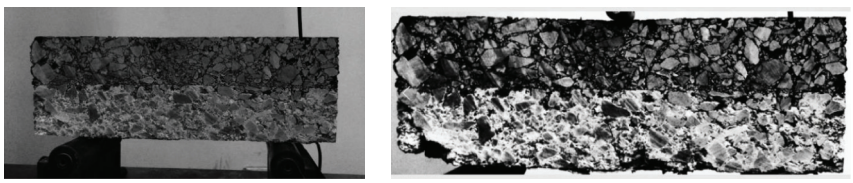

(a) (b)

Figure 8: Image before binarization (a); image after binarization (b).

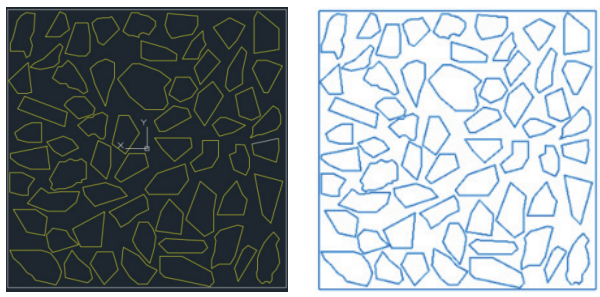

(a) (b)

Figure 9: The vector diagram of the aggregate structure in CAD (a); the aggregate structure imported into the PFC^{2D} (b).

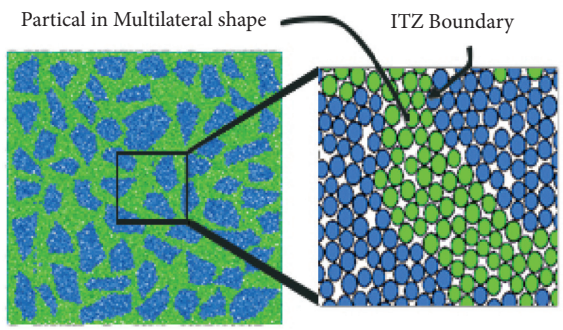

Figure 10: The blue particles are the aggregate clusters; the green particles are the filled mortar units.

(a) (b) (c) (d)

Figure 11: The uniaxial compression test with copper heating plates: (a) room temperature; (b) 100°C; (c) 200°C; (d) 300°C.

$$N = \frac{V_t(1-n)}{\pi(\overline{R})^2},$$
$$\overline{R} = \frac{R_1 + R_2}{2}, \tag{4}$$

where R_1 is the minimum particle radius (lower limit), R_2 is the maximum particle radius (upper limit), and N is the final number of particles, $\overline{R}$ is the average radius of the particles.

After the aggregate cluster and the mortar were filled, not all particles were in proper contact, which may result in errors in the calculation of the model. Therefore, it was necessary to define the contact gap as suspended particles, and the radius of these suspended particles can be expanded to meet the contact status between these particles. Finally, the combined sphere with a certain porosity was obtained, and then it was necessary to assign the contact parameters according to the concrete materials. Since the number of particles remained unchanged before and after the amplification, the amplification factor A of the particles can be obtained in equation:

$$A = \frac{\overline{R}}{\overline{R_0}} = \sqrt{\frac{1-n}{1-n_0}}, \tag{5}$$

where R_0 is the final radius of the particles.

4.3. Boundary Condition of the Particles and the Control of Wall. In PFC^{2D}, the calculation area needs to be determined first, and the modeling calculation cannot be carried out outside the calculation area [16]. The wall needs to be built at the boundary of the calculation area. The moving speed of the wall was controlled by the servo control mechanism to update the position of the base point of the wall. The wall cannot be assigned the force values directly, and only the velocity, angular velocity, and rotation center of the wall can be specified to realize the simulation of uniaxial compression. From an energy point of view, the final external energy values exerted by constant velocity loading and constant load loading are the same, so the loading speed of the standard wall is in line with the actual experimental results. In the simulation of PFC uniaxial compression, the stress of the wall was as follows:

$$\sigma_w = \frac{\sum_N F_w}{L\ d}. \tag{6}$$

F_w is the force exerted on the wall by a single particle; d is the height of the model; L is the width of the model; and N is the number of particles. The relationship between the moving speed of the wall and the stress on the wall is controlled by the parameter G.

$$\dot{u}_w = G(\sigma_w - \sigma_t) = G\Delta\sigma, \tag{7}$$

$\dot{u}_w$ is the moving speed of the wall; the contact stiffness is related to the relative displacement by the following equation:

$$F_n = n_i K_n U_n, \tag{8}$$

K_n is the normal stiffness of particles, n_i is the number of particles, and U_n is the normal displacement.

$$\Delta F_s = n_i K_s \Delta U_s, \tag{9}$$

where K_s is the tangential stiffness, and the tangential force is controlled by displacement increment.

In the process of Uniaxial Compression Test (UCT), reasonable selection of wall stiffness can increase the accuracy of simulation results [16]. If the wall stiffness is too large, the initial contact force between particles will be too large, which increases the time for the model to achieve the initial equilibrium; if the wall stiffness is too small, particles will pass through the wall and the simulation fails. It is reasonable to set the wall stiffness as 10 times of the particle stiffness according to previous studies [15].

4.4. The Calibration of the Particle Contact Parameters of the Concrete Blocks at Different Temperatures. It was necessary to calibrate the particle contact parameters of the PFC^{2D} model before the explosion impact simulation. In our model, the aggregation of particles bonded together by the pb-bonding model. For the concrete structure, its compressive strength, shear strength, and other macro mechanical properties can only be determined by defining the interaction between circular particles [17]. PFC^{2D} provides two methods for value assignment: the first is direct assignment and the second is indirect assignment. It includes effective modulus (e-mod), normal shear stiffness ratio ($\underline{k}_{\text{ratio}}$), radius multiplier (Pb radius), friction coefficient (fric), and so on. In order to study the damage of concrete under different temperatures and blast waves more effectively, the second method was used in this study. The mechanical parameter between particles in the parallel bond model can only be determined by repeated calibration in the simulation process when the simulated stress-strain curve matches the experimental one.

After the concrete test blocks were prepared in the laboratory, the universal hydraulic testing machine in the laboratory was equipped with upper and lower temperature-control copper plates to adjust and control the temperature. The uniaxial compression of the same batch of concrete blocks which take the PFC^{2D} aggregate model was tested at room temperature, 100°C, 200°C, and 300°C. The reason why we chose 300°C as the maximum test temperature is because the concrete block will be considered totally broken after this boundary, and it is unnecessary to consider the shock wave bearing capability of these types of concrete blocks. In order to keep the temperature of uniaxial compression within the specified range, it is necessary to stick high-temperature insulation cotton (black color) around the concrete blocks.

In order to ensure the accuracy of the experiment, three groups of experiments using the same batch were carried out for each test block. As a kind of thermal inert material, the thermal conductivity of concrete is poor, so it is necessary to keep the heating time at 2 hours to ensure that the whole concrete test block reaches the preset temperature before the uniaxial compression. When the concrete was damaged under compression, the side spalling was obviously

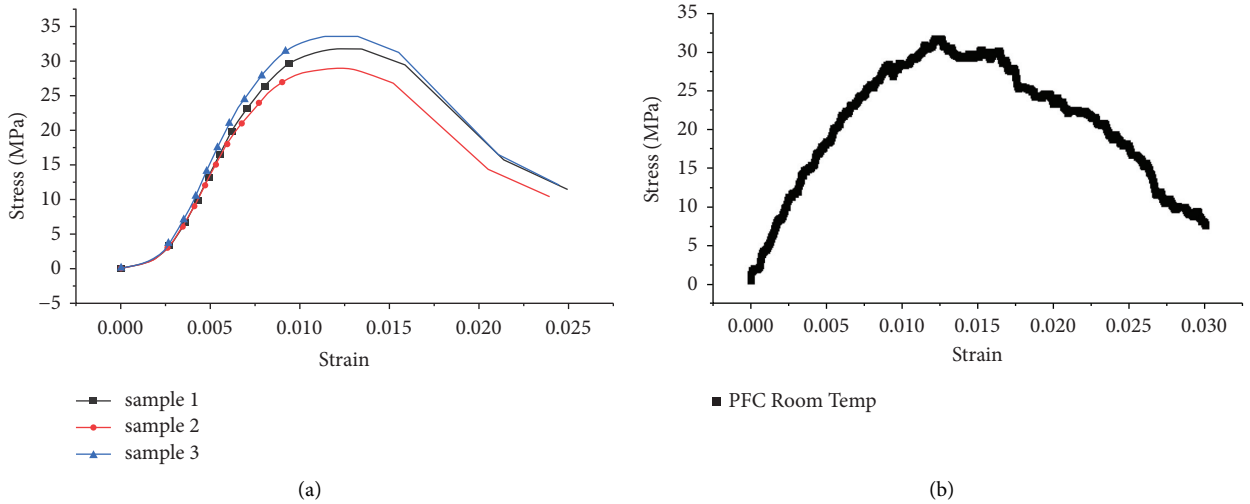

Figure 12: The concrete UCT stress-strain curves at room temperature: (a) the experiment results and (b) the PFC^{2D} result.

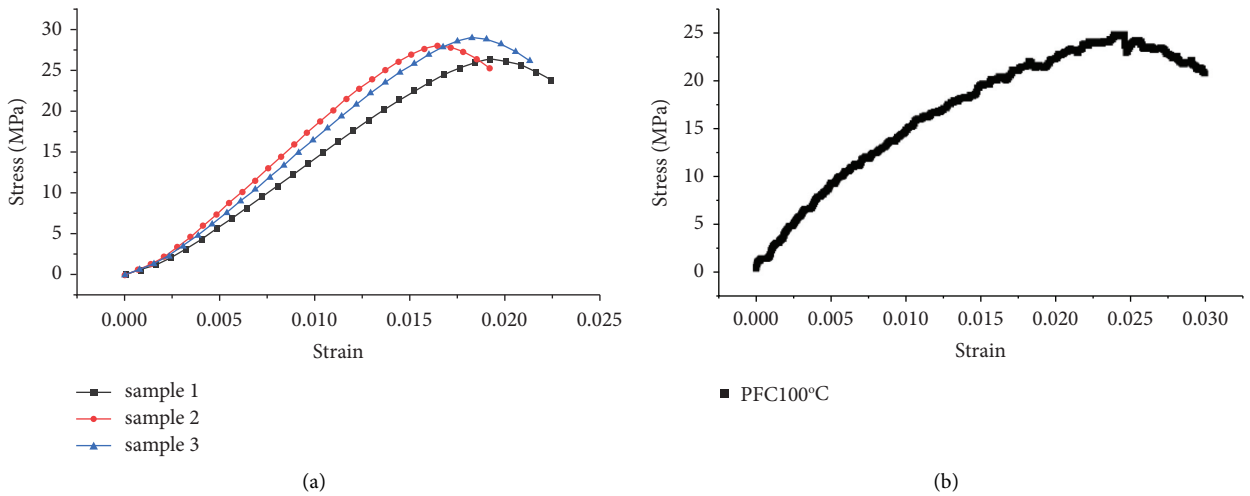

Figure 13: The concrete UCT stress-strain curves at 100°C: (a) the experiment results and (b) the PFC^{2D} result.

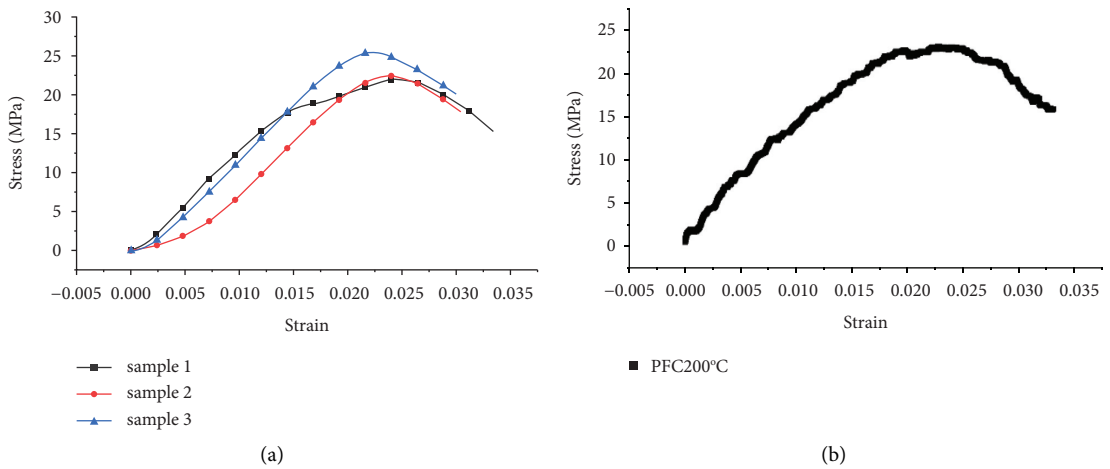

Figure 14: The concrete UCT stress-strain curves at 200°C: (a) the experiment results and (b) the PFC^{2D} result.

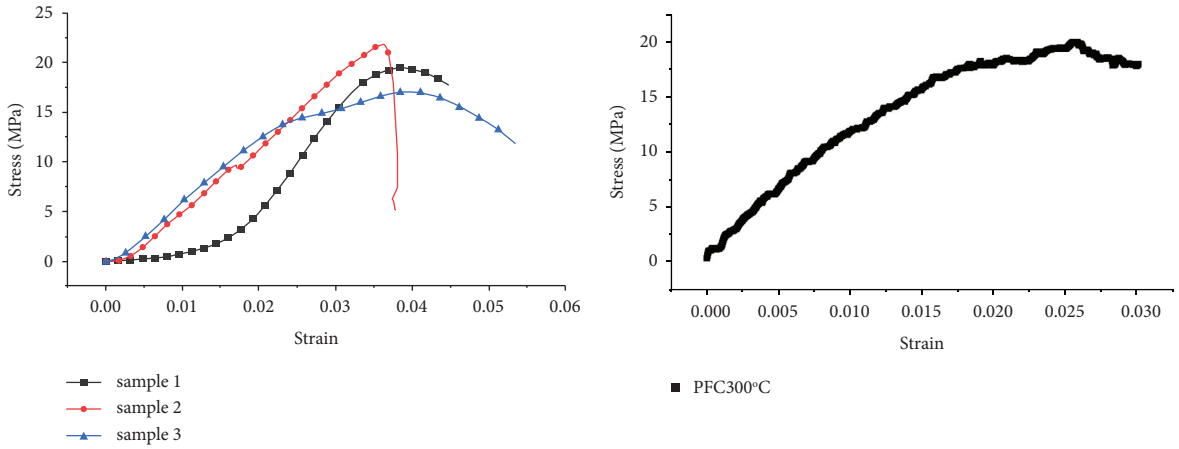

Figure 15: The concrete UCT stress-strain curves at 300°C: (a) the experiment results and (b) the PFC^{2D} result.

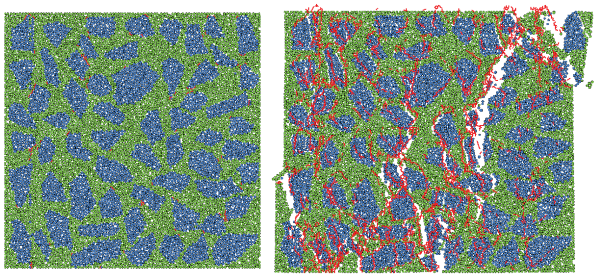

Figure 16: The initial and final figure of UCT in PFC^{2D}.

observed, and the main crack spread through the test block. Shear failure was the main failure mode in numerical simulation as well as uniaxial compression of concrete. The stress-strain curve was recorded for each set of concrete test sample (Figures 12–15).

The UCT results simulated by PFC^{2D} manifested that the deformation and slip of the mortar particles (ball-ball) and aggregates (clump) in the model were obvious during the damage, and the internal crack progression from the opening to the end through the damage can be clearly detected. At the initial stage of loading, due to the small stress, micro cracks appeared around some particles and they mainly existed at the interface between cement matrix and coarse aggregate. When micro cracks appeared between particles, stress redistribution occurred in the whole concrete blocks, and stress concentration was prone to form around the cracks, which leads to the continuous expansion of cracks. As the loading continued, the initial interface cracks gradually extended and widened, new cracks appeared in other aggregate interfaces, and the cracks gradually connected with each other. When the concrete specimen reached the maximal loading, the particle displacement increased obviously, and many macro cracks appeared between particles. As the macro cracks continued to expand, the bearing capacity of residual concrete gradually decreased, and oblique cracks formed between adjacent cracks (Figure 16).

It should be further noted that the meso parameter of the numerical model established by PFC cannot be directly equal to the macro parameter of the real material. The main reason is that the effective modulus and Poisson's ratio obtained by indirect characterization methods are not equivalent to the actual elastic modulus and Poisson's ratio, but they are indeed positively correlated. Based on the comparison of the numerical simulation and the laboratory tests, the digital model is in good agreement with the final failure mode, which indicates the rationality of the calibration parameters.

During the calibration process, the ball-ball contact parameters need to be adjusted continuously. After the stress-strain intensity curves of the test blocks were obtained from the control experiments, the calibrated stress-strain curves at different temperatures were obtained. For the three different temperatures, the key contact parameters of concrete mortar and aggregate in the ball-ball bond model were recorded, respectively, as shown in Tables 6 and 7.

Two parameters (e_mod and pb_emod) were used to characterize the elastic modulus, and k_ratio was used to characterize the Poisson's ratio; between the particles, pb_coh is the cohesive force, pb_fa is the friction angle, and fric is the friction coefficient.

In our calibration process, the internal coefficient of aggregate was kept unchanged, and the stress-strain capacity of concrete block was changed by varying the friction

Table 6: Contact parameters of particles in the mortar area.

	Emod	k_{ratio}	Pb-emod	Pb-kratio	Pb-ten	Pb-coh	Pb-fa	Fric
Ambient temp.	$5.00E+07$	1.3	$5.00E+07$	1.3	$4.00E+06$	$1.30E+07$	$3.40E+01$	$5.00E-01$
100°C	$2.00E+07$	1.3	$2.00E+07$	1.3	$3.00E+06$	$1.00E+07$	$3.40E+01$	$5.00E-01$
200°C	$1.50E+07$	1.3	$1.50E+07$	1.3	$2.00E+06$	$8.00E+06$	$3.40E+01$	$5.00E-01$
300°C	$6.00E+06$	1.3	$6.00E+06$	1.3	$4.50E+05$	$1.25E+06$	$3.40E+01$	$3.00E-01$

Table 7: Contact parameters of particles in the aggregate cluster.

	Emod	k_{ratio}	pb-emod	pb-kratio	pb-ten	pb-coh	pb-fa	Fric
Ambient temp.	$5.00E+09$	1.3	$5.00E+09$	1.3	$5.00E+06$	$2.0E+07$	$5.80E+01$	$5.00E-01$
100°C	$5.00E+09$	1.3	$5.00E+09$	1.3	$5.00E+06$	$2.00E+07$	$5.80E+01$	$5.00E-01$
200°C	$5.00E+09$	1.3	$5.00E+09$	1.3	$5.00E+06$	$2.00E+07$	$5.80E+01$	$5.00E-01$
300°C	$5.00E+09$	1.3	$5.00E+09$	1.3	$5.00E+06$	$2.00E+07$	$5.80E+01$	$5.00E-01$

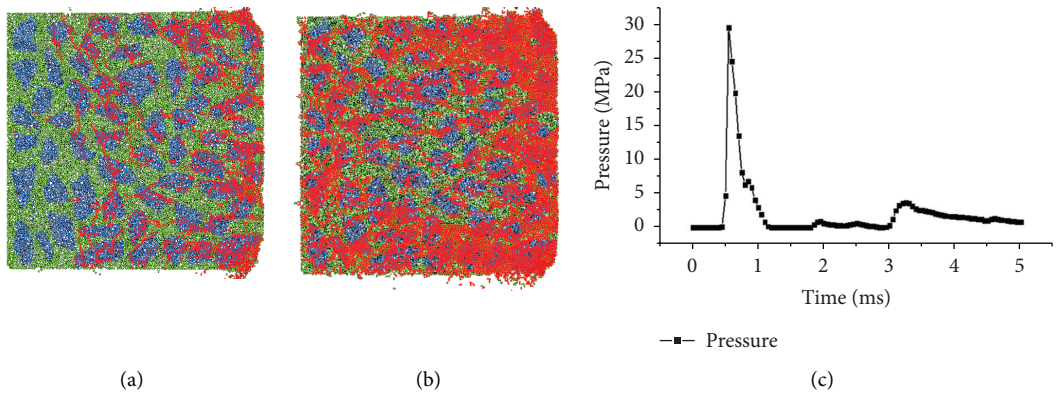

Figure 17: (a) The damage of point B0 at normal temperature, (b) the damage of point B0 at 400 K, and (c) the compressive wave.

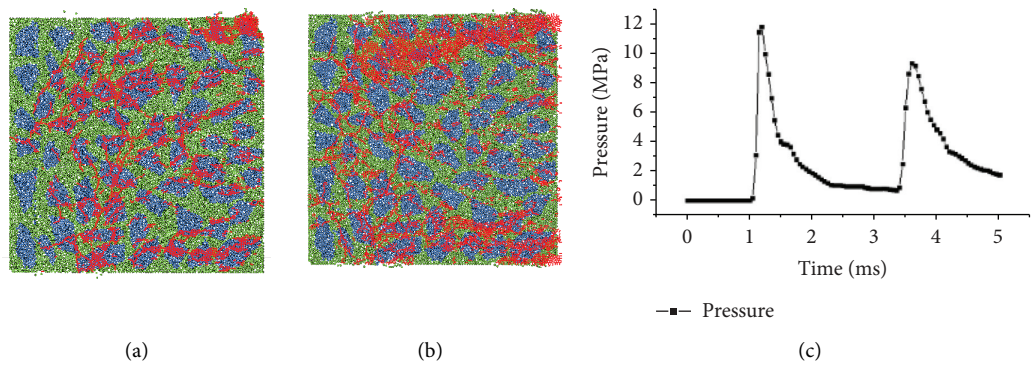

Figure 18: (a) The damage of point B4 at normal temperature, (b) the damage of point B3 at 500 K, and (c) the compressive wave.

coefficient and cohesion between the particles in cement mortar. The uniaxial compression model was set up in PFC^{2D} to calibrate the concrete blocks at different temperatures and the output curve was compared with our experiment results in Figures 12–15.

4.5. Explosion Impact Simulation of Concrete Blocks in PFC2D with Variant Temperatures. The insensibility of the temperature in the concrete lining structure has been classified into three groups (100°C, 200°C, 300°C). After equal sampling of the compressive wave curve, 100 data points were generated and incorporated into PFC^{2D} for impact loading. Combining it with the temperature distribution, at the first 5–15 m, the compressive pressure was relatively high and the temperature gradually increased from the ambient temperature to over 900°C (most of the downstream ceiling). Several critical points were studied to compare the mesoscale explosion damage with and without the variant temperatures (Figures 17–19).

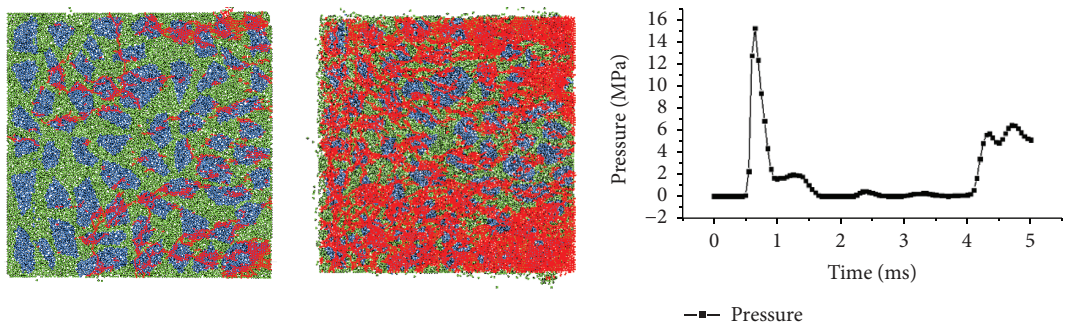

Figure 19: (a) The damage of point D0 at normal temperature, (b) the damage of point D0 at 500 K, and (c) the compressive wave.

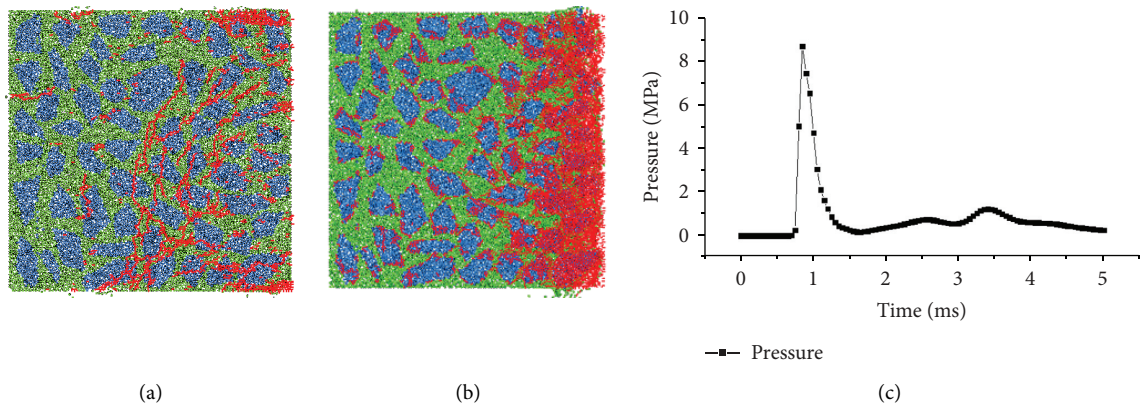

Figure 20: (a) The damage of point D4 at normal temperature, (b) the damage of point D4 at 600 K, and (c) the compressive wave.

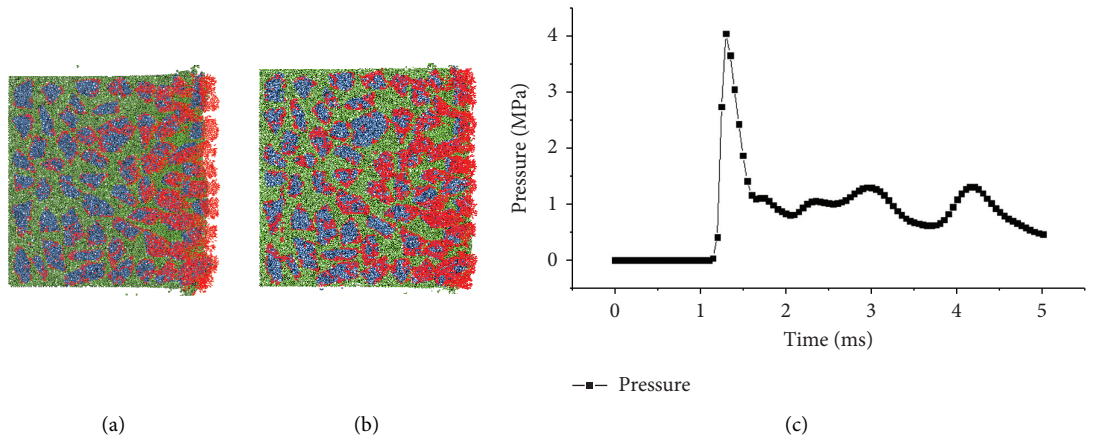

Figure 21: (a) The damage of point E0 at normal temperature, (b) the damage of point E0 at 400 K, and (c) the compressive wave.

By comparison, the damage of the concrete block was obviously enlarged due to the high temperature after being impacted by the same compressive wave.

From the two monitoring points, B0 and B4, which are slightly away from the origin of explosion shock, the shock wave showed a secondary peak, and this phenomenon is completely consistent with the propagation rule of air shock wave in the tunnel.

It can be seen from Figures 20–22 that the damage was mainly located at both sides of the surface and then developed into the depth. The damage in the central part was mainly due to the diagonal interface of the aggregates, which leads to the expansion of the cracks on both sides to the center. In the process of simulation, it can be clearly seen that the intensity of damage was obviously related to the peak value of the stress wave.

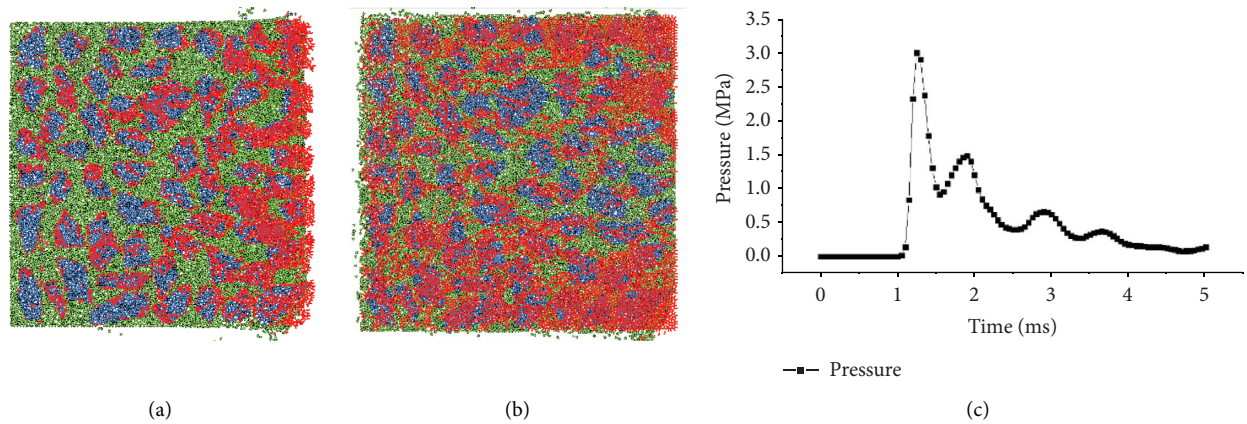

Figure 22: (a) The damage of point E4 at normal temperature, (b) the damage of point E4 at 700 K, and (c) the compressive wave.

The failure modes of experiments and PFC^{2D} simulation models can be divided into three types. First, the aggregate is broken, which has a low probability and generally occurs on the path of the main crack, indicating that the instantaneous pressure at this stage of stress density exceeds the strength of the aggregate itself. Second, the internal failure of cement mortar usually occurs when the mortar strength is low. Third, the breakup of binding connection on the interface between aggregate and cement mortar is very common. Moreover, the crack development direction will change when encountering aggregates in the cracking path. Therefore, the section strength of the micro cement mortar and aggregate ultimately determines the final strength of the macro concrete blocks.

According to our simulation results, the tunnel concrete lining can be divided into the area of explosion damage, the area of high temperature damage, and the area of mixed damages. The boundaries of the three zones are influenced by the internal structure of the tunnel, slope, ventilation speed, explosion equivalent, and the distance between vehicles and the lining structure.

5. Conclusions

(1) The damage process of the concrete material subjected to explosive impacts at different temperatures has been simulated by the discrete element method. The aggregate generated by the clump method can truly reflect the inherent characteristics of aggregates and mortars in concrete. The damage process of the concrete blocks is a dynamic process of energy accumulation and release. Our model can intuitively visualize the fracture originated at the weak interface layer. In the process of PFC^{2D} calibration, the parallel bond model of cement mortar directly affects the peak stress of the stress-strain curve of concrete, while the strength of aggregate itself has little effect, which is consistent with our experimental observations.

(2) The damage of tunnel lining structure after explosion and combustion is mainly caused by high temperature, overpressure impact, and gases such as carbon monoxide. The increase of the temperature has amplified the compress damage significantly.

(3) More attention should be paid to the improvement of vault and arch waist when repairing the middle and rear parts of the lining structure [18].

(4) The simulation results of the discrete element method combined with LS-DYNA and FLUENT can more accurately determine the damage degree of the concrete blocks. These methods will be helpful for providing valuable information needed in making repair decisions and predicting the residual lifetime of a damaged tunnel.

Data Availability

All the data, models, and code generated or used during the study are included in the submitted article.

Conflicts of Interest

The authors declare that they have no conflicts of interest.

Acknowledgments

The research presented in this paper was funded by the Open Fund Project of State Key Laboratory of Disaster Prevention in Civil Engineering, Tongji University, China.

References

[1] N. Hua, A. Tessari, and N. Elhami Khorasani, "Characterizing damage to a concrete liner during a tunnel fire," *Tunnelling and Underground Space Technology*, vol. 109, Article ID 103761, 2021.

[2] H. D. Wang, S. Y. Wang, and X. G. Ban, "Numerical simulation on accident ventilation modes in subway tunnel fire," in *Proceedings of the International Conference of Chinese Transportation Professionals*, 2011.

[3] S. Feng, Y. Li, Y. Hou, J. Li, and Y. Huang, "Study on the critical velocity for smoke control in a subway tunnel cross-passage," *Tunnelling and Underground Space Technology*, vol. 97, Article ID 103234, 2020.

[4] L. Yi, Q. Xu, Z. Xu, and D. Wu, "An experimental study on critical velocity in sloping tunnel with longitudinal ventilation under fire," *Tunnelling and Underground Space Technology*, vol. 43, no. 1, pp. 198–203, 2014.
[5] V. Verda, R. Borchiellini, S. Cosentino, E. Guelpa, and J. M. Tuni, "Expanding the fds simulation capabilities to fire tunnel scenarios through a novel multi-scale model," *Fire Technology*, vol. 57, pp. 1–24, 2021.
[6] X. Wu, X. Zhang, X. Huang, F. Xiao, and A. Usmani, "A real-time forecast of tunnel fire based on numerical database and artificial intelligence article history," *Building Simulation*, vol. 3, no. 3, 2021.
[7] Y. Lu, S. Liu, F. Tian, J. Chen, and S. Deng, "Studies and prospects of technologies for monitoring highway tunnel fire," *IOP Conference Series: Earth and Environmental Science*, vol. 634, no. 1, Article ID 012099, 2021.
[8] Q. Meng, C. Wu, J. Li, P. Wu, S. Xu, and Z. Wang, "A study of pressure characteristics of methane explosion in a 20 m buried tunnel and influence on structural behaviour of concrete elements," *Engineering Failure Analysis*, vol. 122, Article ID 105273, 2021.
[9] M. Zaid, R. Sadique, and M. Samanta, "Effect of unconfined compressive strength of rock on dynamic response of shallow unlined tunnel," *SN Applied Sciences*, vol. 2, 2020.
[10] F. Pan, P. F. Gao, L. Yang, Z. W. Zhu, L. Yang, and M. U. Chao-Min, "Numerical investigation on blast shock wave propagation of an explosion inside its entrance to a multilevel hallery tunnel," *Journal of Safety Science and Technology*, vol. 11, 2013.
[11] B. Beckmann, K. Schicktanz, D. Reischl, and M. Curbach, "Dem simulation of concrete fracture and crack evolution," *Structural Concrete*, vol. 13, no. 4, pp. 213–220, 2012.
[12] L. B. N. Le and P. Stroeven, "Strength and durability evaluation by dem approach of green concrete based on gap-graded cement blending," *Advanced Materials Research*, vol. 450-451, pp. 631–640, 2012.
[13] W.-l. Qiu, R.-x. Peng, and M. Jiang, "Meso equivalent calculation model for frost evaluation of concrete," *Construction and Building Materials*, vol. 272, no. 3–4, Article ID 121867, 2021.
[14] A. Ghazvinian, V. Sarfarazi, W. Schubert, and M. Blumel, "A study of the failure mechanism of planar non-persistent open joints using pfc2d," *Rock Mechanics and Rock Engineering*, vol. 45, no. 5, pp. 677–693, 2012.
[15] S. Zhou, H. Zhu, L. Zhang, J.-W. W. Ju, and Z. Yan, "A micromechanical study of the breakage mechanism of microcapsules in concrete using pfc2d," *Construction and Building Materials*, vol. 115, 2016.
[16] J. Su, L. Zhang, and Y. Zhao, "Numerical simulation of fracture process of concrete under uniaxial compression via pfc2d," *IOP Conference Series: Earth and Environmental Science*, vol. 61, no. 1, Article ID 012069, 2017.
[17] X. Liu, X. Chang, W. Zhou, and S. Li, *Pfc2d Simulation of Thermally Induced Cracks in concrete Specimens*, American Institute of Physics, College Park, MD, USA, 2013.
[18] T.-b. Zhao, M.-l. Xing, W.-y. Guo, C.-w. Wang, and B. Wang, "Anchoring effect and energy-absorbing support mechanism of large deformation bolt," *Journal of Central South University*, vol. 28, no. 2, pp. 572–581, 2021.

Hindawi
Advances in Civil Engineering
Volume 2021, Article ID 6446233, 12 pages
https://doi.org/10.1155/2021/6446233

Research Article

Estimation of Super High-Rise Pumping Pressure for High-Performance Concrete Based on Computational Fluid Dynamics Modeling and Situation Measurement

Weijiu Cui,[1,2] **Chuankai Zhao**,[1] **and Sheng Wang**[3]

[1]*School of Civil Engineering, Qingdao University of Technology, Qingdao 266033, China*
[2]*Innovation Institute for Sustainable Maritime Architecture Research and Technology, Qingdao University of Technology, Qingdao 266033, China*
[3]*Qingjian Group Co., Ltd., Qingdao 266011, China*

Correspondence should be addressed to Weijiu Cui; cuiweijiu@163.com

Received 9 August 2021; Accepted 8 October 2021; Published 30 October 2021

Academic Editor: Guoming Liu

Traditional methods fail to predict the pumping pressure loss of high-performance concrete properly in super high-rise pumping situations due to complex changes of concrete properties. Therefore, it is imperative to propose a relative accurate method for pumping pressure estimation in super high-rise buildings. This paper builds the simplified pressure calculation method "pressure induced by the gravity plus pressure along the pipe line." The later one is gained by establishing topology optimized model based on computational fluid dynamics and considering the lubrication layer formation. The effect of rheological properties and flow rate is analyzed based on this model in detail. Furthermore, the developed calculation method is verified by the measured pumping pressure during the super high-rise building construction of the Shanghai Tower (the tallest building in China recently). The relative differences between the calculation results and the measured data in situ are less than 6%, indicating the applicability of this method for predicting the pressure loss of the super high-rise pumping.

1. Introduction

Concrete pumping has been adopted in formwork casting for decades. It is widely used for concrete conveying during skyscraper construction because it is time-saving and environment-protecting. However, how to avoid pipeline leakage is still a bottleneck in the long-distance pumping process, such as super high-rise buildings, super long bridges, and long-distance tunnels, in which the pumping pressure plays a crucial role. This is mainly because both mixture design of fresh concrete and equipment selection depend on the prediction of pumping pressure, especially for super high-rise pumping.

Therefore, it is very important to predict the pumping pressure of concrete accurately and simply. ACI 304.2R-96 gives a chart used for calculation of the pressure loss [1]. In addition, technical specification for construction of concrete pumping provides an empirical formula for pressure per meter [2]. These specifications play a crucial guiding role in the traditional concrete pumping construction, but they are not suitable for the pressure prediction of high-performance concrete [3]. This is mainly due to the reason that the workability of high-performance concrete may be significantly affected by the addition of various superplasticizers or supplementary cementitious materials [4]. Therefore, as the rheological mechanism of concrete can not be fully considered, it is necessary to carry out research from the rheological point of view to modify the concrete pumping pressure calculated by the traditional estimation method. Fresh concrete is a viscoelastic-plastic body, and its flow is induced by shear actions [5]. The rheological parameters, especially the plastic viscosity and yield stress, are the key factors during the flow process [6–9]. Different rheological models, including Bingham model, Herschel and Bulkley

model, and Casson model, have been proposed to describe the flow regime of fresh concrete [10]. Among them, Bingham model is one of the most commonly used models for high-performance concrete [11]. Besides, the lubrication layer is of vital importance in concrete pumping process, which relates to the shear-induced migration of particle inside the pumping pipe [12].

Based on the theory of tribology, the rheological properties of the lubricating layer can be obtained, and the friction on the boundary can be calculated accurately [13]. In addition, the pressure loss has a strong relationship with its discharge rate. The relation curve between linear pressure loss and discharge rate has been obtained by in situ tests [14–18] or the sliding pipe rheometer [19]. The pressure loss can also be obtained by the reverse calculation of the discharge rate, where the discharge rate is integrated by the velocity distribution in the pipe section [20, 21]. However, the theoretical models cannot be used to predict the actual pressure loss directly because of their implicit expression. Therefore, researches are carried to capture the relationship between the pressure and its governing factors. Due to the yield stress and the plastic viscosity kept relatively constant, the pressure drop shows a linear change with the pipe length increasing [22]. There is a first-order physical correlation between the pressure drop and the flow rate [23]; what is more, a suitable method is given to assess the pressure based on full-size pumping test [24]. This provides a new way to get the pressure, but the full-scale pumping test is time-consuming and labor-costing. Attention is paid on actual concrete pumping project recently. Based on X-ray CT and 3D mesoscopic numerical simulation, the multiscale mechanic properties change after actual pumping and suggestions for real pumping project are given [25]. A workability box of self-compacting concrete (SCC) suitable for direct pumping up to super tall building is given, among which the yield stress and the plastic viscosity are discussed [26]. Therefore, it is still imperative to develop a simplified pumping pressure loss calculation method of fresh concrete in super high-rise buildings.

To solve the above-mentioned problems, this study aims to establish a simplified pumping pressure estimated method based on mechanical analysis and measurement on spot. The pumping force per meter is attained by computational fluid dynamics. The effects of various factors such as flow rate, lubrication layer thickness, yield stress, and viscosity on the lubricating effect are studied. Afterwards, the calculation results are compared with the high-rise pumping pressure recorded during the Shanghai Tower construction process.

2. Calculation Method Introduction

2.1. Force Condition of Pumped Concrete. The actual concrete pumping process is shown in Figure 1. Concrete flows through the pipe line under pressure action supplied by the pump. According to the fluid mechanism, the inlet is taken as velocity type where the value is determined by the actual flow rate. Meanwhile, the outlet is set as pressure type where the velocity is zero. When the concrete flow develops into the stable mode, a representative part of the whole pumping line is separated to undergo a mechanical analysis as shown Figure 1. The fresh concrete is subjected to pressure (P), gravity (G), and friction (F) in the meantime, as expressed in equation (1). The analyzed fresh concrete owns a cylinder shape. Its radius in the ground section and height is expressed by r and h, respectively. The friction is equal to the shear stress multiplied by its area as in equation (2), while gravity can be easily obtained by equation (3).where P represents the pumping force (kg·m/s^2), G denotes the gravity-induced force (kg·m/s^2), and f reflects the force caused by friction (kg·m/s^2). $\tau$and p are the inherent performance of the material, representing the yield stress (Pa) and the density (kg/m^3), respectively. r is the radius (m) of the pipe cross section and h is the vertical height of the pumping pipe (m); g is the gravitational acceleration (m/s^2).

$$P = G + F, \tag{1}$$

$$F = \tau A = \tau(2\pi r h), \tag{2}$$

$$G = \rho\left(\pi r^2 h\right)g, \tag{3}$$

The pumping pressure can be obtained, as shown in the following equation:

$$P = \Delta P A = \Delta P \pi r^2. \tag{4}$$

Based on above equations, the pressure loss is calculated as shown in the following equation:

$$\Delta P \pi r^2 = \tau(2\pi r h) + \rho\left(\pi r^2 h\right)g. \tag{5}$$

A simplified form is shown in equation (5) dividing the same parameter at the both sides of equation (5).

$$\Delta P = \frac{2\tau}{r}h + \rho g h, \tag{6}$$

where ΔP represents the pumping pressure (Pa). According to equation (6), the pumping pressure relates to two factors: the gravity-induced pressure and the frictional-induced one. For the same material, the former one only depends on the pumping height. As for the later one, there are more complicated influential factors. Under the pressure action, the fresh concrete bears a linear shear stress action where it changes zero at the center to peak value at the pipe inner surface. The shear-induced deformation cannot happen unless the shear stress overpasses the yield stress. Therefore, the shear rate shows a linear trend at the deformation area. There is no deformation among the center areas. Consequently, a plug flow is formed (see Figure 2). The discharge rate is obtained by integration on the pipe section.

The fresh concrete takes on Bingham flow in the pipe; its constitutive relationship can be described by equation (7). A correlation can be easily found between the shear rate and the pumping discharge rate. That is to say, the pressure loss along the pipeline can be determined by plastic viscosity, pipe radius, and discharge rate.

$$\tau = \tau_0 + \mu\dot{\gamma}. \tag{7}$$

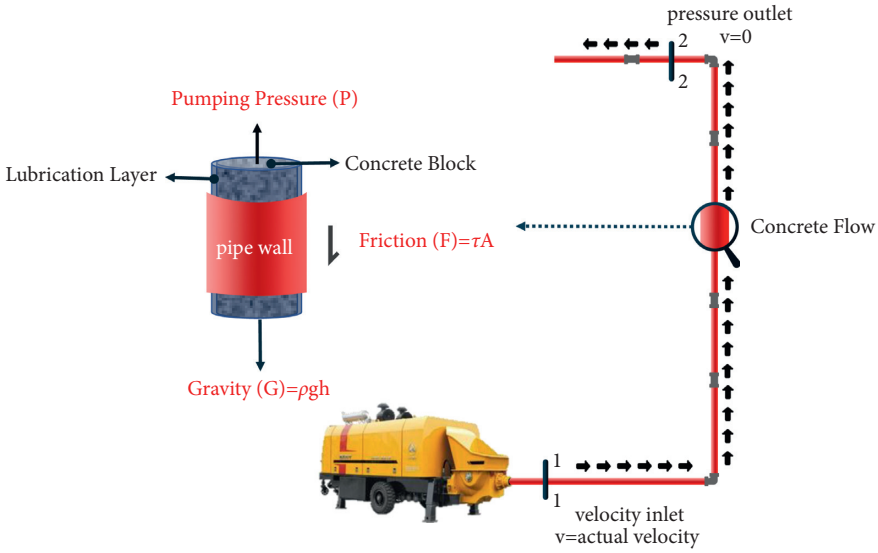

Figure 1: The diagrammatic sketch of concrete pumping and its mechanical analysis.

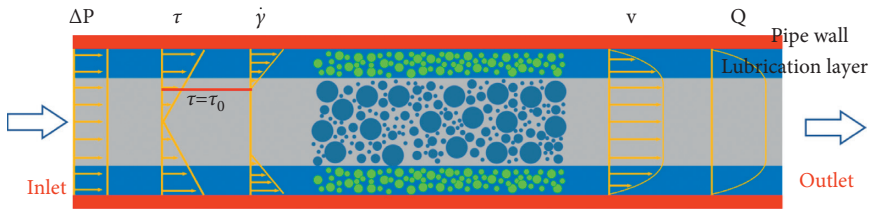

Figure 2: Pressure, shear stress, shear rate, velocity, and discharge rate profiles inside a pumping pipeline.

A simplified equation is given when taking equations (1) and (6) into consideration, as shown in

$$\Delta P = \delta l + \rho g h, \tag{8}$$

where δ denotes the coefficient of pressure loss along the pipeline (Pa/m), l is the total length of the pumping pipe (m), and h represents the height of the pumping pipe (m).

The coefficient δ in (8) represents the pressure loss per meter, which is determined by rheological parameters, pipe radius, and discharge rate. In this paper, the numerical simulation model is established to determine the coefficient of pressure loss along the pumping pipe.

2.2. Pressure Loss per Meter by Computational Fluid Dynamics. A suitable model is the premise of successful simulation. A 2D symmetrical meshing method is used to simplify the 3D simulation [15]. This method brought a high coincidence degree compared with the in situ test results. In the case that the calculation process is asymmetrical, the 2D symmetrical method is no longer applicable. Therefore, a 3D simulation model is adopted in this paper. The flow rate is assumed to be constant during the whole pumping process and the length of the calculation unit is set as 10 m. The whole grid establishing process is displayed in Figure 3. As discussed above, a plug flow forms in the 150 mm pipe. The geometric body is firstly established. For the thickness of the lubrication layer is known as 2 mm [6], two concentric circles are sketched with a 150 mm outer diameter and a 146 mm inner one. Those two circles just empress the concrete block and the lubrication layer. Then, a cylindrical body is formed by image stretching. The 3D model is set up.

The model gird establishment has a remarkable effect on the efficiency and accuracy of simulation analysis. The concrete flow bears friction near the pipe wall where the lubrication layer exists. Thus, the quality of the girds in lubrication layer determines the accuracy of the pressure loss simulation value. Therefore, the whole section is divided into two parts shown in Figure 3. The gird is encrypted to 5 layers in the lubrication layer (blue part shown in Figure 3), with 0.4 mm thickness of each layer. Meanwhile, the thickness of the mesh in the block area (purple part shown in Figure 3) is 5 times that of the lubrication layer. The length of gird is the same on both areas. The mesh size is set as 50 mm along the pipe direction. It is a consensus that the angel of each two sides should be close to 90° for the fluid gird. A topological operation called O-grid is imposed on the original gird. The whole section is divided into five parts; the red line empresses its edge. From Figure 3, we can see that the angel of all two sides should be close to 90° for any gird in any part.

The boundary conditions were defined according to actual pumping. From the mechanical analysis in Figure 1, the inlet is defined as velocity type inlet and the velocity value is determined by the flow rate. The outlet is defined as

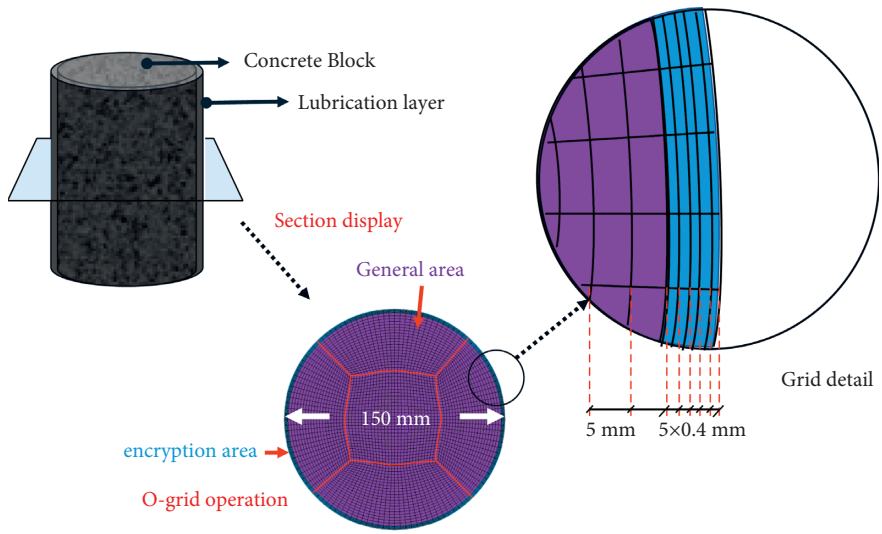

Figure 3: The topological mesh considering the lubrication layer.

pressure type outlet where its velocity is zero. There are two velocity inlets and two pressure outlets because of section division. The inner surface of the pumping pipe was set as no-slip wall boundary condition in order to reflect the friction. To ensure that the particles exchange freely on the interface between the lubrication and the block area, an internal contact is set on the contact plane. At last, the calculation step is preset as 1500 with a consideration of both the calculation efficiency and the precision.

2.3. Pumping Conditions. In order to increase the accuracy of simulation analysis, the working conditions design depends on the actual pumping conditions. According to the discussion above, the pressure loss is mainly caused by the gravity and the friction-induced pressure. For the former one, vertical pipe direction with considering gravity action is shown in Table 1, while horizontal one is set as no gravity. For the latter one, it is mainly affected by the concrete velocity, the performances of lubrication layer, which includes the thickness, the plastic viscosity, and the yield stress. The pipe line for actual concrete pumping is composed of the straight pipe and the bend pipe. Thus, there are 6 kinds of influential factors shown as the first row in Table 1. The values are determined by the actual concrete pumping. For example, the bend angles of the bend pipe are 30°, 45°, and 90° in China. Based on the actual concrete pumping discharge, the working conditions for the discharge rate range from 10 to 100 m^3/h. The rest of factors are also designed following the same principle; the whole working conditions are shown in Table 1.

3. Results and Discussions

3.1. Numerical Simulation Results

3.1.1. The Influence of Lubrication Layer Thickness. Although the thickness of the lubrication layer has obvious influence on the pressure loss of concrete pumping, its exact value is difficult to determine because of the lack of appropriate monitoring measurement. At present, it is a consensus that the thickness of the lubrication is 2 mm. In order to get a generic numerical result, the thickness variable ranges from 1 mm to 5 mm during the numerical simulation. The results are shown in Figure 4. The pressure loss decreases obviously when the thickness of the lubrication increases. Its attenuation is larger when the thickness changes from 1 mm to 2 mm or from 2 mm to 3 mm. When the thickness exceeds 3 mm, the same increment of 1 mm will lead to smaller pressure loss attenuation. Furthermore, the influence of lubrication layer on pumping performance of concrete is proposed. Its thickness determines the value of pressure loss. In other words, the thickness of the lubrication layer is not enough to provide enough mortar for lubrication, resulting in increased friction in the process of pumping concrete. This trend will be aggravated under high velocity. Therefore, the thickness of the lubrication layer should be chosen accurately according to the actual situation.

3.1.2. The Influence of Gravity. As discussed above, the gravity action plays a significant role in the pressure loss, while it can be calculated by a simple form. To further check its rationality, the pressure loss simulation is carried for different pipe types (horizontal pipe and vertical one) which are commonly used in the super high-rise pumping situations. As for the vertical pipe, the gravity is imposed on the model. According to the rheology test taken before, the yield stress is distributed around 100 Pa which is also set as input value for simulation, while the plastic viscosity is 60 Pa · s. Figure 5 presents the pressure loss comparison between the vertical and horizontal pipes under different discharges. It is shown that the pressure difference caused by concrete is close to 0.024 MPa, which is almost equal to the hydrostatic pressure value per meter (0.0245 MPa). Therefore, the vertical mode will not be analyzed in the following sections.

Table 1: Working conditions design.

Lubrication layer thickness (mm)	Discharge rate (m^3/h)	Plastic viscosity (Pa · s)	Yield stress (Pa)	Pipe direction	Bend pipe angel °
1	10	10	100	Horizontal	30
2	20	20	300	Vertical	45
3	30	30	500		90
4	40	40	700		
5	50	50	900		
	60	60			
	70	70			
	80	80			
	90	90			
	100	100			

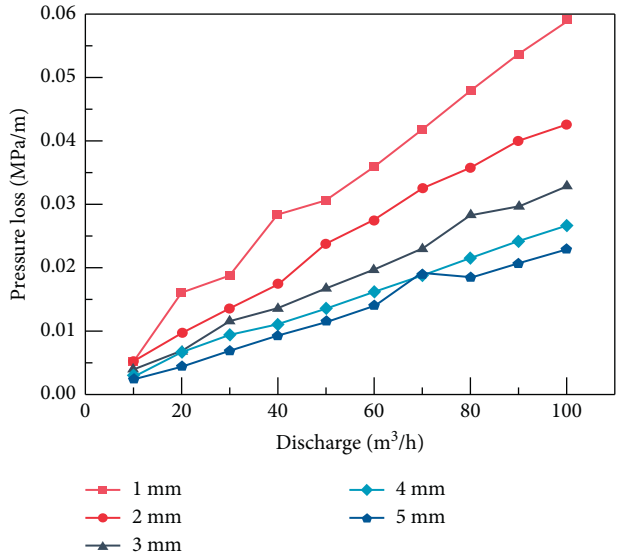

Figure 4: The pressure loss-discharge rate curve under different thickness of lubrication layer.

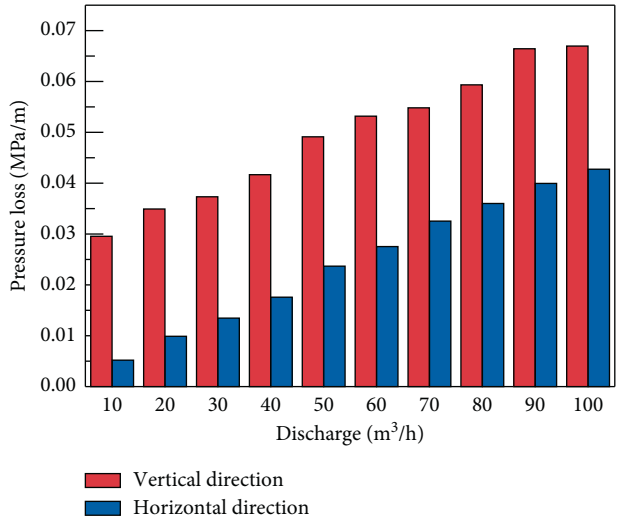

Figure 5: The pressure loss comparison between the vertical and horizontal pipes under different discharges.

3.1.3. Sensitivity Analysis. Theoretically, the yield stress is the key factor to determine whether the flow of fresh concrete starts or not, and the plastic viscosity will decrease the flow. However, it is difficult to determine which parameter has more significant effect on the concrete flow in the pipe. Therefore, sensitivity analysis is needed to determine the effect of each parameter. The plastic viscosity values were derived from the experimental flow curve, which were set from 10 to 100 Pa·s. In addition, the yield stress values are selected from 100 to 900 Pa. The thickness of the lubrication is set as 2 mm, while the discharge is fixed at 30 m^3/h which is commonly used in actual concrete pumping. All this detailed information is shown in Table 1. The relationships between the pressure loss and the rheological parameters (the plastic viscosity and the yield stress) is shown in Figure 6(a). It was shown that the pressure loss increases with the increase of plastic viscosity and yield stress. The slope of the plastic viscosity axis is more abrupt than that of the yield stress axis which can be seen in Figure 6(a). It proves that the plastic viscosity has a more remarkable effect on the pressure loss than the yield stress. Those results for the 125 mm pipe are shown in Figure 6(b); the tendency is just the same with that of the 150 mm pipe. It is shown that the pressure loss increases with plastic viscosity and yield stress. The slope of the plastic viscosity axis is steeper than that of the yield stress axis. The results show that the effect of plastic viscosity on pressure loss is more significant than yield stress. According to the flow mechanism of concrete, the yield stress is the flow threshold to determine the flow mode. During the process of flow, viscous hindrance caused by the plastic viscosity should be considered. At present, there are still some obstacles in using rheological parameters to characterize the pumping ability of concrete in practical engineering.

According to fluid mechanics, the velocity (transferred by the discharge rate which is commonly used in actual concrete pumping) is the most remarkable factor affecting the concrete flow. Combined with previous sensitivity analysis, the discharge rate and the plastic viscosity are discussed in this part. There are three kinds of bend pipes for concrete pumping. They are 30°, 45°, and 90°. The pressure loss of the 90° bend pipe (see Figure 7) is discussed with the plastic viscosity and the discharge changing, because it is the type most used in practical engineering. The three axes represent the pressure loss, the plastic viscosity, and the discharge rate, respectively. It can be seen that the pressure loss increases with an increase in either the plastic viscosity or the discharge rate. The slope of the discharge rate axis is more abrupt than that of the plastic viscosity axis. That is to

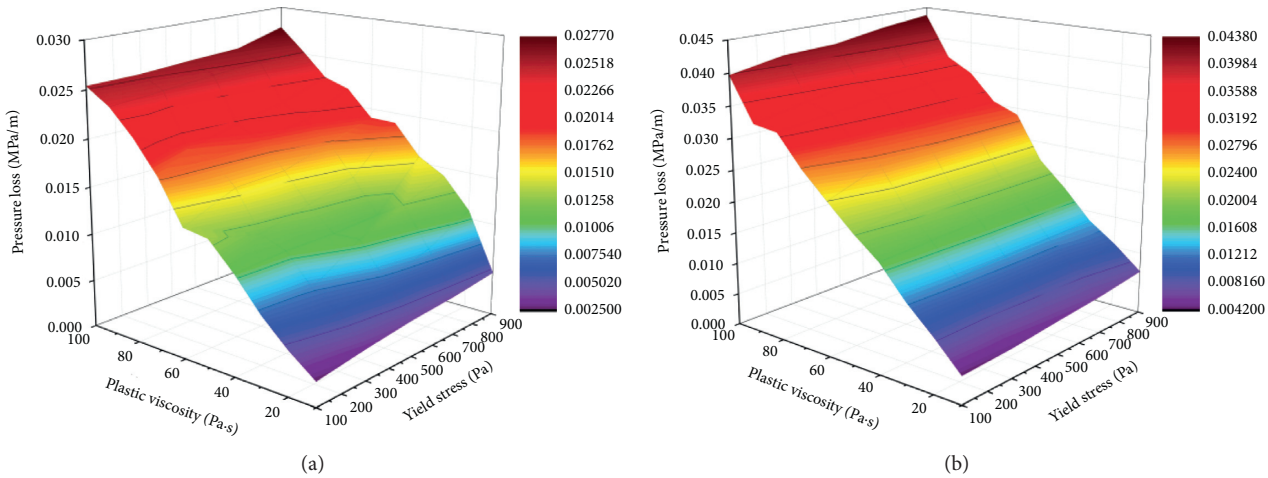

Figure 6: The change of pressure loss under different rheological parameters: (a)ϕ150 mm and (b)ϕ125 mm.

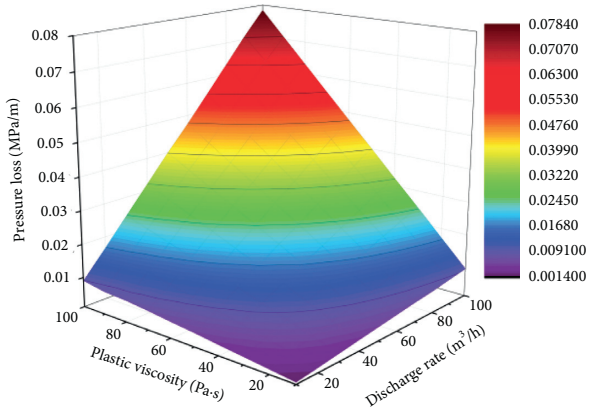

Figure 7: The pressure loss change under different discharge and plastic viscosity.

say, the effect of discharge on the pressure loss is more remarkable than that of the plastic viscosity only from a mathematical perspective of view. However, they are different if the physical significance is also taken into consideration. Namely, both the discharge and the plastic viscosity should be taken into account at the same time while the pressure loss is calculated. Besides, the pressure loss of the 90-degree bend pipe is close to that of the straight pipe under the condition that the influential parameters are set equally. It claims that there is no sudden change for bend pipe which is different from the ordinary code.

3.2. Method Validation

3.2.1. Project Overview. The Shanghai Tower, 632 m high, is the tallest building in China at present. It also brings great challenges to the concrete pumping. For one side, the concrete flow ability should be high enough to make sure that the concrete can reach its final height; for another side, the cohesiveness should be enough to avoid segregation during concrete pumping.

According to the concrete performance and structure characteristics, the concrete stress grade changes along the vertical direction. Self-compacting concrete (SCC) is the best choice if the economic factor can be omitted. High workability concrete (HWC) is also used reasonably for economic consideration. The actual construction sense for different heights is shown in Figure 8. The pressure and the discharge are recorded at the same time in order to carry a comparative analysis.

3.2.2. In Situ Pressure Measurements. During the concrete construction in Shanghai Tower, the highest pressure pump (shown in Figure 9) is used in China. The pressure is measured by the record of the dashboard of the fixed pump; then the concrete pumping pressure is obtained according to a specific conversion rule. There are three dashboards on one pump. They are agitating pressure, change-over pressure, and the pressure of the main system, respectively. The main system pressure represents the pressure which conveys the material to the target location, while the rest of pressures mainly reflect the dynamic performances of the pump. The pressure for concrete pumping is a relative pressure value, which is the pressure difference between the inlet and the outlet of the pumping system. The pressure of the outlet is assumed as zero. The actual concrete pumping pressure can be acquired by multiplying the main system pressure with an efficacy coefficient. The concrete pumping discharge and its pumping time are also recorded on the spot. Another key factor, discharge rate, is obtained by a mathematical division operation, for the concrete appears as constant flow in this study. By this method, the original information is obtained during the pumping process.

As this study mainly focuses on the super high-rise concrete pumping, the pumping information is collected for the pumping height over 94 m. The main concrete grades are C70 and C60. The pressure which includes the concrete pressure and the main system pressure is recorded for three different height intervals, while the pumping discharge is also collected at the same time.

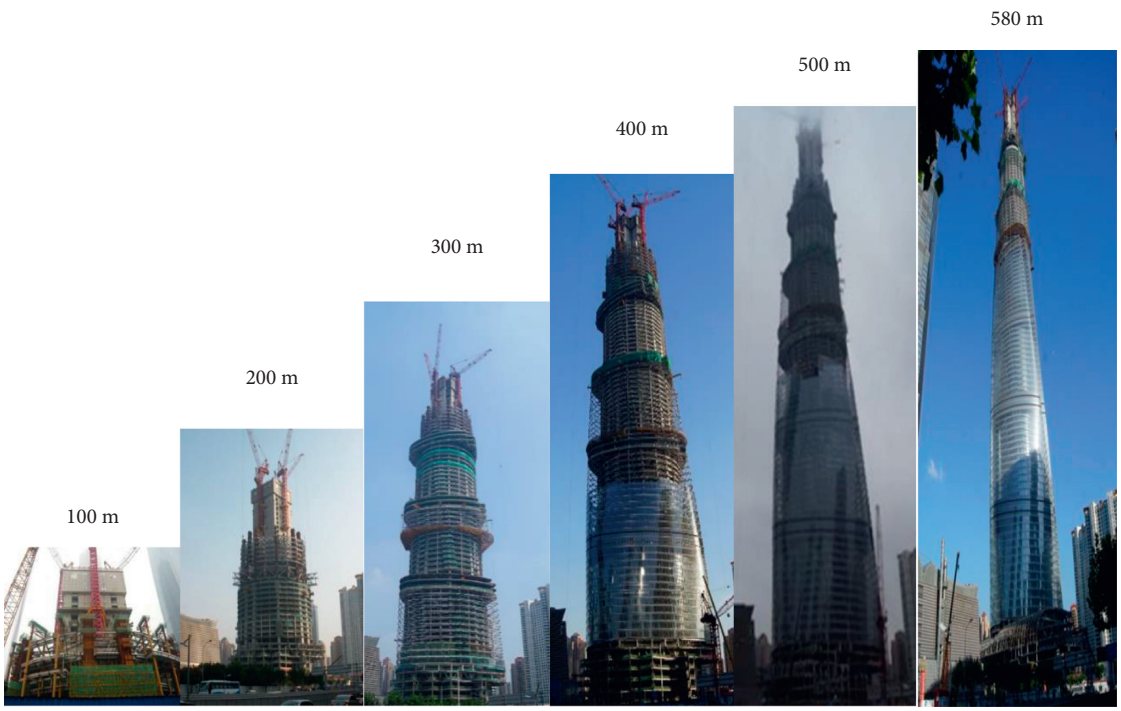

Figure 8: The different concrete pumping heights for the Shanghai Tower.

Figure 9: Pressure record via huge pump on the spot.

Pumping height grabs much attention in super high-rise concrete pumping. Thus, the pressure change law along with the pumping height is discussed in this project. Both the main system pressure and the concrete pressure are shown in Figure 10. The whole figure can be divided into three parts according to pumping height and the concrete strength grade. It can be noticed that there is a high positive correlation between the main system pressure and the concrete pressure. When the pumping high interval changes from 94~164 m to 240~310 m, the pressure increases substantially. Curiously, the pressures do not increase obviously with the height growing from the 240~310 m interval to 540~590 m one. This is mainly because that the discharge decreases below 45 m^3/h (see Figure 11). On the contrary, they decrease with the height growing such as the 243 m height and the 250 m height. A reasonable explanation is that the pressure is affected by multiply factors except for the height. The pressure can also keep decreasing only by slowing down the discharge or reducing the plastic viscosity with the increase of height. In other words, it is necessary to consider all the factors when the pressure law is concluded.

3.2.3. Comparative Analysis. Based on the previous analysis in Section 2, the pressure loss for concrete pumping mainly contains two parts, the pressure caused by the gravity action and the pressure along the pumping pipeline. According to the conveying pipe type, the latter one is further divided into pressure loss for the straight pipe and that caused by the bend pipe. The calculation formula is shown in (9). The key factor for the pressure calculation is δ (pressure loss). The pressure loss is calculated by its length for the straight pipe, while the pressure loss of the bend pipe is obtained by its number. The pressure loss coefficient is affected by rheological parameters, discharge, pipe diameter, and pipe type. The specific relation between the coefficient and its affected

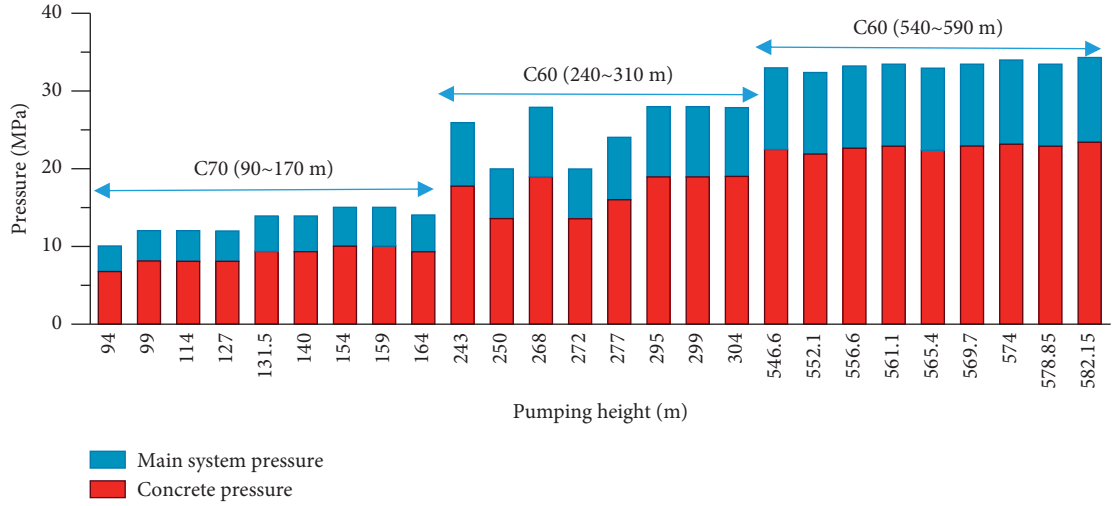

Figure 10: The change law between the pressure and the height.

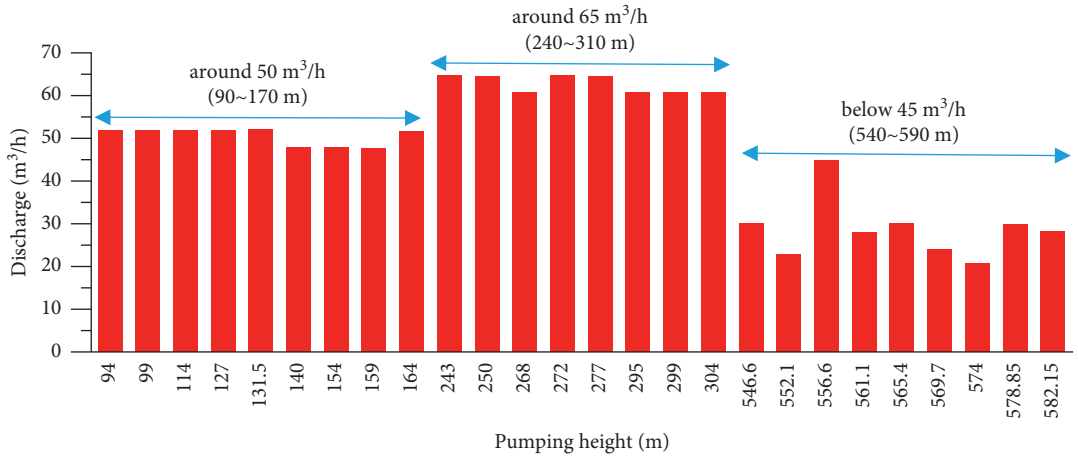

Figure 11: The pumping discharge for different pumping height interval.

factors is determined by simulation in Section 3.1. Then, the pressure values can be calculated according to the original information in Shanghai Tower pumping construction. To check the rationality of this method, a compared analysis with the measured data is made in the following part:

$$\Delta P = \rho g_h + \delta_h l + \delta_i n_i, \tag{9}$$

where ΔP represents the pressure value (MPa), h denotes the pumping height (m), p is the inherent performance of the material representing the density (kg/m^3), and l reflects the total length of pipe line (m). δ_h is the pressure loss coefficient of the straight pipe (MPa/m), while δ_i represents the pressure loss coefficient of the straight pipe of the bend pipe; =1, 2, and 3, represented 90°, 45°, and 30°, respectively(MPa). At last, n_i reflects the bend numbers.

The coefficient is only related to rheological parameters and discharge rate under the condition that the pipe diameter is fixed. According to the sensitivity analysis of rheological parameters, plastic viscosity plays a dominant role in the pressure loss. A rheological performance test by the rheometer named ICAR is carried with the same concrete mixing proportion of that in this project. The plastic viscosity increases while the slump decreases. It changes from 40 Pa·s to 70 Pa·s, when the initial slump is around 600 mm. It begins at 35 Pa·s and ends at 55 Pa·s, while the initial slump is around 700 mm. Unfortunately, it failed to find a qualitative relationship. Thus, a plastic viscosity average value is adopted for the pressure loss calculation. Appropriate adjustment for the slump is carried based on the actual pumping. At the height interval (243~304 m), the slump decreased to 600 mm, while it enlarges to 700 mm at the height interval (546~582 m). Finally, the plastic viscosity calculation value is taken as 55 Pa·s for the height interval (243~304 m), and that is 45 Pa·s for the height interval (546~582 m). The other parameters are shown in Table 2 according to the project information. Besides, there are four bend pipes with 90° and two bend pipes with 45°.

To simplify the pressure loss calculation, its controlling chart is drawn by the simulation results. The coefficient can be easily obtained if the plastic viscosity and the discharge are all foreknown. As both the plastic viscosity and the

Table 2: The comparison for the calculated pressure value and measured one.

Pumping height (m)	Plastic viscosity (Pa · s)	Discharge (m^3/h)	Calculated value (MPa)	Measured value (MPa)	Relative error (%)
243	55	65	16.33	17.7	−7.71
250	55	65	16.69	13.6	22.69
268	55	61	16.86	19	−11.28
272	55	65	17.79	13.6	30.80
277	55	65	18.0	16	−12.75
299	55	61	18.36	19	−3.39
295	55	61	18.16	19	−4.41
299	55	65	19.27	16	20.48
304	55	61	17.98	19	−5.39
546.6	45	30	21.10	22.5	−6.21
552.1	45	23	19.74	22	−10.27
556.6	45	45	24.22	22.6	7.18
561.1	45	28	21.62	22.9	−5.61
565.4	45	30	21.77	22.5	−3.26
569.7	45	24	20.32	22.9	−11.25
574	45	21	18.86	23.1	−18.35
578.85	45	30	22.24	22.9	−2.87
582.15	45	28	22.36	23.4	−4.45

discharge are designed as per ten counts, a linear interpolation is taken to deal with the nondecimal values in the actual concrete pumping. Take the concrete pumping at the 243 m height level as an example, its plastic viscosity and discharge are 55 Pa·s and 65 m^3/h, respectively; then the coefficient can be the average value of those under the condition of (50 Pa·s, 60 m^3/h), (50 Pa·s, 70 m^3/h), (60 Pa·s, 60 m^3/h), and (60 Pa·s, 70 m^3/h), respectively. It is 0.026625 MPa/m, while the coefficients of 90° bend and 45° angles are 0.028975 MPa and 0.01995 MPa, respectively. Then, the pressure loss can be acquired by (9) as follows:

$$P = 2400 \times 9.8 \times 243 + 0.026625 \times 393 + 0.028975 \times 4 + 0.01995 \times 2 = 16.33479\,(\text{MPa}). \tag{10}$$

By this way, all the pressures are calculated at different heights. The results are recorded in Table 2. The relative error which reflects the accuracy of the calculated value is obtained by

$$\text{relative error} = \frac{\text{calculated value} - \text{measured value}}{\text{measured value}} \times 100\%. \tag{11}$$

It can be seen from Table 2 that the relative differences errors between the calculated values and the measured ones can be distributed among 13%; most of them are within 6%. But there are still exceptions for pressures at such heights including 250 m, 272 m, 299 m, and 574 m. It can be concluded that this method is reasonable for pumping pressure calculation of the concrete super high-rise pumping. The calculated values of the pressure are generally less than the measured ones because of the plastic viscosity difference between the calculated value and the measured one. The plastic viscosity is supposed to be a constant value for pressure calculation, while it will increase because of the cement hydration and pressure compaction during the actual concrete pumping. Thus, calculation without considering the nonlinear change of the plastic viscosity leads to this negative difference. It still keeps an acceptable scale for the concrete pumping construction under the condition that the concrete can be pumped timely, which means that the fresh concrete is pumping without too long delay after its arrival. Further research is still indeed to consider the effect of the concrete plastic viscosity nonlinear change. Unfortunately, it is impossible to measure the plastic viscosity directly. Its actual change is hard to judge during the pumping process. In a word, it still needs much effort to form a calculated method with high accuracy.

The relative differences between the measured pressure and the calculated value show a huge gap for the pumping heights at 250 m, 272 m, 299 m, and 574 m with the biggest one being 30.80%. Either the inaccurate plastic viscosity value or discharge rate value leads to this problem. As we all know, the discharge rate can be recorded directly, while the plastic viscosity is set up by the slump test. Thus, it is definite that the unreasonable plastic viscosity value leads to pressure calculation distortion, which can also be confirmed by the engineer's record on the spot. It is difficult to keep the plastic viscosity uniform for different batches of the concrete with the same mixing proportion. The slump test of the concrete fluctuates with different batches. Therefore, the plastic viscosity can be adjusted according to the actual situation. After consulting the concrete pumping records, it is found that the slumps are close to 700 mm for those batches of the concrete which are used for pumping heights at 250 m, 272 m, and 299 m. The original plastic value is overestimated; then it is adjusted to 40 Pa·s. New calculated pressure is obtained; all

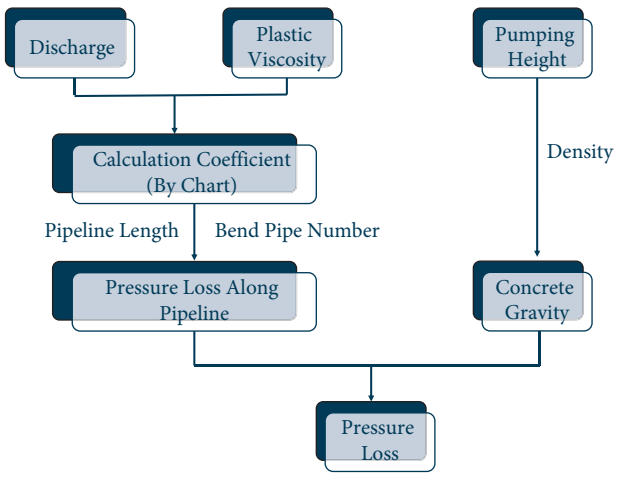

Figure 12: The simplified pressure loss calculation method for the concrete pumping.

the relative differences can be controlled within 6%. As for the pressure relative difference at 574 m height, it is mainly caused by underestimating the plastic viscosity. It is a consensus that a low discharge is adopted for high plastic viscosity concrete. The actual discharge rate is only 21 m^3/h. Thus, the plastic viscosity is enlarged to 55 Pa·s according to its slump. The relative difference between the newly calculated value and the measured one is 7.3%, which can suit the construction requirements. In a word, the simplified pressure method, determining the pressure loss coefficient by the pumping discharge and the plastic viscosity, is reasonable, which can estimate the pumping pressure loss for the concrete super high-rise pumping within an acceptable error scale.

3.2.4. Suggestion for Calculation. To further deepen engineers' impression, the simplified pressure calculation method is shown in Figure 12. Considering the deficiencies of the original method, the new method is refunded by the basic mechanic analysis. It can be seen from the figure that the pressure loss caused by gravity can be determined by the concrete density and the pumping height. The pressure loss along the whole pipe can be obtained by the coefficient and the pipe parameters. The coefficient is determined by the plastic viscosity and the pumping discharge together. That is to say, the pressure loss for the concrete super high-rise pumping is easy to estimate by this method if those parameters (see Figure 11) are determined.

Some suggestions are given to enhance its construction application because this method should be combined with the project experience closely. The discharge of fresh concrete has a strong relationship with the project schedule. It is usually a constant value determined by the planned schedule. Compared with the concrete slump, the plastic viscosity is more complicated. For the concrete with the same mixing proportion, the measured plastic viscosity appears as an internal around one fixed value. Before the concrete pumping begins, the concrete preparation work is carried in the laboratory. The plastic viscosity can be obtained at the same time. During the actual concrete pumping, the plastic viscosity will fluctuate because of the uncontrolled factors. Thus, it will lead to the difference between the estimated pressure and the actual value. Therefore, a plastic viscosity interval is given for pressure estimation. Its upper limit is determined by a 10 percent increment for the measured plastic viscosity, while its lower limit is 10 percentage decrements on the measured one. By this means, a reasonably estimated pressure is determined to guide the concrete super high-rise pumping construction.

4. Conclusions

As the pressure calculation method is no longer suitable for concrete pumping in present codes, a simplified calculation method which combines the concrete pumping pressure measurement in situ and computational fluid dynamics (CFD) simulation is established in this paper. The following conclusions could be drawn:

(1) The simplified method developed in this paper can be applied to predict the pumping pressure in the super high-rise pumping cases. The relative difference between the calculated pressure loss and the recorded pressure loss in situ can be controlled within 13%. The key factor of this method is pressure loss coefficient, which is determined by interpolation according to the discharge rate and the plastic viscosity.

(2) The pressure loss coefficient is obtained by computational fluid dynamics (CFD) simulation. During the simulation process, the gird in lubrication layer area is encrypted 5 times than that in the block area, and the block part is optimized by the topology method. The results show that this kind of simulation method can be further used in concrete pumping pressure calculation.

(3) A convenient concrete pumping guidance is claimed for engineers in actual projects. Engineers can estimate the concrete pumping pressure according to the plastic viscosity tested in advance and the scheduled pumping discharge before the concrete pumping. If unexpected event happens during the actual concrete pumping, engineers also can adjust the plastic viscosity or the pumping discharge according to this guidance. There still some brief issues needed for further study. Testing technology on spot for concrete pumping should be paid more attention to grab the real thickness of the lubrication. It is urgent to gather more data from other projects like the Shanghai Tower to optimize this simplified method.

Data Availability

The datasets used and analyzed during the study are included within the manuscript.

Additional Points

Highlights. (1) A simplified calculated method is proposed to predict the the pumping pressure. (2) The pressure loss along the pipe is mainly determined by the plastic viscosity and discharge rate of the concrete for a super high-rise pumping. (3) The simulation considering the lubrication layer gains a high accuracy with a topological meshed cross section. (4) The calculated pumping pressure is in good agreement with the test value in super high-rise building situ.

Conflicts of Interest

The authors declare that they have no conflicts of interest.

Acknowledgments

The authors would like to thank the engineers from Shanghai Construction Group for their valuable pressure data, in particular Delong Wu and Jianda Chen. This work was supported by the Open Fund of Innovation Institute for Sustainable Maritime Architecture Research and Technology (iSMART), Qingdao University of Technology (no. 2020-031).

References

[1] ACI, "Placing concrete by pumping methods," ACI 304.2R-96 Report, ACI Committee, Detroit, MI, USA, 2008.

[2] JCJ, *Technical Specification for Construction of concrete Pumping*, Architecture & Building Press, Ministry of Housing and Urban-Rural Construction of the People's Republic of China, Beijing, China, 2011, in Chinese.

[3] L. H. Li, X. W. Chen, M. L. Li, and P. Y. Yan, "Analysis on the changes of pumping pressure of self-compacting concrete in pipes," *Construction Technology*, vol. 45, no. 12, pp. 52–56, 2016, in Chinese.

[4] P. Y. Yan, M. Y. Li, J. G. Han, and X. Zhao, "Recent development on pumpability of fresh concrete," *Journal of the Chinese Ceramic Society*, vol. 46, no. 2, pp. 239–246, 2018, in Chinese.

[5] R. J. Phillips, R. C. Armstrong, R. A. Brown, A. L. Graham, and J. R. Abbott, "A constitutive equation for concentrated suspensions that accounts for shear-induced particle migrationv," *Physics of Fluids A Fluid Dynamics*, vol. 4, no. 1, pp. 30–40, 1998.

[6] J. S. Kim, S. H. Kwon, K. P. Jang, and M. S. Choi, "Concrete pumping prediction considering different measurement of the rheological properties," *Construction and Building Materials*, vol. 171, pp. 493–503, 2018.

[7] H. Xie, F. Liu, Y. Fan et al., "Workability and proportion design of pumping concrete based on rheological parameters," *Construction and Building Materials*, vol. 44, pp. 267–275, 2013.

[8] V. N. Nerella and V. Mechtcherine, "Virtual sliding pipe rheometer for estimating pumpability of concrete," *Construction and Building Materials*, vol. 170, pp. 366–377, 2018.

[9] M. S. Choi, Y. J. Kim, K. P. Jang, and S. H. Kwon, "Effect of the coarse aggregate size on pipe flow of pumped concrete," *Construction and Building Materials*, vol. 66, pp. 723–730, 2014.

[10] M. Nehdi and M. A. Rahman, "Effect of geometry and surface friction of test accessory on oscillatory rheological properties of cement pastes," *ACI Materials Journal*, vol. 101, no. 5, pp. 416–424, 2004.

[11] W. J. Cui, "Research and application of high performance concrete pumping construction technology in super high-rise structures," Ph D Thesis in Chinese, Tongji University, Shanghai, China, 2018.

[12] S. Jacobsen, L. Haugan, T. A. Hammer, and E. Kalogiannidis, "Flow conditions of fresh mortar and concrete in different pipes," *Cement and Concrete Research*, vol. 39, no. 11, pp. 997–1006, 2009.

[13] T. T. Ngo, E. H. Kadri, R. Bennacer, and F. Cussigh, "Use of tribometer to estimate interface friction and concrete boundary layer composition during the fluid concrete pumping," *Construction and Building Materials*, vol. 24, no. 7, pp. 1253–1261, 2010.

[14] D. Kaplan, F. D. Larrard, and T. Sedran, "Avoidance of blockages in concrete pumping process," *ACI Materials Journal*, vol. 102, no. 3, pp. 183–191, 2005.

[15] M. Choi, N. Roussel, Y. Kim, and J. Kim, "Lubrication layer properties during concrete pumping," *Cement and Concrete Research*, vol. 45, no. 1, pp. 69–78, 2013.

[16] M. S. Choi, Y. J. Kim, and S. H. Kwon, "Prediction on pipe flow of pumped concrete based on shear-induced particle migration," *Cement and Concrete Research*, vol. 52, no. 10, pp. 216–224, 2013.

[17] E. Secrieru, D. Cotardo, V. Mechtcherine, L. Lohaus, C. Schröfl, and C. Begemann, "Changes in concrete properties during pumping and formation of lubricating material under pressure," *Cement and Concrete Research*, vol. 108, pp. 129–139, 2018.

[18] D. Feys, K. H. Khayat, A. Perez-Schell, and R. Khatib, "Prediction of pumping pressure by means of new tribometer for highly-workable concrete," *Cement and Concrete Composites*, vol. 57, pp. 102–115, 2015.

[19] V. Mechtcherine, V. N. Nerella, and K. Kasten, "Testing pumpability of concrete using sliding pipe rheometer," *Construction and Building Materials*, vol. 53, pp. 312–323, 2014.

[20] S. H. Kwon, S. D. Jo, C. K. Park, J. H. Jeong, and S. H. Lee, "Prediction of concrete pumping: Part I—development of new tribometer for analysis of lubricating layer," *ACI Materials Journal*, vol. 110, no. 6, pp. 647–656, 2013a.

[21] S. H. Kwon, S. D. Jo, C. K. Park, J. H. Jeong, and S. H. Lee, "Prediction of concrete pumping: Part II—analytical prediction and experimental verification," *ACI Materials Journal*, vol. 110, no. 6, pp. 657–668, 2013b.

[22] K. P. Jang and M. S. Choi, "How affect the pipe length of pumping circuit on concrete pumping," *Construction and Building Materials*, vol. 208, pp. 758–766, 2019.

[23] S. Fataei, E. Secrieru, V. Mechtcherine, and N. Roussel, "A first-order physical model for the prediction of shear-induced particle migration and lubricating layer formation during concrete pumping," *Cement and Concrete Research*, vol. 147, Article ID 106530, 2021.

[24] E. Secrieru, W. Mohamed, S. Fataei, and V. Mechtcherine, "Assessment and prediction of concrete flow and pumping pressure in pipeline," *Cement and Concrete Composites*, vol. 107, Article ID 103495, 2019.

[25] Y. Li, J. Hao, Z. Wang, Z. Guan, J. Liu, and C. Jin, "Influence of ultra-high-rise pumping on microstructure and multi-scale mechanical properties of concrete based on X-ray CT and 3D

mesoscopic numerical simulation," *Construction and Building Materials*, vol. 267, Article ID 120980, 2020.

[26] Y. T. H. Cu, M. V. Tran, C. H. Ho, and P. H. Nguyen, "Relationship between workability and rheological parameters of self-compacting concrete used for vertical pump up to supertall buildings," *Journal of Building Engineering*, vol. 32, Article ID 101786, 2020.

Hindawi
Advances in Civil Engineering
Volume 2021, Article ID 7323934, 11 pages
https://doi.org/10.1155/2021/7323934

Research Article

Degradation of Shotcrete Materials Subjected to Sulfate and Chloride Attack in Varying Exposure Regimes

Ruiqiang Zhao,[1] Lihao Xu,[1] Jun Yang,[2] Yang Zou,[2] and Zhongya Zhang[2,3]

[1]*School of Materials Science and Engineering, Chongqing Jiaotong University, Chongqing 400074, China*
[2]*State Key Laboratory of Mountain Bridge and Tunnel Engineering, Chongqing Jiaotong University, Chongqing 400074, China*
[3]*School of Civil Engineering, Chongqing Jiaotong University, Chongqing 400074, China*

Correspondence should be addressed to Zhongya Zhang; zhangzhongya@cqjtu.edu.cn

Received 16 June 2021; Revised 25 July 2021; Accepted 29 September 2021; Published 11 October 2021

Academic Editor: Guoming Liu

Durability of in situ shotcrete under external sulfate attack was investigated, taking into consideration the addition of mineral admixtures, along with the presence of chloride ions. Three water-to-binder ratios (w/b), i.e., 0.35, 0.45, and 0.55, and two types of supplementary cementitious materials (SCMs), namely, fly ash (FA) and silica fume (SF), were considered in the current study. Two different laboratorial immersion regimes (continuously full immersion and partial immersion with cycling temperature and relative humidity) were carried out to induce chemical/physical sulfate attack. Results show that loss of strength was the typical feature of chemical sulfate attack on shotcrete, while surface spalling dominated in deterioration caused by physical sulfate attack. The presence of chloride ions can globally mitigate these deteriorations. Meanwhile, the lower w/b ratio proved to be efficient in increasing the resistance to both sulfate attacks. Adding fly ash (FA) in shotcrete mixtures enhanced the long-term performance but invited massive white efflorescence on surface layer under partial-immersion exposure condition. Silica fume (SF) admixture can compensate the undesired reduction of early-age strength caused by FA addition, but make these specimens more susceptible to sulfate attack. Mercury intrusion porosimetry (MIP) analysis, scanning electron microscopy (SEM), and X-ray diffraction (XRD) tests reveal that these consequences were strongly related to the refinement of microstructure resulted from pozzolanic reactions and hydration kinetics.

1. Introduction

Durability of cement-based materials, no matter emerging or conventional ones, has become a major issue in structural engineering over the last few decades [1, 2]. Among them, shotcrete durability is generally overlooked due to the reliable performance benefited from its technology of high speed jet, high early-age strength and the addition of the accelerator, which differs from conventional concrete materials [3]. However, they have the risk to be eroded by contaminated groundwater under harsh ambient environments, such as shotcrete liners of a tunnel underneath a refuse landfill. This groundwater is deleterious to shotcrete materials since it was contaminated by certain pernicious species, e.g., SO_4^{2-} and Cl^- or the combination of two. These ions have adverse impact on the durability of porous shotcrete materials, such as a collapse of mechanical strength. Free chloride ions mainly corrode the reinforcement steel, and sulfate salt attacks the concrete pastes inch by inch [4, 5]. Meanwhile, chloride ions were also detected to degrade cement pastes [5]. These adverse impacts may cause deterioration or even disintegration of shotcrete materials during service period. Since permanent shotcrete linings are increasingly adopted in road slope and underground tunneling engineering, durability of shotcrete under these aggressive environments is becoming crucial at the design and construction stage. Unfortunately, there is dearth of information on sulfate resistance of shotcrete materials in the presence of chloride ions. The corresponding performance-based testing was also rarely reported.

Shotcrete materials usually directly contact with groundwater or rock mass. The individual damage mechanisms caused by these ions on cement-based materials were well-documented in the last few decades [6–11]. Among

them, sulfate expansive products such as ettringite (E), gypsum (G), and thaumasite (T) and crystallization of sulfate salt (mainly sodium sulfate) are regarded as two main hypotheses [12–19]. As for chloride-induced damage, it is generally believed that Cl^- may combine with the C_3A phase to generate Friedel's salt [20–25]. However, dedicated durability studies on the sulfate resistance of shotcrete materials mixed with fly ash (FA)/silica fume (SF) were rare. This is mainly due to that in situ preparation of shotcrete materials is difficult and uncontrollable. Moreover, construction deficiency such as cavity may widely exist during the preparation of shotcrete materials, thus largely reducing the reliability of tests. In addition, many researchers studied the effects of exposure regimes on the sulfate attacking mechanism on concrete materials [26–30]. In these reports, it can be concluded that full immersion or partial immersion of concrete specimens in Na_2SO_4 solutions may result in different damages on concrete [31–38]. For dry-mix shotcrete, the w/b ratio is controlled by the volume of water mixing in the jet, rather than changing the amount of cementing materials. Clearly, this process greatly depends on the experience of workers, although predesign was well done. Thus, many studies on shotcrete shift the preparation stage to indoor, using small spray devices. However, this also alters the nature of shotcrete property, reducing reliability of the obtained results. On-site fly ash (FA) and silica fume (SF) are usually used to enhance the performance of shotcrete materials under various ambience environments [39]. Due to early-age strength of shotcrete is ensured by the addition of accelerator, thus, FA is added in the system to increase the long-term strength and workability. This is expected to increase the durability of shotcrete under severe exposure conditions. The early-age strength of shotcrete with addition of fly ash was reduced; silica fume can well compensate this deficiency [2]. However, durability of in situ mixing FA/SF shotcrete under sulfate-rich environments in presence of chloride ions remains to be thoroughly tested. Large number of researchers focused on chloride-induced corrosion of steel reinforcements [21, 23, 24]. In addition, only a few studies concerned on combined Cl^- and SO_4^{2-} attacking concrete materials [14, 25]. In these research studies, full immersion of concrete specimens in $MgSO_4$ with the coexistence of NaCl was mainly performed [25]. Clearly, the deterioration caused by $MgSO_4$ was mitigated or even delayed by the coexistence of NaCl from the results of these recent studies [14, 25].

Concerning the chloride-induced corrosion or sulfate attack mechanism on concrete materials, a number of achievements have been reported [40–45]. However, dedicated studies concerning sulfate resistance of shotcrete materials in presence of chloride ions are scarce. Most reports with respect to shotcrete materials mainly focused on development of accelerator products, additive or spray equipment, primarily aiming at enhancing the early-age strength and reducing rebound ratio [46–52]. In this study, thus a laboratory-scale accelerated corrosion test on shotcrete specimens (100 mm^3 cube) exposed to sodium sulfate solutions was performed, taking into account the presence of chloride ions. The erosion solutions were made using pure solution of 5% w/w Na_2SO_4 (S) and a mixed solution of 5% w/w Na_2SO_4 and 5% w/w NaCl (SC). In this way, the deterioration mechanism of shotcrete specimens exposed to Na_2SO_4 solution in the presence of Cl^- was preliminarily explored, by means of different analytical techniques and evaluation indicators.

2. Experimental Program

2.1. Materials. Universal ordinary portland cement (OPC, intermediate levels of OPC, C3A was 9%, P.O.42.5) was used as the main cementitious material (CMs). Two types of supplementary cementing materials (SCMs), i.e., Class I fly ash (FA) and silica fume (SF) were used as partial replacement of OPC to make binary binders. The low alkaline accelerator (AC), which contained $NaAlO_2$ and Ca_2SiO_4 (C_2S) as the main components, was used at a dose of 2.27% of the total binder content (i.e., 10.55 kg/m^3). Polycarboxylic acid (HRWRA) with a water reducing rate of 22.8% was used as a water reducing agent, and its dosage is 0.8% of the total binder content (3.712 kg/m^3). The details of the used materials are provided in Table 1.

Fine aggregate used in this study is natural river sand, fineness modulus is 2.61, having a continuous rating and a maximum size of 12 mm in the gravel as coarse aggregate. The specific gravity (kg/m^3) is 2650 and absorption (%) is 0.61. Both aggregates meet the requirements of JGJ/T 372-2016 [35] and JGJ 52-2006 [36].

2.2. Specimen Preparation. Single and binary binders were prepared using these pozzolana materials and cement (C). The dosage of mineral admixtures is at weight percentage (w/w) by the total binder content, as partially replacement of OPC. The detailed proportions of binders are summarized in Table 2. Different ratios of water-to-binder (w/b) were adopted in mixtures made by OPC.

The total cementitious materials (CM + SCMs = b) content was kept constant at 464 kg/m^3 for all binders in the current study. Seven concrete mixtures were tested in this study. Single binder (control) mixtures were prepared from 100% OPC, in which three w/b ratios (0.35, 0.45, and 0.55) were considered. Other two mixtures were prepared from blended binders with a certain replacement level of OPC having a uniform w/b ratio of 0.45. The proportions of the mixed design are listed in Table 3.

In the present experiment, the concrete mixture is prepared in line with JGJ/T 372-2016 [35]. The w/b ratio is controlled by the amount of water, and the cement is controlled. The design ratio of the mixture is shown in Table 3, which meets the requirements of JGJ/T 372-2016 [35], GB/T 50082-2009 [37], and GB/T 50081-2002 [38].

2.3. Exposure Regimes. After 28 days of initial curing, the shotcrete samples were immersed in mixed solutions (containing 5% w/w sodium sulfate alone (S) and 5% w/w sodium sulfate and 5% w/w sodium chloride (SC)) under different regimes. In addition, these solutions were prepared by dissolving anhydrous sodium sulfate (Na_2SO_4) and

Table 1: Chemical compositions and physical properties of cementitious materials and supplementary cementing materials [2].

Components/properties (w/w)	CMs	SCMs		Admixture
	OPC	FA	SF	Accelerator
Chemical compositions (%)				
Silicon oxide (SiO_2)	19.7	48.9	94.0	14.63
Aluminum oxide (Al_2O_3)	5.12	23.3	0.1	18.79
Ferric oxide (Fe_2O_3)	2.41	14.9	0.1	4.14
Calcium oxide (CaO)	60.5	3.8	0.4	32.73
Magnesium oxide (MgO)	3.31	0.7	0.4	0.65
Sulfur trioxide (SO_3)	3.01	0.2	1.3	0.27
Compound composition of clinker (%)				
Tricalcium silicate (C_3S)	61.8			
Dicalcium silicate (C_2S)	12.1			
Tricalcium aluminate (C_3A)	9.1			
Tetracalcium aluminoferrite (C_4AF)	7.6			
Physical properties				
Loss on ignition (%)	2.5	0.3	4.7	
Specific surface area (m^2/kg)	410	280	19530	
Specific gravity	3.17	2.08	2.12	

Table 2: Design proportions of blended binders.

Binders	Proportions
1	100% Ordinary Portland Cement
2	90% OPC + 10% w/w fly ash
3	90% OPC + 10% w/w silica fume

Table 3: Design of the mixing ratio of shotcrete mixtures per cubic meter.

Materials	PC35	PC45	PC55	FA10	SF10
OPC (kg)	464	464	464	418	418
FA (kg)				46	
SF (kg)					45
Coarse aggregate (kg)	907	907	907	907	907
Fine aggregate (kg)	890	890	890	890	890
Accelerator (kg)	10.55	10.55	10.55	10.55	10.55
Water reducing (kg)	3.712	3.712	3.712	3.712	3.712
Water (kg)	162.4	208.8	255.2	208.8	208.8
w/b (w/w)	0.35	0.45	0.55	0.45	0.45

sodium chloride (Na_2Cl) with a specified amount of water. All solutions were renewed monthly and the pH was controlled at a range of 6.0–8.0 by titration with diluted sulfuric acid solutions at regular time intervals (15 days). In this study, two exposure regimes were simultaneously carried out for a comprehensive comparison, i.e., continuously full immersion and partial immersion with cycling temperature and RH (relative humidity). They are described as follows:

(a) The regime of continuously full immersion is to fully submerge the cubic specimens within the erosion solutions up to 10 months, as shown in Figure 1.

(b) The regime of partial immersion is similar to the method by Nehdi et al. [19] in which the cubic specimens were partially submerged in erosion solutions subjected to cycles of temperature and RH, as shown in Figure 2. One cycle (15 days) consisted of two phases: 8 days of wetting curing at temperature of $20 \pm 2^{\circ}$C and RH of $90 \pm 5\%$, followed by 7 days of the drying phase at $45 \pm 2^{\circ}$C and $35 \pm 5\%$ RH in an environmental chamber. A total of 10 cycles (5 months) was performed in this study.

2.4. Tests

2.4.1. Mass Variation. Before testing, the spray cubes tested were air-dried in the laboratory at a temperature of 23°C (73.4°F) and a relative humidity of 70% until a constant mass was reached. Then, the mass of shotcrete cubic specimens at erosion time t, i.e., m_t, was measured using a balance with an accuracy of 0.01 g. Then, calculate the mass change according to

$$\text{Mass variation at} = \frac{(m_e - m_0)}{m_0} \times 100\%, \quad (1)$$

where m_0 is the initial mass before exposure and m_e is the mass of shotcrete cubic specimen after exposure period.

2.4.2. Strength. Compressive strength of the shotcrete cubic specimens under all regimes in erosion solutions was measured according to the GB 50081-2002 [38] (standard for the method of mechanical properties on ordinary concrete). All tests were performed on three identical samples, and the average of the three was used. Subsequently, the strength variation was calculated according to

$$\text{Strength variation at} = \frac{(\sigma_e - \sigma_0)}{\sigma_0} \times 100\%, \quad (2)$$

where σ_0 is the initial strength before exposure and σ_e is the strength of shotcrete cubic specimen after exposure period.

2.4.3. Microanalysis. Scanning electron microscopy (SEM) with energy dispersive X-ray analysis (EDX) are performed to study the microstructure and morphology of minerals in the deteriorating sample. At the specified time, let the sample air dry in the laboratory until no water is visible. Then, some of them were broken up and small debris (diameter less than 11 mm) was collected from different portions of samples. The collected debris was dried using a desiccator and then coated with gold on the surface before the SEM and EDX testing. The compositions of the corrosion products were analyzed using X-ray diffraction (XRD). After the exposure period, the deteriorating shotcrete specimens were taken out from the container. They were air-dried in the laboratory until no water can be seen. Then, some of them were broken up and small debris was collected from different portions of the specimen. The collected debris from identical portions was ground, and the obtained powder samples were going to pass the 200 μm sieve before the XRD testing.

2.4.4. Pore Structure. After 28 days of standard curing, small pieces were retrieved from selected samples to evaluate the pore size distribution using mercury intrusion porosimetry (MIP).

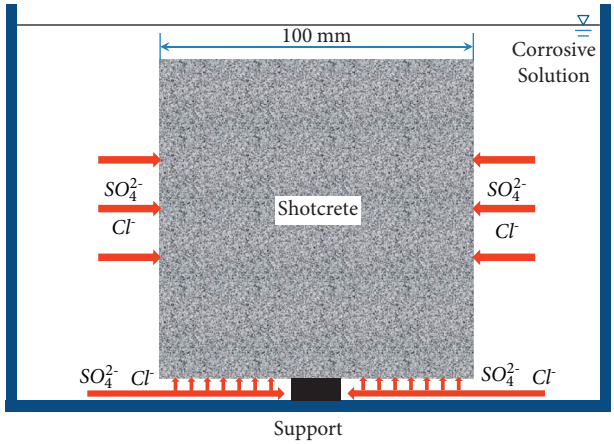

Figure 1: Continuously full immersion.

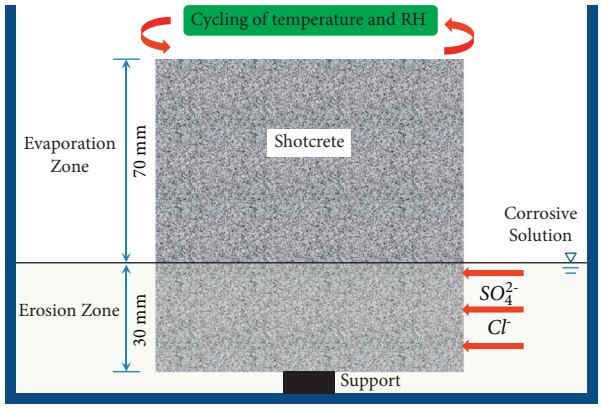

Figure 2: Partial immersion subjected to cycles of temperature and RH.

More specifically, the collected fragments were immediately plunged in an isopropanol solvent to stop cement hydration reactions. These samples were subsequently dried inside a desiccator until a constant mass was reached. The MIP measurements were performed using a MIP machine (Micromeritics AutoPore IV 9500). The surface tension was assumed to be 480 mN/m, and the contact angle was assumed to be 130° according to ASTM D4404 [53] (Standard Test Method for Determination of Pore Volume and Pore Volume Distribution of Soil and Rock by Mercury Intrusion Porosimetry).

3. Results

3.1. Continuously Full Immersion

3.1.1. Visual Inspection. The pore size distribution of various shotcrete mixtures measured by MIP is shown in Figure 3. The blended binary binders with addition of FA or SF have finer pore structures compared to the plain binders made with pure OPC. The total pore volume of various specimens follows PC > FA10 > SF10. For PC specimens, a lower w/b ratio results in a lower intruded pore volume. Mixtures made by OPC with a w/b ratio of 0.35 possess the lowest intruded pore volume. In addition, the mixtures incorporating 10% SF have the large volume of small pores (<0.05 μm in diameter).

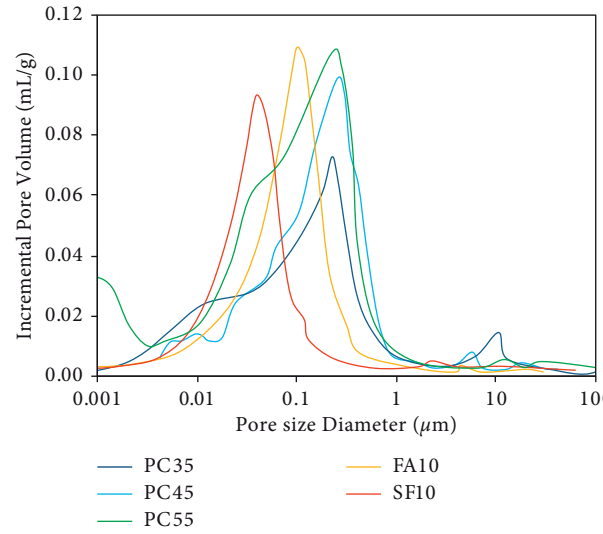

Figure 3: MIP results of specimens from various shotcrete mixtures before exposure.

After 10 months of continuously full immersion in both erosion solutions (S and SC), all shotcrete specimens remained visually intact except the specimens incorporating 10% SF (SF10). Overall, FA10 exhibited better resistance to surface deterioration in comparison with that of PC specimens. This may be attributed to consumption of calcium hydroxide (CH) in pozzolanic reactions, while it is the most vulnerable component under the ingress sulfate ions. Meanwhile, this process can increase the compactness of shotcrete, thereby to enhance permeability and porosity. Such refinement effect can reduce the formation of deleterious compounds such as ettringite and gypsum [28]. In addition, high aluminium oxide (Al_2O_3) and low tri-calcium aluminate (C_3A) content in FA10 specimens was not conducive to ettringite formation [8].

However, surface deterioration of SF10 was the most intense (see Figure 4), which signified the worst resistance to sulfate attack in comparison with others. This behavior was due to that low aluminium oxide (Al_2O_3) content in the SF system was favor to the formation of thaumasite ($CaSiO_3$ $CaCO_3$ $CaSO_4$ $15H_2O$) in SF10 specimens, as confirmed by XRD analysis shown in Figure 5. Since the XRD pattern of thaumasite is similar to ettringite, some main peaks are almost overlapping, such as the peak of 16° 2θ. Thus, we must identify thaumasite from some weak peaks, such as 26° 2θ and 28° 2θ.

It was reported that the formation of thaumasite can be a result of the reaction between calcium silicate hydrate, sulfate, and carbonate ions at low temperatures (0–5°C) and excess humidity environments [39]. However, thaumasite was also detected under CSA at higher temperature conditions [40]. Meanwhile, low Al_2O_3 content of SF binders resulted in a high SO_3/Al_2O_3 mole ratio in the system, which was prerequisite for thaumasite attack. Since calcium silicate hydrate (C-S-H) is necessary for thaumasite formation, this attack gradually destroys the binding ability of the cement paste by transforming C-S-H gels into a mush. For SF10

Figure 4: Visual appearance of SF10 specimens after exposure.

Figure 5: Visual appearance of various shotcrete specimens partially immersed in S solutions subjected to cycles of temperature and RH for 5 months.

specimens, spalling along the edges began at around 8 months of immersion. As can be seen, loss of cementitious matrix-aggregate bond was observed along the edges of specimens. As a consequence, edges and corners of the specimen were smoothed down. Moreover, the degree of surface deterioration of SF10 specimen in S solution was higher than that of SF10 specimen in SC solution. It has been well established that chloride can mitigate chemical sulfate attack on cement-based materials [14, 15]. Since the faster penetration capability of free chloride ions than that of sulfate ions, chloride may firstly combine with C_3A and calcium hydroxide (CH) to form Friedel's salt ($3CaO\ Al_2O_3\ CaCl_2\ 10H_2O$) before sulfate arrived. The possible reaction is expressed by

$$\begin{aligned} &Ca(OH)_2 + 2NaCl \text{®} CaCl_2 + 2Na + 2OH \\ &CaCl_2 + C_3A + 10H_2O \longrightarrow C_3A \cdot CaCl_2 \cdot 10H_2O \text{ (Friedel's salt).} \end{aligned} \tag{3}$$

These products thus can block tiny pores and cracks in the system, delaying or mitigating sulfate attack on shotcrete paste. In addition, the chloride ions' binding capacity can be

well improved due to higher volume of C-S-H (hydrated calcium silicate) gels in fly ash binders [41]. Free chloride ions may be bundled by C-S-H or C-A-H (hydrated calcium aluminate) to form Friedel's salt, thus blocking the tiny pores. As a result, sulfate attack on shotcrete can be mitigated in the presence of chloride. In sum, shotcrete mixtures made by binary binders incorporating 10% SF as partial replacement of OPC can facilitate sulfate attack on shotcrete, regardless of the presence of chloride or not. Addition of fly ash as partial replacement of OPC proved to be a valid countermeasure to reduce the degree of surface deterioration. In addition, concomitance of chloride in sulfate solutions can mitigate sulfate-induced deterioration on shotcrete, due to the block effect caused by the prior form of Friedel's salt.

3.1.2. Mass Variation. After 10 months of continuous full immersion in both erosion solutions (S and SC), all shotcrete specimens underwent variation of mass. Mass variations for shotcrete specimens made by single and blended binders after 10 months of full immersion in erosion solutions (S or SC) are reported in Table 4.

Overall, PC and FA10 specimens had a mass gain, while a slight loss of mass was found from SF10 specimens. More specifically, the maximal mass gain occurred from PC55 specimens, which was 2.13% in S solutions and 1.78% in SC solutions, respectively. Mass loss of SF10 specimens was 0.77% in S solutions and 0.22% in SC solutions, respectively. The mass variation of various shotcrete specimens follows: PC55 > PC45 > PC35 > FA10 > SF10. Clearly, the mass gain owed to water absorption, further hydration of binders and sulfate expansive products. The mass loss of SF10 attributed to surface spalling and the formation of thaumasite, which was expounded above. Meanwhile, a higher w/b ratio resulted in a larger mass gain in PC specimens. This may be due to a higher w/b ratio leads to higher water permeability and larger volume of pores on shotcrete pastes, thus giving rise to larger amount of ettringite formation and accumulation in these pores. In addition, the mass variation of a same type of shotcrete specimens was less in SC solutions compared to those in S solutions. This may be due to lower amount of secondary ettringite formed in SC solutions than in S solutions, due to inhibition by Friedel's salt. Clearly, the specimens incorporating 10% FA exhibited the best resistance to both S and SC solutions' attacks, followed by PC specimens with low w/b ratio. SF10 specimens displayed the worst behavior under sulfate attack. In addition, the specimens in SC solutions showed less mass change than those in S solutions.

3.1.3. Compression Strength Variation. Compressive strength variations for various shotcrete specimens incorporating different SCMs after 10 months of continuously full immersion in S and SC solutions are listed in Table 4. As a whole, all shotcrete specimens immersed in S and SC solutions suffered from strength loss, which indicated deterioration and damage. The strength loss of various shotcrete specimens follows: SF10 > PC55 > PC45 > PC35 > FA10. The maximal loss of strength happened in SF10 specimens, i.e., 15.26% in S solutions and 10.6% in SC solutions, respectively. This is as expected because the formation of thaumasite, along with ettringite and gypsum, seriously deteriorated SF10, which was confirmed above and by previous reports [39]. It is clear that the FA10 showed superior performance under sulfate or sulfate-chloride attacks compared to other mixtures. However, shotcrete specimens incorporating 10% SF exhibited the lowest resistance to sulfate or sulfate-chloride attacks under full immersion regime. Thus, the use of silica fume as a partial replacement of OPC is not suitable for shotcrete under sulfate bearing environments. In addition, the specimens in SC solutions showed less loss of strength than those in S solutions. These findings are in line with the results of mass and visual inspection, also conforming well to recent reports [39, 41].

Table 4: Variation of mass and compressive strength of various shotcrete specimens after exposure.

Type	Full immersion for 10 months				Partial immersion with cycle of temperature and RH for 5 months			
	Mass variation (%)		Compressive strength variation (%)		Mass variation (%)		Compressive strength variation (%)	
	S	SC	S	SC	S	SC	S	SC
PC35	1.04	0.73	−5.51	−2.83	0.35	0.12	−2.21	−2.11
PC45	1.56	1.21	−7.12	−4.31	−0.11	0.45	−3.93	−3.51
PC55	2.13	1.78	−9.81	−7.12	−0.59	0.32	−6.74	−5.27
FA10	0.61	0.42	−1.83	−0.71	−2.74	−1.88	1.42	2.14
SF10	−0.71	−0.22	−15.26	−10.6	−3.86	−3.49	−7.41	−6.25

3.2. Partial Immersion with Cycling Temperature and RH

3.2.1. Visual Inspection. For all specimens in partial immersion regime, white efflorescence appeared on surface of specimen portion above the solution level (upper portion) after one cycle. These white substances may be the deposition of soluble sodium sulfate salt (i.e., mirabilite). Results of SEM and EDX analysis from fragment samples from upper portion of specimens confirmed that white efflorescence was sodium sulfate [2, 19].

They came from salt solutions and moved up by capillary action and diffusion, due to concentration gradient as a result from moisture evaporation in upper portion of shotcrete specimens. Figure 5 depicts various shotcrete specimens after partial immersion in S solution with cycling temperature and RH for 5 months. For PC specimens, it can be observed that the amount of efflorescence follows PC55 > PC45 > PC35. Thus, higher w/b ratios may facilitate physical sulfate attack on shotcrete. It has been reported that higher w/b ratios facilitate physical sulfate attack on concrete materials, due to the higher permeability and porosity of concrete pastes with high w/b ratios [19]. Clearly, this conclusion is also suitable for shotcrete under sulfate attack.

For specimens made by binary binders, specimens containing 10% silica fume (SF10) exhibited more severe

spalling along the edges and corners than that containing 10% fly ash (FA10). This may be due to that the finer pore structure of SF10 leads to higher capillary suction, as confirmed by MIP results. Thus, more possibility of salt crystallization occurred on the specimen surface of upper portion. Under cycling of temperature and RH, phase transformation between mirabilite and thenardite took place on the surface layer of specimens [42]. Such repetitive crystallization of thenardite and mirabilite due to cyclic wetting and drying was responsible for the surface deterioration of shotcrete specimens exposed to sulfate solutions.

Partial replacement of OPC by SCMs can refine the pore structure and reduce the permeability of shotcrete, due to a reduction of the C_3A content in the binder (dilution effect), along with the consumption of calcium hydroxide (CH) in pozzolanic reactions [42]. However, this may not result in positive effect on the resistance to physical sulfate attack, since finer pore structure may lead to high capillary suction [18]. This is a powerful accomplice to physical sulfate attack on shotcrete. As expected, the deterioration degrees of specimens made by binary binders were higher than that made by pure OPC.

This phenomenon also existed in the presence of chloride ions. Figure 6 presents various shotcrete specimens after partial immersion in SC solution with cycling temperature and RH for 5 months. Clearly, addition of fly ash or silica fume as partial replacement of OPC can facilitate physical sulfate attack on shotcrete. In addition, the presence of chloride may mitigate the deterioration caused by sulfate expansive products, due to the formation of Friedel's salt.

3.2.2. Mass Variation. Mass variations of specimens made by different binders after partial immersion in S and SC solutions with cycling temperature and RH for 5 months are also provided in Table 4. The specimens made by binary binders suffered from mass loss in both S and SC solutions. This is due to spalling at edges and corners of specimens caused by salt crystallization. This indicates that partial replacement of OPC by fly ash or silica fume has adverse impact on the resistance to physical sulfate attack. For PC specimens, a higher w/b ratio results in more mass loss. This means that lowering the w/b ratio can enhance the resistance to physical sulfate attack on shotcrete, by decreasing porosity. Overall, the mass loss of specimens made by binary binders was more severe than those made by pure OPC, since more spalling occurred.

3.2.3. Compression Strength Variation. Compressive strength variations for various shotcrete specimens incorporating different SCMs after 5 months of partial immersion in S and SC solutions with cycling temperature and RH are presented in Table 4. All shotcrete specimens that were partially immersed in S and SC solutions suffered from strength loss, except for FA10. The strength loss of different specimens follows: SF10 > PC55 > PC45 > PC35 > FA10. For PC specimens, the higher w/b ratio exhibited less resistance to efflorescence, thus resulting in more loss of strength. Note that FA10 specimens gained compressive strength of 1.42% in S solutions and 2.14% in SC solutions, respectively. However, FA10 specimens showed more surface spalling and mass loss than those made by pure OPC. It is well acknowledged that binders incorporating SCMs such as fly ash can refine porosity, thus to increase capillary suction. Such improvement may increase the risk of physical sulfate attack on cement-based materials, since the supply of sulfate ions in drying portion of specimens mainly depends on capillary rise in tiny pore systems [20]. This is confirmed via the performance of SF10 specimens, which displayed more loss of strength than those made by pure OPC after 5 months under physical sulfate attack. However, it does not work for FA10 specimens. It is well known that fly ash, as an excellent mineral admixture as a partial replacement of OPC, is prominent in enhancing the long-term strength of cement-based materials. However, the use of fly ash should pay the price of a reduction in early-age strength of concrete. Generally, this deficiency can be improved by the addition of silica fume, especially for shotcrete, since partial replacement of OPC by silica fume can significantly improve the early-age strength of shotcrete. This is allimportant for shotcrete materials, since early-age strength of shotcrete is crucial in the design of these materials. However, silica fume has high content of silicium and low content of Al_2O_3. Such low-Al_2O_3 system is favor to the form of ettringite, even thaumasite if other conditions were fulfilled, such as low temperature. Anyhow, silica fume exhibits adverse impact on both chemical and physical sulfate attacks in current trials. This finding is also in accordance with that reported in [18–20, 24]. Probably, the gain of strength for FA10 specimens attributed to delayed enhancement in strength during the later exposure period. This point should require further attention, thus ongoing trials keep going on.

As a whole, shotcrete specimens containing 10% fly ash exhibited the best resistance to physical sulfate attack, while this is just the reverse for those containing 10% silica fume. Thus, fly ash seems to be a better mineral admixture to increase the resistance to physical sulfate attack. However, the use of silica fume as partial replacement of OPC should be cautious in practical. In addition, the specimens in SC solutions showed less loss of strength than those in S solutions. This indicates that the presence of chloride can mitigate damage caused by physical sulfate attack.

Results of microanalysis from powder samples confirmed that the periodic phase transformation between mirabilite and thenardite was the main driving mechanism of surface spalling, which is the typical feature of physical sulfate attack on shotcrete. In addition, it can be seen that weak peaks of ettringite and gypsum existed in the powder samples from the above portion of deteriorating specimens. This indicates that some sulfate may also react with CH and C-A-H to form these expansive products. Therefore, chemical sulfate attack also occurred under the exposure regime, aiming at inducing pure physical sulfate attack. Generally, it is regarded that physical sulfate attack cannot affect concrete strength, since the core is not influenced [19]. However, loss of strength still took place in concrete under physical attack. This seems to be inconsistent with the above findings and previous reports [31].

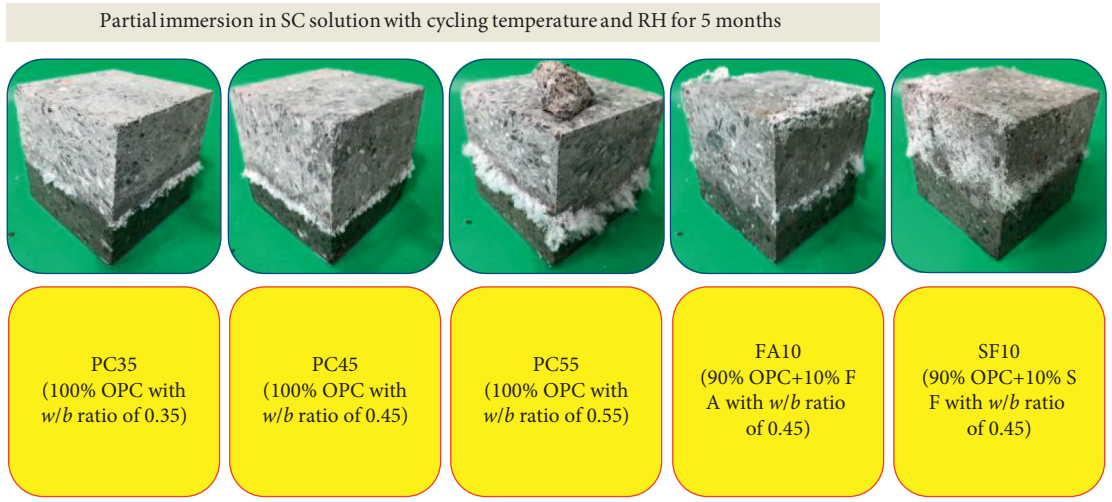

Figure 6: Visual appearance of various shotcrete specimens partially immersed in SC solutions subjected to cycles of temperature and RH for 5 months.

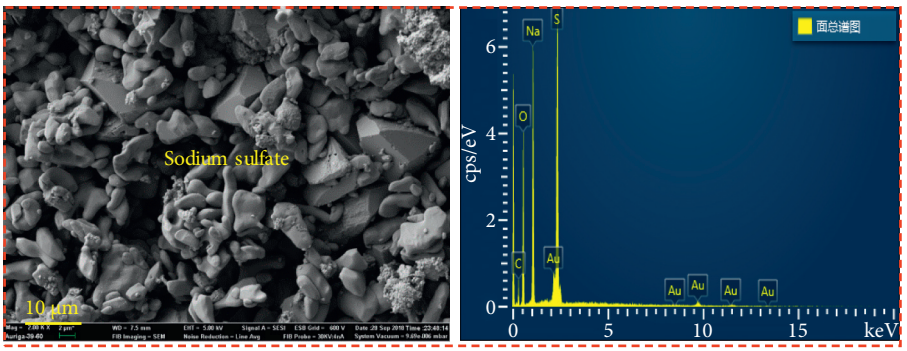

Figure 7: Test result of powder samples taken from the shotcrete specimen on the surface or superficial layer beneath the surface.

Different exposure regimes in lab-scale tests aim at inducing different attack mechanisms. For example, full immersion is responsible for chemical attack, while physical attack generally happens under partial immersion [28]. Loss of strength is the typical characteristics of chemical sulfate attack on cement-based materials, since C_3A and hydrated aluminate phases were destroyed by sulfate [2]. Under physical sulfate attack, deterioration often stays on the specimen surface or beneath the surface, in the form of spalling and flaking [19]. Crystallization and phase transformation of sulfate salt may be the main driving mechanism of this attack [20]. Generally, it is regarded that physical sulfate attack does not affect strength of concrete. However, small size specimens with high specific surface area were primarily used in the lab to perform physical sulfate attack test on concrete. These specimens can be completely destroyed under harsh physical attack regime, such as drastic drying-wetting cycles or high-concentration sodium sulfate solutions. Therefore, larger specimens (100 mm^3 cubes) were used to experience physical attack in this study. Under this consideration, the test period was highly increased due to that specimens with large specific surface area were hard to be attacked in comparison with small specimens. Fortunately, some important details are found. By the microanalysis of samples from interior concrete core, no sulfate reaction products such as ettringite or gypsum were detected. More interesting, traces of ettringite and CH were simultaneously detected in the powder samples taken from around 20 mm beneath the specimen surface. However, no sodium sulfate crystal was found from these powder samples. In other words, sodium sulfate crystals such as mirabilite and thenardite were only detected on the specimen surface or the superficial layer beneath the surface, as shown in Figure 7.

This indicates that shotcrete cores will not be deteriorated by salt crystallization subjected to physical sulfate attack. Meanwhile, coexistence of chemical and physical sulfate attack on conventional physical sulfate attack on shotcrete. Evaporation of water in the upper portion of shotcrete specimens' results in a remarkable gradient of concentration between the upper portion and the lower portion, especially near the surface. This gradient of concentration significantly affects the transportation kinetics of sulfate ions in the matrix. If chloride exists, the ingress of sulfate ions into core may be impeded by the prior formation of Friedel's salt, since the penetration rate of free chloride ions in concrete is faster than that of sulfate ions. Therefore, physical spalling mainly deteriorates the surface of specimens, but chemical reactions

may attack concrete interior. That is why the loss of strength from shotcrete specimens under physical sulfate attacks in the current study. In addition, the current tests will be continuous; more details concerning external sulfate attack on shotcrete specimens (100 mm^3 cubes) in the presence of chloride will be obtained. In fact, this consideration of the specimen size is closer to practical, such as shotcrete lining of a tunnel. However, shotcrete lining is typically attacked by groundwater contaminated by pernicious species at only one surface. Such exposure regime is far away from that of piers or piles. Thus, the resulting transportation kinetics and damage mechanism on shotcrete may be different. This point requires further attention, since it is vital in the shotcrete design of practical engineering.

4. Conclusions

Durability of shotcrete with addition of mineral admixtures under external sulfate attack in the presence of chloride was investigated. From the present study, the following conclusions can be drawn:

) (iUnder conventional chemical sulfate attack on shotcrete, loss of strength is the typical feature. For partial immersion with cycling temperature and RH, physical sulfate attack in the form of surface spalling is the main type of deterioration.

(ii) Shotcrete specimens incorporating 10% FA as partial replacement of OPC achieved adequate resistance to chemical sulfate attack. However, such specimens suffered from surface deterioration under the exposure of partial immersion with cycling temperature and RH. Shotcrete with addition of 10% SF exhibited the least resistance to both chemical and physical sulfate attack, regardless of the presence of chloride. This is due to that low aluminium oxide (Al_2O_3) and tri-calcium aluminate (C3A) content of silica fume system is favor to the formation of ettringite and thaumasite.

(iii) Shotcrete specimens with lower w/b ratios show good resistance to both chemical and physical sulfate attack, due to its higher compactness and lower porosity and permeability.

(iv) The concomitant presence of chloride can mitigate the deterioration caused by external sulfate attack. This is due to that chloride combined C_3A and calcium hydroxide (CH) to form Friedel's salt. This product can block shotcrete pores, thereby to forestall the further ingress of sulfate ions.

(v) Under physical sulfate attack on shotcrete, the specimen size has an influence on the transportation kinetics of sulfate ions in matrix, subsequently the nature of attack mechanism. For 100 mm^3 cubic specimens used in this study, salt crystallization was only detected in the surface layer of specimens. Shotcrete cores were at risk of chemical sulfate attack. The effect of the specimen size on physical sulfate attack should require further attention.

Data Availability

The data used to support the findings of this study are included within the article.

Conflicts of Interest

The authors declare that they have no conflicts of interest.

Acknowledgments

This work was sponsored by the China Postdoctoral Science Foundation (Grant no. 2021M693919), the Natural Science Foundation of Chongqing, China (Grant no. cstc2020jcyj-bshX0007), and the National Natural Science Foundation of China (nos. 51808082 and 52008066).

References

[1] S. W. Tang, Y. Yao, C. Andrade, and Z. J. Li, "Recent durability studies on concrete structure," *Cement and Concrete Research*, vol. 78, pp. 143–154, 2015.

[2] Z. Zhang, X. Jin, and W. Luo, "Long-term behaviors of concrete under low-concentration sulfate attack subjected to natural variation of environmental climate conditions," *Cement and Concrete Research*, vol. 116, pp. 217–230, 2019.

[3] Z. Zhang, X. Jin, and W. Luo, "Mechanical responses of shotcrete specimens in direct shear tests," *Construction and Building Materials*, vol. 188, pp. 305–313, 2018.

[4] N. Shanahan and A. Zayed, "Cement composition and sulfate attack," *Cement and Concrete Research*, vol. 37, no. 4, pp. 618–623, 2007.

[5] Y. Zhao, H. Ding, and W. Jin, "Development of the corrosion-filled paste and corrosion layer at the steel/concrete interface," *Corrosion Science*, vol. 87, pp. 199–210, 2014.

[6] Y. Zhao, X. Zhang, and W. Jin, "Influence of environment on the development of corrosion product-filled paste and a corrosion layer at the steel/concrete interface," *Corrosion Science*, vol. 124, 2017.

[7] C. Fu, N. Jin, H. Ye, X. Jin, and W. Dai, "Corrosion characteristics of a 4-year naturally corroded reinforced concrete beam with load-induced transverse cracks," *Corrosion Science*, vol. 117, 2017.

[8] F. Bellmann, W. Erfurt, and H.-M. Ludwig, "Field performance of concrete exposed to sulphate and low ph conditions from natural and industrial sources," *Cement and Concrete Composites*, vol. 34, no. 1, pp. 86–93, 2012.

[9] J. L. Provis, A. Palomo, and C. Shi, "Advances in understanding alkali-activated materials," *Cement and Concrete Research*, vol. 78, pp. 110–125, 2015.

[10] K. L. Scrivener, P. Juilland, and P. J. M. Monteiro, "Advances in understanding hydration of portland cement," *Cement and Concrete Research*, vol. 78, pp. 38–56, 2015.

[11] M. Collepardi, "A state-of-the-art review on delayed ettringite attack on concrete," *Cement and Concrete Composites*, vol. 25, no. 4-5, pp. 401–407, 2003.

[12] A. Ghazy and M. T. Bassuoni, "Resistance of concrete to different exposures with chloride-based salts," *Cement and Concrete Research*, vol. 101, no. 11, pp. 144–158, 2017.

[13] M. Zajac, P. Durdzinski, C. Stabler, J. Skocek, D. Nied, and M. Ben Haha, "Influence of calcium and magnesium carbonates on hydration kinetics, hydrate assemblage and microstructural development of metakaolin containing

composite cements," *Cement and Concrete Research*, vol. 106, pp. 91–102, 2018.

[14] K. Sotiriadis, E. Nikolopoulou, and S. Tsivilis, "Sulfate resistance of limestone cement concrete exposed to combined chloride and sulfate environment at low temperature," *Cement and Concrete Composites*, vol. 34, no. 8, pp. 903–910, 2012.

[15] M. Maes and N. De Belie, "Resistance of concrete and mortar against combined attack of chloride and sodium sulphate," *Cement and Concrete Composites*, vol. 53, no. 10, pp. 59–72, 2014.

[16] I. Tai, S. H. P. Cavalaro, I. Segura, and A. Aguado, "Alternative methodology to consider damage and expansions in external sulfate attack modeling," *Cement and Concrete Research*, vol. 63, no. 63, pp. 105–116, 2014.

[17] F. Girardi, W. Vaona, and R. Di Maggio, "Resistance of different types of concretes to cyclic sulfuric acid and sodium sulfate attack," *Cement and Concrete Composites*, vol. 32, no. 8, pp. 595–602, 2010.

[18] M. Nehdi and M. Hayek, "Behavior of blended cement mortars exposed to sulfate solutions cycling in relative humidity," *Cement and Concrete Research*, vol. 35, no. n 4, pp. 731–742, 2005.

[19] M. L. Nehdi, A. R. Suleiman, and A. M. Soliman, "Investigation of concrete exposed to dual sulfate attack," *Cement and Concrete Research*, vol. 64, pp. 42–53, 2014.

[20] M. T. Bassuoni and M. M. Rahman, "Response of concrete to accelerated physical salt attack exposure," *Cement and Concrete Research*, vol. 22, 2015.

[21] X. Zhang, M. Li, L. Tang et al., "Corrosion induced stress field and cracking time of reinforced concrete with initial defects: analytical modeling and experimental investigation," *Corrosion Science*, vol. 120, pp. 158–170, 2017.

[22] M. Otieno, "Sensitivity of chloride-induced corrosion rate of steel in concrete to cover depth, crack width and concrete quality," *Materials and Structures*, vol. 50, no. 1, p. 9, 2017.

[23] A. Michel, A. O. S. Solgaard, B. J. Pease, M. R. Geiker, H. Stang, and J. F. Olesen, "Experimental investigation of the relation between damage at the concrete-steel interface and initiation of reinforcement corrosion in plain and fibre reinforced concrete," *Corrosion Science*, vol. 77, no. 6, pp. 308–321, 2013.

[24] W. Nguyen, J. F. Duncan, G. Jen, and C. P. Ostertag, "Influence of matrix cracking and hybrid fiber reinforcement on the corrosion initiation and propagation behaviors of reinforced concrete," *Corrosion Science*, vol. 140, 2018.

[25] K. Sotiriadis, E. Nikolopoulou, S. Tsivilis, A. Pavlou, E. Chaniotakis, and R. N. Swamy, "The effect of chlorides on the thaumasite form of sulfate attack of limestone cement concrete containing mineral admixtures at low temperature," *Construction and Building Materials*, vol. 43, pp. 156–164, 2013.

[26] F. Chen, J. Gao, B. Qi, D. Shen, and L. Li, "Degradation progress of concrete subject to combined sulfate-chloride attack under drying-wetting cycles and flexural loading," *Construction and Building Materials*, vol. 151, pp. 164–171, 2017.

[27] B. Frank, M. . Bernd, and J. Stark, "Influence of sulfate solution concentration on the formation of gypsum in sulfate resistance test specimen," *Cement and Concrete Research*, vol. 36, no. 2, pp. 358–363, 2006.

[28] M. T. Bassuoni and M. L. Nehdi, "Durability of self-consolidating concrete to different exposure regimes of sodium sulfate attack," *Materials and Structures*, vol. 42, no. 8, pp. 1039–1057, 2009.

[29] M. T. Bassuoni and M. L. Nehdi, "Durability of self-consolidating concrete to sulfate attack under combined cyclic environments and flexural loading," *Cement and Concrete Research*, vol. 39, no. 3, pp. 206–226, 2009.

[30] R. M. Espinosa, L. Franke, and G. Deckelmann, "Phase changes of salts in porous materials: crystallization, hydration and deliquescence," *Construction and Building Materials*, vol. 22, no. 8, pp. 1758–1773, 2008.

[31] Z. Liu, D. Deng, G. D. Schutter, and Z. Yu, "Chemical sulfate attack performance of partially exposed cement and cement+fly ash paste," *Construction and Building Materials*, vol. 28, no. 1, pp. 230–237, 2012.

[32] R. J. Flatt, "Salt damage in porous materials: how high supersaturations are generated," *Journal of Crystal Growth*, vol. 242, no. 3-4, pp. 435–454, 2002.

[33] G. W. Scherer, "Stress from crystallization of salt," *Cement and Concrete Research*, vol. 34, no. 9, pp. 1613–1624, 2004.

[34] S. Zhutovsky and R. Douglas Hooton, "Experimental study on physical sulfate salt attack," *Materials and Structures*, vol. 50, no. 1, p. 54, 2017.

[35] Jgj/T 372-2016, *Technical Specification for Application of Sprayed concrete*, China Architecture & Building Press, Beijing, China, 2016.

[36] Jgj 52-2006, *Standard for Technical Requirements and Test Method of Sand and Crushed Stone (Or Gravel) for Ordinary Concrete*, China Architecture & Building Press, Beijing, China, 2016.

[37] Gb/T 50082-2009, *Standard for Test Methods of Long-Term Performance and Durability of Ordinary concrete*, China Architecture & Building Press, Beijing, China, 2009.

[38] Gb 50081-2002, *Standard for Method of Mechanical Properties on Ordinary Concrete*, China Architecture and Building Press, Beijing, China, 2002.

[39] M. F. Najjar, M. L. Nehdi, A. M. Soliman, and T. M. Azabi, "Damage mechanisms of two-stage concrete exposed to chemical and physical sulfate attack," *Construction and Building Materials*, vol. 137, pp. 141–152, 2017.

[40] M. Jin, S. Gao, L. Jiang, H. Chu, M. Lu, and F. F. Zhi, "Degradation of concrete with addition of mineral admixture due to free chloride ion penetration under the effect of carbonation," *Corrosion Science*, vol. 138, 2018.

[41] T. Aye and C. T. Oguchi, "Resistance of plain and blended cement mortars exposed to severe sulfate attacks," *Construction and Building Materials*, vol. 25, no. 6, pp. 2988–2996, 2011.

[42] J.-P. Won, U.-J. Hwang, and S.-J. Lee, "Enhanced long-term strength and durability of shotcrete with high-strength C 12 A 7 mineral-based accelerator," *Cement and Concrete Research*, vol. 76, pp. 121–129, 2015.

[43] P. Choi, J. H. Yeon, and K.-K. Yun, "Air-void structure, strength, and permeability of wet-mix shotcrete before and after shotcreting operation: the influences of silica fume and air-entraining agent," *Cement and Concrete Composites*, vol. 70, pp. 69–77, 2016.

[44] P. Bamonte, P. G. Gambarova, and A. Nafarieh, "High-temperature behavior of structural and non-structural shotcretes," *Cement and Concrete Composites*, vol. 73, pp. 42–53, 2016.

[45] P. B. Trujillo, M. Jolin, B. Massicotte, and B. Bissonnette, "Bond strength of reinforcing bars encased with shotcrete," *Construction and Building Materials*, vol. 169, pp. 678–688, 2018.

[46] M. Khooshechin and J. Tanzadeh, "Experimental and mechanical performance of shotcrete made with nanomaterials

and fiber reinforcement," *Construction and Building Materials*, vol. 165, pp. 199–205, 2018.

[47] J. Wang, D. Niu, and Y. Zhang, "Mechanical properties, permeability and durability of accelerated shotcrete," *Construction and Building Materials*, vol. 95, pp. 312–328, 2015.

[48] D.-T. Niu, Y.-D. Wang, R. Ma, J.-B. Wang, and S.-H. Xu, "Experiment study on the failure mechanism of dry-mix shotcrete under the combined actions of sulfate attack and drying-wetting cycles," *Construction and Building Materials*, vol. 81, pp. 74–80, 2015.

[49] J. O. Ukpata, P. A. Muhammed Basheer, and L. Black, "Expansion of CEM I and slag-blended cement mortars exposed to combined chloride-sulphate environments," *Cement and Concrete Research*, vol. 123, Article ID 105794, 2019.

[50] J. O. Ukpata, P. A. M. Basheer, and L. Black, "Slag hydration and chloride binding in slag cements exposed to a combined chloride-sulphate solution," *Construction and Building Materials*, vol. 195, pp. 238–248, 2019.

[51] M. Fathima Suma, M. Santhanam, and A. V. Rahul, "The effect of specimen size on deterioration due to external sodium sulphate attack in full immersion studies," *Cement and Concrete Composites*, vol. 114, Article ID 103806, 2020.

[52] Y. Cao, L. Guo, B. Chen, and J. Wu, "Thermodynamic modelling and experimental investigation on chloride binding in cement exposed to chloride and chloride-sulfate solution," *Construction and Building Materials*, vol. 246, Article ID 118398, 2020.

[53] ASTM D4404, *Standard Test Method for Determination of Pore Volume and Pore Volume Distribution of Soil and Rock by Mercury Intrusion Porosimetry*, ASTM International, West Conshohocken, PA, USA, 2010.

Hindawi
Advances in Civil Engineering
Volume 2021, Article ID 9360708, 10 pages
https://doi.org/10.1155/2021/9360708

Research Article

Research on the Creep Characteristics of Thermal Insulation Shotcrete under the Action of Temperature and Humidity Circulation

Jinsong Zhang[1,2], **Yaxing Wang**[2], **Junjun Liu**[2] **and Jiuqun Zou**[2]

[1]*State Key Laboratory of Mining Response and Disaster Prevention and Control in Deep Coal Mine, Anhui University of Science and Technology, Anhui, Huainan 232000, China*
[2]*School of Civil Engineering and Architecture, Anhui University of Science and Technology, Anhui, Huainan 232000, China*

Correspondence should be addressed to Jiuqun Zou; jqzou1225@sina.com

Received 25 April 2021; Revised 29 July 2021; Accepted 13 August 2021; Published 19 August 2021

Academic Editor: Guoming Liu

In order to explore the creep characteristics of thermal insulation shotcrete under the action of temperature and humidity circulation, a series of uniaxial compression creep tests were carried out with different cycles of temperature and humidity and hierarchical loading conditions. The test results show that the axial creep deformation and creep strain of the thermal insulation shotcrete specimens increase with the increase of the number of drying and wetting cycles under normal temperature water bath condition. After 28 cycles, the deformation value becomes larger obviously, and the creep strain increases greatly in the precycle period. The thermal insulation shotcrete axial steady-state creep rate increases nonlinearly with the increase of the number of drying and wetting cycles under different stress levels. When the number of adjacent cycles is 0–3, the average increase is larger, and the axial steady-state creep rate of thermal insulation shotcrete for 28 cycles increases with the increase of water bath temperature. The instantaneous deformation modulus of thermal insulation shotcrete decreases logarithmically with the increase of the number of drying and wetting cycles, and the total deterioration degree of the average instantaneous deformation modulus increases gradually, but the deterioration degree between adjacent cycles decreases successively. The thermal insulation shotcrete specimens with 3 cycles of fracture were mainly stretched, and with the increase of the water bath temperature, the specimen was damaged by shear failure. When the water bath temperature is 40°C, the fracture degree of the specimen increases first and then decreases with the increase of the number of cycles.

1. Introduction

Nowadays, some practical projects often face high-temperature damage problems [1, 2], such as the environment in which certain roadways are located in the process of coal mining. Solving the temperature problems encountered in the project is of practical significance to improving the project environment. Zhang and Xiao-Qiang [3] used inorganic sprayed concrete materials as the insulation layer and developed high-performance heat-insulating lightweight aggregate sprayed concrete that can be applied in different rock temperature environments. Yao and Pang [4] selected a variety of thermal insulation materials, and a new type of thermal insulation concrete was obtained through a cross test, which found a good thermal insulation effect that its thermal conductivity was only 1/8 of that of ordinary concrete, At present, there have been more and more research studies on insulated shotcrete (HS), and exploring the relevant characteristics of HS has certain theoretical value. In some roadway excavation projects, HS as the sprayed layer of the roadway will change the moisture content of the surrounding rock due to various effects [5–8] and the changes of temperature stress [9], and the ventilation situation in the roadway may cause the insulated sprayed concrete to be at the state of alternation of wetting and drying; in the indoor test, dry and water bath alternate treatments are performed on the sample to simulate the dry-wet cycles process. Regarding the dry-wet cycles of concrete, domestic and foreign

scholars have conducted a lot of research studies in recent years. Zhao Gao-wen et al. [10] found that the underground cast-in-situ concrete structure often suffers from multiple ion dry and wet alternate compound erosion. The indoor test conditions are used to simulate the compound erosion process of underground cast-in-place concrete structures in actual projects. The size, quality, and compressive strength changes of the specimens and the distribution of sulfate at different depths were measured. Li Bei-xing et al. [11] carried out the semi-immersion dry-wet cycles test of three kinds of concrete with large amount of mineral admixture in sodium sulfate solution, which studied the chemical corrosion damage mechanism of concrete and the role of mineral admixture in it. Chen Wei-Kang and Liu [12] systematically studied the coupling transmission process of moisture and polyions in concrete under alternating wet and dry conditions. Zhang and Sun [13] used drying and wetting cycles and full immersion methods to carry out Cl^{-1} permeation comparison tests, which found that the dry-wet cycles accelerate the migration of Cl^{-1} into the concrete. Yao et al. [14] studied the influence of the chloride dry-wet cycles on the average shear strength and slip at the interface between fiber braid-mesh reinforced concrete (TRC) and existing concrete through double-sided shear test. The test results show that with the increase of the number of chloride salt drying and wetting cycles, the interface performance between TRC and existing concrete decreases. Xue-Qiang et al. [15] explored the effect of drying and wetting cycles on the resistance of concrete to chloride ion penetration. It was found that the effect of dry-wet cycles roughened the surface pore structure of concrete specimens, increased the pore content of pore diameters >50 nm, and significantly increased the free and total chloride ion concentration. Jiang and Di-Tao [16] obtained the full stress-strain curve equation under uniaxial compression through the action of concrete sulfate erosion and dry-wet cycles and found a method to determine the damage layer concrete stress-strain equation. Chen et al. [17] used NMR technology to collect T2 spectrum and porosity under different wetting and drying cycles, analyzed the pore development and porosity change under wetting and drying cycles tests, and obtained the damage rule of recycled concrete under wetting and drying cycles environment. Yue et al. [18] studied the porosity, ultrasonic sound velocity, and compressive strength of concrete specimens with different numbers of drying and wetting cycles. Jiang Shao-fei et al. [19] carried out the corrosion degradation test of concrete's elastic modulus, compressive strength, and CFRP-concrete shear specimen interface bond performance under different dry-wet cycles. Qiang et al. [20] presented the physical and mechanical characteristics of AAS mortars (i.e., visual appearance, compressive/flexural strength, mass change, capillary porosity, and water sorptivity), as well as mineralogical and chemical parameters were determined using XRD, FTIR, DSC, and BSE. Findings were compared to Portland cement (PC) and high sulfate resistant (HSR) samples. Guo et al. [21] The results show that with the prolongation of the dry-wet cycles, the deterioration degree of concrete increases first and then decreases. The microstructure analysis shows that the corrosion depth of sulfate erosion increases with the increase of dry-wet cycles. Dehestani et al.' [22] experimental study found that as the number of wet and dry cycles increases, the tensile and shear fracture toughness of concrete decreases. Daqing et al. [23] studied the relationship between compressive strength and splitting strength of recycled concrete under the action of dry-wet cycles. Cao et al.' [24] experimental results show that compared with the conditions of long-term immersion in water, the wetting and drying cycles will significantly increase the creep deformation of the axial compressive fly ash concrete members, mainly in the early four dry-wet cycles.

There are many studies on the relevant properties of concrete under different dry-wet cycles. Many scholars have mainly studied the compressive, tensile strength, and anti-permeability properties of samples under different dry-wet cycles. However, concrete is often subjected to the long-term effect of external stress in some projects, so the study of the creep characteristics of concrete samples after different dry-wet cycles has practical significance for the long-term strength evaluation of concrete in some projects. Furthermore, due to the increase in temperature of some projects [25], the study of the changes in the creep mechanical properties of concrete samples after different water bath temperature treatments and different dry-wet cycles has provided the theoretical reference value for concrete engineering to a certain extent.

In order to better study the creep characteristics of concrete under different water bath temperatures and different dry-wet cycles, this study takes HS as the research object and uses the RDL-200 electronic creep relaxation tester to test samples after different water bath temperatures and dry-wet cycles. The uniaxial compression creep test was carried out to study the influence of different dry-wet cycles and different water bath temperatures on the relative creep mechanical properties of HS and revealed the mechanism of the impact of different dry-wet cycles and water bath temperatures on HS.

2. The Design of the Temperature and Humidity Cycles Test

2.1. Test Instrument. In this test, the water bath process of specimens should be carried out in the digital constant temperature circulating water tank HH-420, and the temperature control range is room temperature to 100°C, as shown in Figure 1(a); the drying process should be carried out in the DHG constant temperature drying oven, and the temperature control range is 10–300°C, as shown in Figure 1(b). The creep test should use the RDL-200 electronic creep relaxation tester, the test force measurement error is not more than ±0.5% of the indicated value, and the deformation measurement range is 0–10 mm. The resolution is 0.001 mm, as shown in Figure 1(c).

2.2. Mixture Ratio Design. The raw materials for the test are selected as follows according to the specification [26]: the sand is fine sand, the stone is Huainan melon seed slices

(a) (b) (c)

Figure 1: Test apparatus. (a) HH-420 constant temperature circulating water tank. (b) DHG constant temperature drying oven. (c) RDL series electronic creep relaxation test.

stone of 5–10 mm, and cement is P·O42.5 ordinary Portland cement produced in Bagongshan, Huainan, the fly ash is grade I fly ash, and the mixing water is tap water. The optimum mix proportion is calculated according to grey correlation degree from the previous 9 groups of specimens, as given in Table 1.

2.3. Specimen Making. According to the specification [27], the test should use the mold with the size of φ 50 mm $*$ 100 mm, then put the mode into the saturated $Ca(OH)_2$ solution for curing for 28 days, and then take it out and grind the rough end face, as shown in Figure 2.

2.4. Test Scheme. The thermal insulation shotcrete specimen was dried in the drying box for 8 h, took out and cooled for 30 min, and then put into the constant temperature water bath box for water bath for 16 h, which was a dry-wet cycle. The temperature of the first drying of the specimen should be 105°C, and the later drying temperature should be 60°C. The so-called temperature and humidity cycles are the process of specimen cycling in different water bath temperatures. The specimens were divided into four groups and placed in four different water bath temperatures of room temperature, 40°C, 60°C, and 80°C for circulation. Each group of 12 blocks underwent 3, 7, 14, and 28 times of dry-wet cycles, respectively. After the end of the cycle, prevent contact with air, seal, and store for the next step of the test. The specific steps are shown in Figure 3. The creep test is carried out by step loading, and the creep loading value is determined by the average value of uniaxial compressive strength after the specimen reaches the curing age. Taking 40% of the compressive strength as the initial stress value, the step loading is divided into five stages. The stress increment of each stage is 2.598 MPa, the stress duration of each stage is 12 h, the data acquisition interval is 5 s during loading, and the acquisition interval for stress holding is 10 min. The specific axial graded stress is given in Table 2, The specific test scheme is given in Table 3.

3. The Results and Analysis of the Creep Test

Thanks to the internal heterogeneity of concrete specimens, and the grading stress value is determined according to the average value of compressive strength of several specimens; so when the axial graded stress exceeds the compressive strength of the specimen itself, the specimen will experience creep failure, and its deformation will change greatly when compared with the deformation under other stresses. Therefore, only the influences of the first four stages of temperature and humidity cycles on the axial strain, axial creep strain, steady creep rate, and instantaneous deformation modulus of thermal insulation concrete are studied.

3.1. Analysis of Creep Characteristics of Specimens under Different Dry-Wet Cycles. The creep curve of HS specimen with different drying and wetting cycles under normal temperature water bath is shown in Figure 4.

3.1.1. Creep Curve Analysis of Samples with Different Dry-Wet Cycles. The results show that the axial strain of thermal insulation shotcrete specimen increases with the increase of loading stages. The instantaneous deformation occurs at the moment of stress loading, and creep occurs when the stress is constant. The slope of early creep curve gradually decreases with time, showing deceleration creep, and then, the slope of curve basically tends to be a constant value, showing steady-state creep. As shown in Figure 4, the instantaneous deformation and creep deformation of thermal insulation shotcrete specimen increase with the increasing times of the dry and wet cycles, and the deformation values after cycling for 28 times increase obviously.

3.1.2. Effect of Dry-Wet Cycles on Axial Creep Strain of Specimens. The change of axial creep strain of thermal insulation shotcrete under different stress levels and cycle times is shown in Figure 5. It can be seen from the figure that the axial creep strain changing rule of thermal insulation shotcrete is basically the same under different stress levels, and the axial creep strain increases with the increasing times of the drying and wetting cycles. The results show that the axial creep strain is larger under the first-order stress and high stress level. The reason is that the compactness of the concrete itself is poor for manufacture factors; thus, the inside of the concrete itself exist cracks. The crack shrinks

Table 1: Mixture ratio of specimen (kg/m^3).

Ceramsite	Taunsa	Basalt fiber	Plant fiber	Vitrified microsphere	Sand	Gravel	Cement	Fly ash	Water-reducing agent	Water
58.142	66.448	5.26	0.4	9	764.152	772.458	427.5	47.5	3.8	213.8

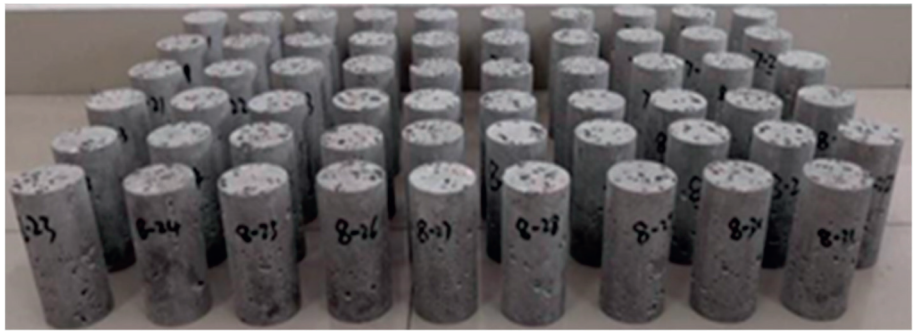

Figure 2: Concrete specimen.

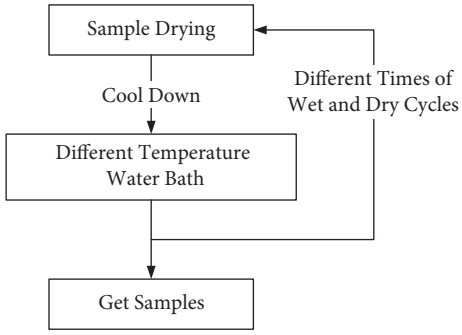

Figure 3: Sample preparation step diagram.

under the primary stress; thus, the axial creep strain becomes larger, and the high stress accelerates the shrink of the crack.

In order to make the change of axial creep strain of thermal insulation shotcrete more specific, the average increment [28] is introduced. The formula of the average increment of thermal insulation shotcrete axial creep strain under adjacent drying and wetting cycles could be expressed as follows:

$$\Delta\varepsilon = \frac{(\varepsilon_n - \varepsilon_m)/\varepsilon_m}{n - m} \times 100\%. \quad (1)$$

In the formula, ε_n and ε_m represent the axial creep strain after doing n times and m times of thermal insulation shotcrete drying and wetting cycles, respectively. When n is 3, 7, 14, and 28, the value of M is 0, 3, 7, and 14.

The average increment table of thermal insulation shotcrete axial creep strain under adjacent drying and wetting cycles (Table 4) is given. It can be found that the average increase of axial creep strain of thermal insulation shotcrete under 0–3 and 3–7 cycles is significantly higher than that under 7–14 and 14–28 cycles. The maximum increase of axial creep strain at 0–3 times is 16.21%, and the minimum value of 8.26% under 0–3 and 3–7 cycles is much higher than the maximum value of the average increase under 7–14 and 14–28 cycles. This indicates that the axial creep strain of thermal insulation shotcrete increases greatly in the early stage of the drying and wetting cycles.

3.1.3. The Effect of the Drying and Wetting Cycles on Axial Steady Creep Rate of Thermal Insulation Shotcrete for Sample. The changing chart of thermal insulation shotcrete axial steady creep rate under different stress levels in different dry and wet cycles is shown in Figure 6. It can be found that the changing trend of thermal insulation shotcrete axial steady-state creep rate under different stress levels is basically the same as the changing of the times of the drying and wetting cycles. It is all increases nonlinearly with the increasing times of the dry and wet cycles, and the axial steady-state creep strain rate value under the higher stress level is much higher. The average increase of thermal insulation shotcrete axial steady-state creep rate under adjacent drying and wetting cycles is given in Table 5. The table provides that the average increase of axial steady-state creep rate under adjacent drying and wetting cycles is quite different, among which the average increase of 0–3 times is the largest, and the maximum value is 92.57%, which is far more than the average increase value of other adjacent cycles. This indicates that the axial steady creep rate of thermal insulation shotcrete increases greatly at 0–3 times of adjacent cycles.

3.1.4. Effect of Dry-Wet Cycles on Instantaneous Deformation Modulus of Samples. The ratio of each step stress to its corresponding instantaneous strain is defined as the instantaneous deformation modulus of thermal insulation shotcrete, E_0. Taking the number of drying and wetting cycles, n as the abscissa and the instantaneous deformation modulus under each cycle number as the ordinate, the scatter distribution diagram of instantaneous deformation modulus under different stress levels after drying and wetting cycles for 0, 3, 7, 14, and 28 times was drawn. After fitting it with the logarithmic function, the fitting results are

Table 2: Axial graded stress.

Loading series	Axial graded stress (MPa)				
	0	3	7	14	28
1	6.926	6.926	6.926	6.926	6.926
2	9.524	9.524	9.524	9.524	9.524
3	12.121	12.121	12.121	12.121	12.121
4	14.719	14.719	14.719	14.719	14.719
5	17.316	17.316	17.316	17.316	17.316

Table 3: Specific test plan.

Times	T (°C)			
	25	40	60	80
3	A11/7-24 A12/7-26 A13/7-4			
7	A21/7-10 A22/8-4 A23/8-2			
14	A31/8-12 A32/8-3 A33/8-29			
28	A41/7-18 A42/8-17 A43/8-26	B41/8-1 B42/8-19 B43/8-20	C41/8-7 C42/8-30 C43/8-24	D41/8-8 D42/8-16 D43/8-5

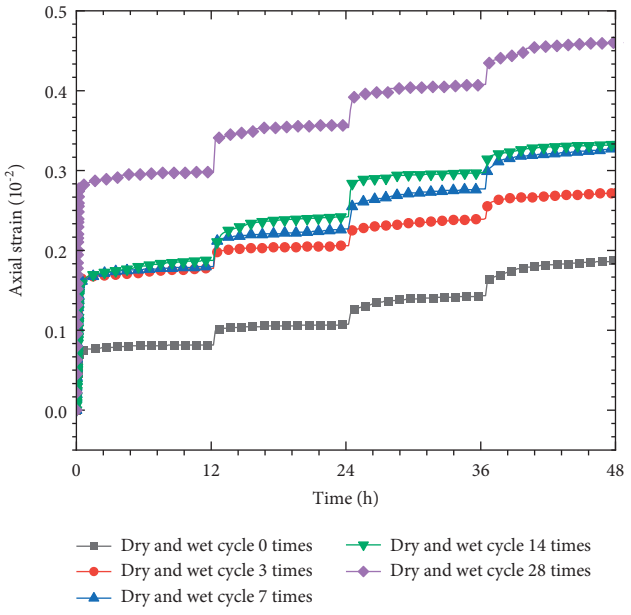

Figure 4: Uniaxial compression creep curve of different dry-wet cycles.

shown in Figure 7. As shown in the figure, the instantaneous deformation modulus of thermal insulation shotcrete decreases nonlinearly with the increasing times of the drying and wetting cycles. What is more, the instantaneous deformation modulus of thermal insulation shotcrete E_0 at different stress levels has the following relationship with the times of drying and wetting cycles, n:

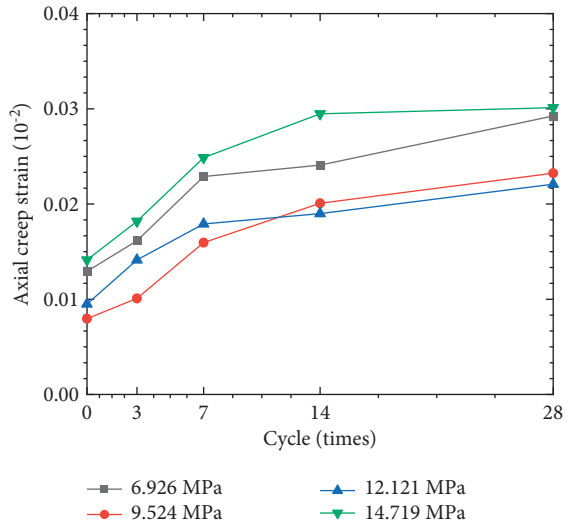

Figure 5: Axial creep strain of thermal insulation shotcrete under different drying and wetting cycles.

$$E_0 = 6.31 - 0.86 \ln n \left(R^2 = 0.95\right). \tag{2}$$

The instantaneous elastic modulus of thermal insulation shotcrete at different stress levels fluctuates in a certain range under the same cycle times. Therefore, the average value of instantaneous elastic modulus under four stress levels was taken as the research object to explore the variation of instantaneous elastic modulus of thermal insulation shotcrete under different wetting and drying cycles. According to the research of Deng [29], define the decreases of degree of the average instantaneous deformation modulus of thermal insulation shotcrete after different drying and wetting cycles as degradation degree and define the average decrease degree of thermal insulation shotcrete average instantaneous deformation modulus as the stage degradation degree Δs. Thus, the relationship of total degradation degree Sn and stage deterioration degree Δs can be expressed as follows:

$$S_n = \frac{\overline{E_{00}} - \overline{E_{0n}}}{\overline{E_{00}}} \times 100\%, \tag{3}$$

$$\Delta S = \frac{S_n - S_m}{n - m}. \tag{4}$$

In the formula, $\overline{E_{00}}$ is the average value of the instantaneous deformation modulus of the sample when the dry-wet cycles is 0 times, and $\overline{E_{0n}}$ is the average value of the

Table 4: Average increment of thermal insulation shotcrete axial creep strain under adjacent drying and wetting cycles.

Stress level (MPa)	Average increment of axial creep strain (%)			
	0–3	3–7	7–14	14–28
6.926	8.26	10.46	0.75	1.53
9.524	8.92	14.52	3.70	1.12
12.121	16.21	6.71	0.87	1.16
14.719	9.61	9.18	2.65	0.15

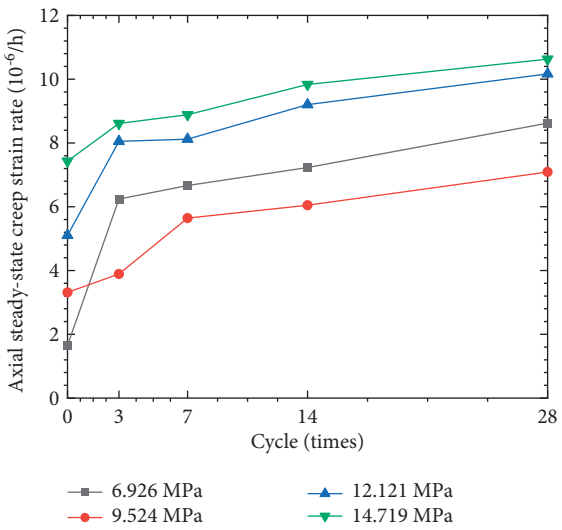

Figure 6: Axial steady creep rate of thermal insulation shotcrete under different drying and wetting cycles.

instantaneous deformation modulus of the sample during N dry-wet cycles. When n is 3, 7, 14, and 28, M is 0, 3, 7, and 14.

According to the calculation results of equations (3) and (4), the total deterioration degree S_n and the stage deterioration degree Δs of thermal insulation shotcrete average instantaneous deformation modulus under different drying and wetting cycles are planted (Figure 8). As shown in Figure 8, with the increasing times of the drying and wetting cycles, the total deterioration degree of average instantaneous deformation modulus gradually increases, and their value are 44.81%, 51.24%, 57.33%, and 65.05% (from small to large). But the stage deterioration degree between 0, 3, 7, 14, and 28 adjacent cycle times decreases in turn, of which the deterioration degree of 0–3 times is the largest, reaching 14.94%, which is far greater than that of other adjacent cycle times. This indicates that the deterioration of thermal insulation shotcrete is gradual processing during the drying and wetting cycles. What is more, during the process of drying and reabsorbing water at the early stage of the cycle, there is a large concentration gradient difference between the surface and the interior of the thermal insulation shotcrete specimen, which makes the deterioration degree obvious relatively.

3.2. Creep Characteristics of Specimens at Different Water Bath Temperatures. When the step stress is 14.719 MPa, the table of the axial steady-state creep rate of thermal insulation shotcrete at different water bath temperatures after experiencing drying and wetting for 28 times can be drawn as follows (Table 6). As it given in the table, the axial steady-state creep rate of thermal insulation shotcrete increases with the increase of water bath temperature, indicating that the drying and wetting cycles at higher water bath temperature will enhance the axial steady-state creep rate of thermal insulation shotcrete.

Table 5: Average increase of thermal insulation shotcrete axial steady creep rate under adjacent drying and wetting cycles times.

Stress level (MPa)	Average increase of axial steady creep rate (%)			
	0–3	3–7	7–14	14–28
6.926	92.57	1.71	1.21	1.38
9.524	5.81	11.26	1.02	1.23
12.121	19.26	0.21	1.91	0.75
14.719	5.30	0.80	1.52	0.58

The logarithmic ln$K$ is taken from the axial steady-state creep rate K of thermal insulation shotcrete under different water bath temperatures, and logarithmic ln$k$ has a linear relationship with the reciprocal $1/T$ of the absolute temperature T, which can be analogically written as Arrhenius formula:

$$K = A_1 \exp\left(-\frac{Q_C}{RT}\right), \tag{5}$$

where K is the axial steady-state creep rate of specimen; A_1 is the material structure coefficient related to stress, and unit is consistent with K; R is the molar gas constant, which is 8.314 J/(mol·K); QC is the creep activation energy, unit: J/mol; T is the absolute temperature, unit: K.

In the formula (5), the creep activation energy represents the energy required for a unit amount of material to creep initially. If the creep activation energy of the material is larger, it means that creep needs more energy; thus, it is difficult to produce creep under the same conditions. Therefore, the creep activation energy can be used to measure the deformation properties of materials.

If the logarithms of both sides of equation (5) are taken at the same time, then

$$\ln K = \ln A_1 - \frac{Q_C}{RT}. \tag{6}$$

Fitting (Figure 9) according to the correlation value of formula (6) is given in Table 7.

The structural coefficient A_1 under the stress of 14.719 MPa was obtained by calculation. The creep activation energy QC obtained by fitting was 3.658 kJ/mol, and the correlation coefficient was 0.9744. As shown in Figure 9, the fitting results are good.

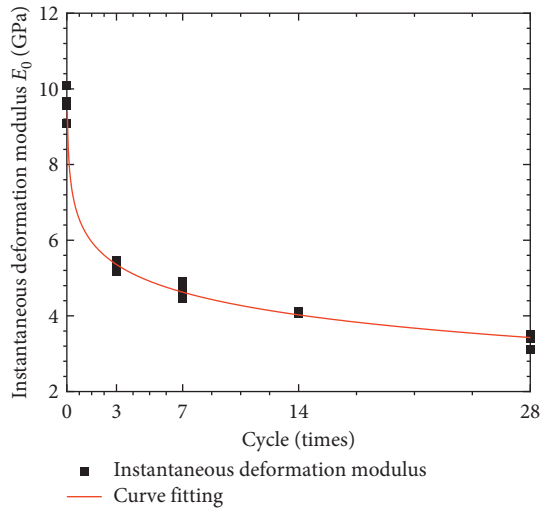

Figure 7: Fitting curves of thermal insulation shotcrete instantaneous deformation modulus under the drying and wetting cycles.

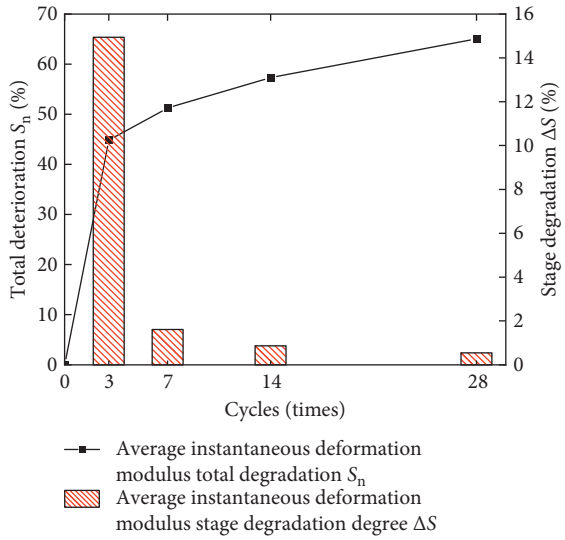

Figure 8: Total degradation degree and stage deterioration degree of average instantaneous deformation modulus under different drying and wetting cycles.

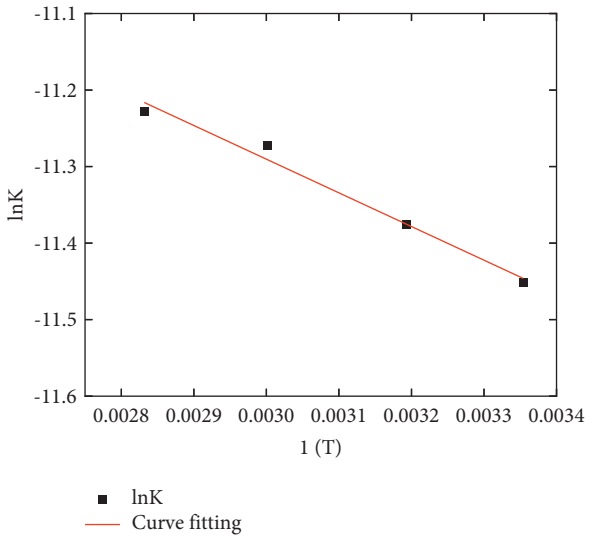

Figure 9: Fitting diagram of creep affected by water bath temperature.

Table 6: Axial steady-state creep rate at different water bath temperatures.

Stress (MPa)	Axial steady creep rate at different water bath temperatures (10^{-6}/h)			
	Normal atmospheric temperature	40°C	60°C	80°C
14.719	10.629	11.472	12.715	13.289

4. Failure Mode

The uniaxial creep failure pattern of specimens under the action of temperature and humidity cycles is shown in Figures 10 and 11. Figure 10 shows the failure pattern of specimens under the different water bath temperatures, and Figure 11 shows the failure pattern of specimens under different cycles times under the same water bath temperature.

Under uniaxial conditions, the fracture of the specimen is mainly based on tensile. As shown in Figure 10, the fracture degree of the specimen decreases gradually. Under the action of low water bath temperature, the fracture of the specimen and the peripheral spalling part is more obvious. The main reason is that the internal matrix of the specimen may change under the action of temperature, and the fracture degree is getting lower and lower due to the closer connection of the matrix. What is more, with the increase of water bath temperature, shear failure appears. It can be seen from Figure 11 that when the water bath temperature is 40°C, the fragmentation degree of the specimen first increases and then decreases with the increasing times of

Table 7: Calculation table of creep fitting equation influenced by water bath temperature.

Stress (MPa)	Temperature (°C)	Reciprocal of absolute temperature (1/K)	Axial steady-state creep rate K (10^{-6}/h)	LnK	Fitting	A_1 (10^{-11}/h)	Q_C (kJ/mol)
	Normal atmospheric temperature	0.003354	10.6294	−11.452			
14.72	40	0.003193	11.4717	−11.376	$y = -439.97x - 9.97$	4.68	3.658
	60	0.003002	12.7148	−11.273			
	80	0.002832	13.2894	−11.229			

(a) (b) (c) (d)

Figure 10: Failure pattern of specimens under the different water bath temperatures (drying and wetting cycles, 3 times). (a) Normal atmospheric temperature. (b) 40°C. (c) 60°C. (d) 80°C.

(a) (b) (c) (d)

Figure 11: Failure pattern of specimens under different cycle times (40°C). (a) Three times. (b) Seven times. (c) 14 times. (d) 28 times.

cycles, among which the specimen with cycling for 3 and 7 times has a greater crushing degree, while the crushing degree of the specimen with cycling for 28 times is small, but some parts of specimen are spalling. It is analyzed that this is caused by the dispersion and condensation of sample components under the action of the drying and wetting cycles.

5. Conclusion

(1) Under normal temperature water bath, the creep deformation and axial creep strain of thermal insulation shotcrete specimens increase with the increasing times of the drying and wetting cycles, the deformation values after cycling for 28 times increase obviously, and the axial creep strain increases greatly at the early stage of cycle times.

(2) The results show that the axial steady creep rate of thermal insulation shotcrete increases nonlinearly with the increase of the drying and wetting cycles under different stress levels, and the value of axial steady creep strain rate is larger at the higher stress level, among which the average increase of 0–3 times is the largest, and the maximum value is 92.57%. The axial steady-state creep rate of thermal insulation shotcrete increases with the increase of water bath temperature after doing the drying and wetting cycles for 28 times, which indicates that the drying and wetting cycles will increase the axial steady-state creep rate of thermal insulation shotcrete under higher water bath temperature.

(3) The results show that the instantaneous deformation modulus of thermal insulation shotcrete decreases logarithmically with the increasing times of the drying and wetting cycles. The total degradation degree of average instantaneous deformation modulus increases gradually, but the stage deterioration degree between adjacent cycles decreases in turn.

(4) The fracture of thermal insulation shotcrete specimen in 3 cycles is mainly based on tensile, and shear failure occurs with the increase of immersion temperature. When the water bath temperature is 40°C, the fragmentation degree of the specimen first increases and then decreases with the increasing times of the cycles.

Data Availability

The data used to support the findings of this study are available from the corresponding author upon request.

Conflicts of Interest

The authors declare that they have no conflicts of interest.

References

[1] B. Shi-Ke, *Study on Utilization of Deep Geothermal Resources in Tang Kou Coal Mine*, China University of Mining and technology, Beijing, China, 2018.

[2] Y. Yu-Biao, *Research on thermal Damage Control Technology of Deep Mine in Zhangshuanglou Coal Mine*, China University of Mining and Technology, Beijing, China, 2012.

[3] J.-R. Zhang and O. Xiao-Qiang, "Research idea for high-performance thermal insulation lightweight aggregate shotcrete in high geo-temperature tunnel," *Concrete*, vol. 323, no. 9, pp. 140–144, 2016.

[4] W.-J. Yao and J.-Y. Pang, "Research and application of new thermal insulation concrete shotcrete support technology," *Journal of Yangtze River Academy of Sciences*, vol. 34, no. 1, pp. 124–128, 2017.

[5] Q.-L. Wang and L. Xiao-Xiang, "Analysis on the relationship between water content and stability of surrounding rock in tertiary water rich silty fine sand layer of Taoshuping tunnel and Humaling tunnel," *Modern Tunnel Technology*, vol. 49, no. 4, pp. 1–5, 2012.

[6] D. Ma, H. Duan, X. Li, Z. Li, Z. Zhou, and T. Li, "Effects of seepage-induced erosion on nonlinear hydraulic properties of broken red sandstones," *Tunnelling and Underground Space Technology*, vol. 91, no. 9, Article ID 102993, 2019.

[7] D. Ma, H. Duan, J. Liu, X. Li, and Z. Zhou, "The role of gangue on the mitigation of mining-induced hazards and environmental pollution: an experimental investigation," *The Science of the Total Environment*, vol. 664, no. 5, pp. 436–448, 2019.

[8] D. Ma, J. Zhang, H. Duan et al., "Reutilization of gangue wastes in underground backfilling mining: o," *Chemosphere*, vol. 264, no. 2, Article ID 128400, 2021.

[9] X.-L. Cao, *Resource Utilization Technology of High Temperature Heat Damage in Deep Mine of Sanhejian Mine*, China University of Mining and Technology, Beijing, China, 2010.

[10] Z. Gao-wen, L. Jing-pei, H.-h. fan et al., "Effect of chloride on sulfate corrosion deterioration and diffusion of cast-in-situ concrete under dry wet cycle," *Journal of Tongji University: Natural Science Edition*, vol. 46, no. 12, pp. 1637–1645, 2018.

[11] L. Bei-xing, Q. Fang, and F. Peng, "Durability of high content admixture concrete semi immersed in sulfate solution," *Journal of Harbin Engineering University*, vol. 41, no. 6, p. 7, 2020.

[12] C. Wei-kang and Q.-f. Liu, "Numerical study on coupled transport of moisture and multi ions in concrete under dry wet alternation," *Journal of Hydraulic Engineering*, vol. 1–11, 2021.

[13] M.-H. Zhang and Y.-Y. sun, "Resistance to Cl- permeability of nano concrete under dry wet cycling," *Journal of Harbin Institute of Technology*, vol. 51, no. 8, pp. 167–176, 2019.

[14] L. Yao, S.-P. Yin, and L. V. Heng-Lin, "Interfacial properties of fiber reinforced concrete and existing concrete under chloride drying and wetting cycles," *Journal of Central South University*, vol. 27, no. 3, pp. 252–266, 2020.

[15] H. Xue-Qiang, S.-L. Zhan, Q. Xu et al., "Effect of dry wet cycling on chloride ion penetration resistance of concrete," *Acta Composite Materials*, vol. 37, no. 1, pp. 198–204, 2020.

[16] L. Jiang and N. Di-Tao, "Study on constitutive relation of concrete under sulfate attack and dry wet cycle," *Journal of China University of Mining and Technology*, vol. 46, no. 1, pp. 66–73, 2017.

[17] K.-f. Chen, Q. Hong-xia, P.-h. Wang et al., "Reliability evaluation of recycled concrete dry wet cycle based on NMR," *Journal of Huazhong University of Science and Technology (Nature Science Edition)*, vol. 48, no. 7, pp. 88–92, 2020.

[18] L. Yue, Z. Guan, P. Geng et al., "Study on deterioration performance of early age concrete under sulfate and dry wet cycle," *Concrete*, vol. 359, no. 9, pp. 6–8, 2019.

[19] J. Shao-fei, E.-j. Cui, J. Wang et al., "Study on interfacial bonding performance of CFRP concrete under chloride dry wet cycle," *Journal of Building Structures*, vol. 1–11, 2021.

[20] L. Qiang, X. Li, K. Yang et al., "The long-term failure mechanisms of alkali-activated slag mortar exposed to wet-dry cycles of sodium sulphate," *Cement and Concrete Composites*, vol. 116, Article ID 103893, 2020.

[21] J.-J. Guo, P.-Q. Liu, C.-L. Wu, and K. Wang, "Effect of dry-wet cycle periods on properties of concrete under sulfate attack," *Applied Sciences*, vol. 11, no. 2, p. 888, 2021.

[22] A. Dehestani, M. Hosseini, and A. Taleb Beydokhti, "Effect of wetting-drying cycles on mode I and mode II fracture toughness of cement mortar and concrete," *Theoretical and Applied Fracture Mechanics*, vol. 106, Article ID 102448, 2020.

[23] L. Da-qing, C. Liang-liang, J.-W. Gong et al., "Study on the relationship between compressive strength and splitting tensile strength of recycled concrete under sulfate dry wet cycle," *Water Resources and Hydropower Technology*, vol. 49, no. 4, pp. 188–194, 2018.

[24] J. Cao, L.-F. Liu, Z. Han et al., "Experimental study on creep of fly ash concrete under dry wet cycling," *Journal of Nanchang Institute of Engineering*, vol. 36, no. 4, 2017.

[25] L. Han-Hu, L. Xiu-Han, Z.-q. Jiang et al., "Influence of underground water temperature on prediction of mine water inflow," *China Coal Geology*, vol. 26, no. 7, pp. 42–44, 2014.

[26] Ministry of Housing and Urban Rural Development of the People's Republic of China, *JGJ/T372-2016, Technical Specification For Application Of Shotcrete*, China Construction Industry Press, Beijing, China, 2016.

[27] Ministry of Construction of the People's Republic of China, *GB/T50081-2002, Test Method Standard for Mechanical Properties of Ordinary concrete*, China Construction Industry Press, Beijing, China, 2003.

[28] Q.-y. Ma, Y. Pei-Yang, and P. U. Yuan, "Experimental study on the influence of dry wet cycle on creep characteristics of deep siltstone," *Journal of Rock Mechanics and Engineering*, vol. 37, no. 3, pp. 593–600, 2018.

[29] H.-F. Deng, Z.-Y. Xiao, L. Jian-Lin et al., "Experimental study on strength degradation of damaged sandstone under water rock interaction," *Journal of Rock Mechanics and Engineering*, vol. 34, no. S1, pp. 2690–2698, 2015.

Hindawi
Advances in Civil Engineering
Volume 2021, Article ID 3750589, 16 pages
https://doi.org/10.1155/2021/3750589

Research Article

Simulation of Motion Behavior of Concrete in Pump Pipe by DEM

Ji Hao[1,2] **Caiyun Jin**[3] **Yue Li**[1] **Zigeng Wang**[1] **Jianglin Liu**[1] **and Hongwen Li**[1]

[1]*The Key Laboratory of Urban Security and Disaster Engineering, Beijing University of Technology, Beijing 100124, China*
[2]*Department of Material Science and Engineering, Beijing University of Technology, Beijing 100124, China*
[3]*College of Applied Sciences, Beijing University of Technology, Beijing 100124, China*

Correspondence should be addressed to Caiyun Jin; jincaiyun@bjut.edu.cn

Received 14 April 2021; Accepted 13 May 2021; Published 26 May 2021

Academic Editor: Guoming Liu

In this paper, the mesocalibration test was used to measure the contact parameters (restitution coefficient, rolling friction coefficient, static friction coefficient, and surface energy) between coarse aggregate particles and mortar particles in Discrete Element Method (DEM) model of concrete. Then, the DEM model of concrete slump was established according to the coarse aggregate gradation to study the flow behavior of coarse aggregate in fresh concrete. The slump test result was compared with the output of the slump DEM model with high consistent, indicating the promising reliability of the mesocalibration test. Finally, based on the mesocalibration test results, the DEM model of pumping concrete was established. It was obtained that the pumping pressure calculated by the numerical model was similar to that of the pumping test with satisfactory accuracy better than the concrete pumping pressure calculated according to the rheological test results of concrete and lubricating layer. On this basis, the movement trajectory of coarse aggregate in the pump pipe was analyzed and the influence of coarse aggregate on the pumping performance of concrete was revealed.

1. Introduction

Fresh concrete is a kind of heterogeneous and multiphase composite material with highly inhomogeneous composition and structure [1, 2]. In fresh concrete, mortar showed non-Newtonian flow behavior, while coarse aggregate showed discrete particle flow behavior [3]. The movement behavior of coarse aggregate in concrete was an important factor affecting the fluidity and pumpability [4, 5]. In the concrete flow process, there are very complex interactions between the components [6]. Accurate understanding of the flow behavior of fresh concrete is a necessary prerequisite for normal construction and improvement of hardening properties of concrete [7]. In order to deeply study the flow performance of fresh concrete, numerical simulation had become a common method to study the fluidity of concrete [8]. DEM was a numerical method to simulate the motion behavior of discontinuous media with unique advantages in describing the fluidity of concrete on macroscale and the collision behavior of aggregate particles on mesoscale [9, 10]. During the pumping process, the movement trajectory and collision behavior of the aggregate were the main factors affecting the pumpability of the concrete [11]. The DEM can be used to truly simulate the flow behavior of the aggregate in the pump pipe [12].

At present, a variety of DEM contact models of fresh concrete have been proposed to simulate the fluidity of fresh concrete. Mechtcherine [13] focused on the algorithm of model parameters related to yield stress and then compared the analytical prediction and numerical prediction of the slump-flow test. Shyshko [14] based on the test results of force-displacement between particles to establish a normal contact model between particles, and the influence of contact parameters on numerical simulation was studied. Remond and Pizette [15] proposed a new "hard-core soft-shell" DEM model to simulate the rheology and slump of concrete. Hoornahad and Koenders [16] used two-phase paste-bridge system as grain-paste-grain interactions to explore the fluidity of fresh concrete. Li et al. [17, 18] proposed a DEM model for predicting the time-dependent fluidity of fresh concrete. Zhang et al. [19] established the normal action constitutive relationship between self-

compacting concrete particles and then simulated the flow process of rock-filled concrete. Compared with the concrete fluidity test, the DEM simulation can describe the flow behavior of concrete particles at the mesoscopic level. Considering the important factors such as pipeline, aggregate, and pumping conditions, Zhan et al. [20] adopted the DEM to simulate the local pumping of concrete. Tan [21] established the DEM model of concrete by considering the thixotropy of fresh concrete and studied the variation of lateral pressure of concrete to wall with time. Cui et al. [22, 23] used irregularly shaped particles as coarse aggregate to study the effect of coarse aggregate size distribution on pump plugging. Cao et al. [24] studied the effect of coarse aggregate volume fraction on yield stress by using the DEM model of fresh concrete, and then they clarified the effect of coarse aggregate volume fraction on pumping pressure and wall wear. Haustein et al. [25] used DEM to study the segregation of concrete particles under pulsating pumping regime.

A variety of DEM contact models suitable for fresh concrete have been proposed, and extensive fluidity simulations have been carried out. However, the fundamental task of DEM simulating fresh concrete has not been solved, that is, the determination of the quantitative relationship between the contact parameters in the concrete DEM model and the properties and proportion of the components in the concrete [26, 27]. At present, there were two methods to calibrate the contact parameters of DEM [26]. The first method was trial-error, that is, iteratively change the DEM parameter values until the numerical simulation results match the test results to determine the contact parameter values of the DEM model [28, 29]. However, the simulation results were affected by multiple parameter values, and different parameter combinations may produce the same simulation results [28, 30]. Therefore, the main problem of trial and error method was that the correctness of parameter combination used in numerical simulation was hard to estimate [31, 32]. The second method was to measure the mesocontact parameters directly by test (mesocalibration test), then establish DEM model, and compare the simulation results with the test results [33]. The measured results of the mesocalibration test were close to the real contact parameter value [34]. However, due to the great difference in the shape and size of concrete particles, the testing method of contact parameters was still being further improved [16].

This paper established a quantitative relationship between the DEM contact parameters and the properties and proportions of the fresh concrete composition by using the method of mesocalibration test and further studies the flow behavior of concrete particles in the pump pipe. Fresh concrete was regarded as a material composed of discrete coarse aggregates and uniform flowing mortar. This DEM modeling method was called separate single phase element mode [16]. Through a series of mesocalibration tests, the contact parameters of coarse aggregate particles and mortar particles in concrete DEM model were measured, including restitution coefficient, static friction coefficient, rolling friction coefficient, and surface energy. Then the slump DEM model of fresh concrete was established according to the particle size distribution of coarse aggregate with the contact parameters being inputted for slump numerical simulation. The DEM simulation results were compared with the test results to verify the feasibility of using calibration test to measure the contact parameters between fresh concrete particles. Finally, the DEM model of pumping concrete was established, and the simulation results were compared with the pumping test results to analyze the movement behavior of coarse aggregate in the pumping process of concrete. The research roadmap of this paper is shown in Figure 1.

2. Materials and Test

2.1. Materials

2.1.1. Cementitious Materials. In this paper, P II 42.5 Portland cement, F-type fly ash, S95 ultrafine slag powder, and ultrafine silica fume were used as cementitious materials. For the chemical composition and basic properties of cementitious materials, see Table 1.

2.1.2. Aggregate. In order to avoid the influence of the shape of aggregate on the accuracy of particle mesoinput parameters, high-precision spherical glass was used as the coarse aggregate of concrete to carry out mesocalibration test, slump test, rheological test, and pumping test, as shown in Figure 2(a). The glass sphere had smooth surface, good wear resistance, and high compressive strength. The particle size error of glass sphere was less than 0.02 mm, the density was 2530 kg/m^3, the shear modulus was 1.97 GPa, and Poisson's ratio was 0.25. The particle size distribution of coarse aggregate is shown in Table 2.

This paper used spherical glass beads as fine aggregates, as shown in Figure 2(b). The density of the glass beads was 2487 kg/m^3, the shear modulus was 1.93 GPa, and Poisson's ratio was 0.26. The particle size distribution of the fine aggregate is shown in Table 3.

2.1.3. Mixture Proportion. The mix ratio of concrete can be divided into three groups, A, B, and C, according to the amount of cementitious material and water consumption, and each group had three different coarse aggregate contents. Nine concrete mixes for slump test, rheological test, pumping test, and DEM parameter calibration test are shown in Table 4. In this paper, glass sphere of different particle sizes was used to replace sand and gravel with equal volume. The polycarboxylic acid superplasticizer with a water reduction rate of 29% and a solid content of 16.9% was used.

2.2. Concrete Fluidity Test

2.2.1. Slump Test. The slump test of concrete was carried out according to the standard GB/T 50080-2016 [35]. The lift-off speed of the slump cone was 0.06 m/s. The slump and slump-flow test results of fresh concrete are shown in Table 5. Comparing the slump and slump-flow test results of A, B,

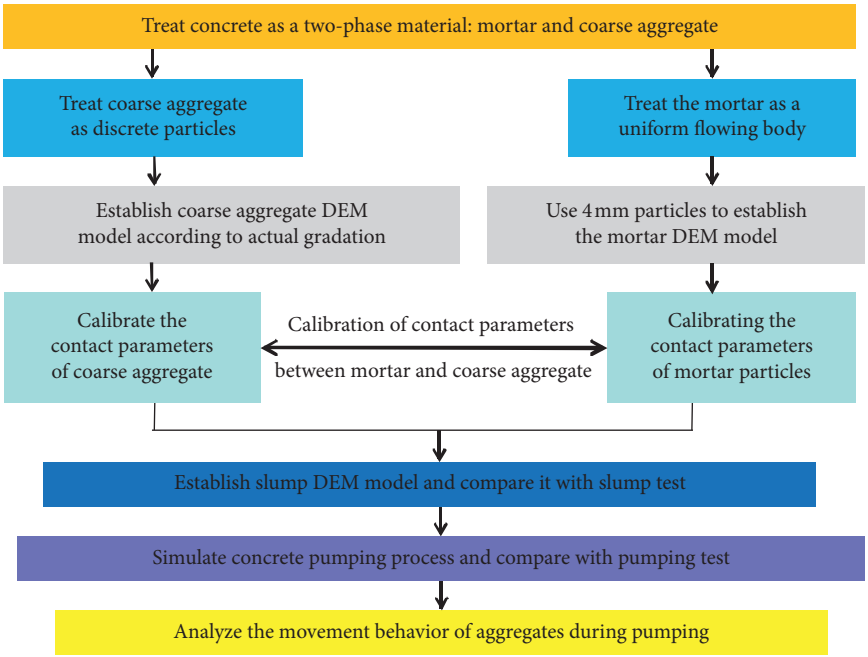

Figure 1: Roadmap of this paper.

Table 1: Chemical compositions and basic properties of cementitious materials (%).

Chemical composition	Cement	Fly ash	Ultrafine slag	Silica fume
SiO_2	23.6	52.3	45.7	92.7
Al_2O_3	4.4	29.7	5.8	1.1
Fe_2O_3	2.3	6.5	0.3	0.7
CaO	67.5	11.2	46.6	0.8
SO_3	2.03	1.5	1.2	0.0
Ignition loss	4.08	3.7	0.26	4.0
Density g/cm^3	3.10	2.78	2.81	2.20

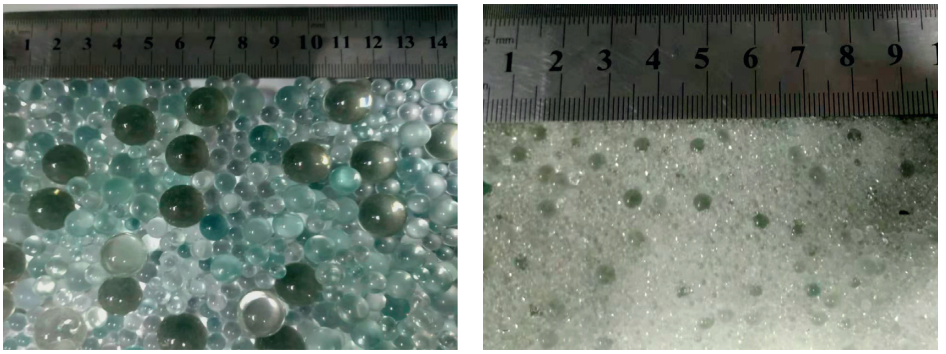

(a) (b)

Figure 2: Spherical glass aggregate. (a) Coarse aggregate. (b) Fine aggregate.

Table 2: Size distribution of coarse aggregate (%).

Particle size	6 mm	7 mm	8 mm	9 mm	10 mm	11 mm	12 mm	13 mm	14 mm	16 mm
Volume percent	8	10	10	12	12	11	10	9	8	10

Table 3: Size distribution of fine aggregate (%).

Particle size	0.15 mm	0.30 mm	0.60 mm	1.18 mm	2 mm	3 mm	4 mm
Volume percent	8	22	20	12	13	13	12

Table 4: Mixture proportions of concrete (kg/m^3).

Code	*w/c*	Sand rate	Water	Cement	Fly ash	Slag	Silica fume	Fine aggregate	Coarse aggregate	Admixture
A1	0.42	0.41	189.0	250	120	60	20	950	1367	2.6
A2		0.46	189.0	250	120	60	20	950	1115	2.6
A3		0.51	189.0	250	120	60	20	950	910	2.6
B1	0.32	0.41	193.6	320	150	100	35	780	1122	3.9
B2		0.44	193.6	320	150	100	35	780	993	3.9
B3		0.47	193.6	320	150	100	35	780	890	3.9
C1	0.26	0.37	163.8	350	130	100	50	647.5	1102	5.6
C2		0.40	163.8	350	130	100	50	647.5	971	5.6
C3		0.43	163.8	350	130	100	50	647.5	858	5.6

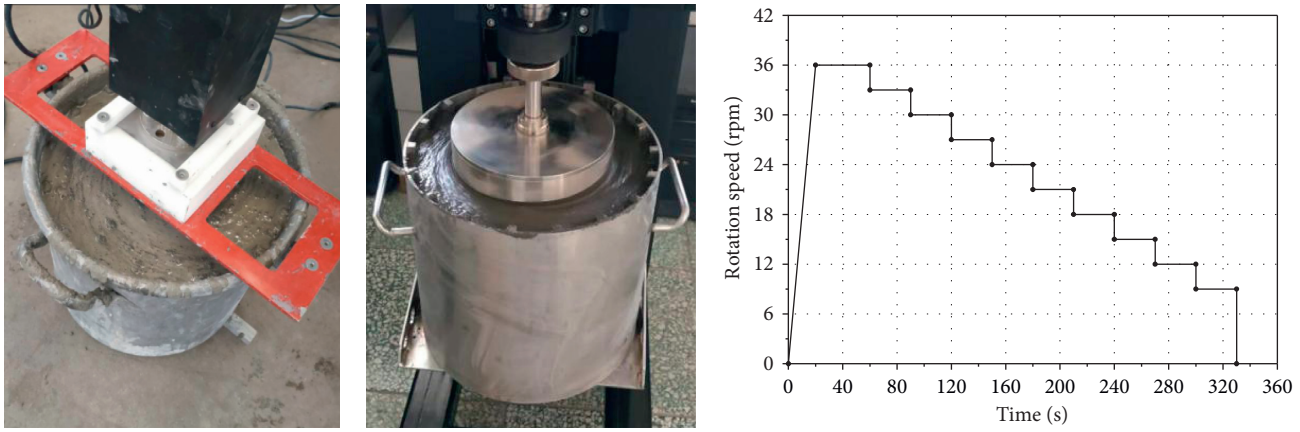

(a) (b) (c)

Figure 3: Tribometer and rheometer used to measure rheological properties. (a) ICAR rheometer. (b) TR-CRI tribometer. (c) Test speed of TR-CRI.

Table 5: Test results of slump and slump-flow of fresh concrete (mm).

	A1	A2	A3	B1	B2	B3	C1	C2	C3
Slump	222	224	226	219	221	224	212	215	217
Slump-flow	555	561	565	549	551	552	512	516	522

Table 6: Rheological parameters of lubricating layer and bulk concrete.

Parameter	A1	A2	A3	B1	B2	B3	C1	C2	C3
τ_0 (Pa)	21.4	20.2	19.4	28.0	26.3	25.7	37.8	35.8	33.1
μ (Pa·s)	16.0	15.2	14.1	20.1	19.5	18.3	24.6	22.3	21.4
τ_{0LL} (Pa)	10.8	10.4	10.1	12.2	11.9	11.5	14.5	13.7	13.3
μ_{LL} (Pa·s)	1.8	1.7	1.7	2.2	2.2	2.1	3.6	3.6	3.6

and C of concrete, the influence of glass sphere coarse aggregate content on concrete test result was small, and the flow performance of concrete with the same amount of cementitious material and water consumption was basically similar.

2.2.2. Rheological Test of Concrete and Lubricating Layer. At present, it was generally believed that the rheological properties of concrete and lubricating layer were the key parameters affecting the pumping pressure of concrete, and there was a good correlation between the pressure loss-flow rate of pumped concrete and the rheological parameters of the concrete [5]. It was very difficult to measure the rheological properties of the lubricating layer in the pump pipe directly. Therefore, it was usually made to use "tribometer" to measure the rheological properties of the lubricating layer [36]. In this paper, the yield stress τ_0 and plastic viscosity μ of concrete were measured by ICAR concrete rheometer (see Figure 3(a)). The yield stress τ_{0LL} and plastic viscosity μ_{LL} of the lubricating layer between concrete and cylinder wall were measured by TR-CRI tribometer (see Figure 3(b)). The test speed of TR-CRI tribometer is shown in Figure 3(c). Rheological parameters of lubricating layer and bulk concrete are shown in Table 6. The content of coarse aggregate had little effect on the rheological properties of concrete. The yield stress and plastic viscosity of concrete with the same water-cement ratio decreased with the decrease of aggregate

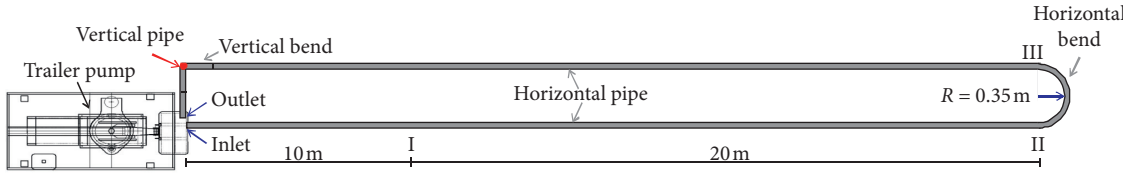

Figure 4: Schematic ground plan of the pumping test.

Table 7: The pumping pressure of concrete in horizontal pipe (MPa/m).

		A1	A2	A3	B1	B2	B3	C1	C2	C3
Simulation value	0.53 m/s	0.0293	0.0286	0.0278	0.0403	0.0396	0.0389	0.0531	0.0526	0.0514
	0.71 m/s	0.0340	0.0332	0.0326	0.0472	0.0460	0.0448	0.0586	0.0569	0.0553
Test value	0.53 m/s	0.0312	0.0307	0.0301	0.0419	0.0409	0.0403	0.0553	0.0543	0.0537
	0.71 m/s	0.0367	0.0356	0.0345	0.0491	0.0475	0.0459	0.0612	0.0606	0.0597
Calculated value	0.53 m/s	0.0718	0.0679	0.0678	0.0878	0.0877	0.0838	0.14339	0.14335	0.14333
	0.71 m/s	0.0956	0.0903	0.0903	0.1169	0.1169	0.1115	0.19100	0.19096	0.19094

content. The yield stress and plastic viscosity of the lubricating layer were very little affected by the coarse aggregate content.

2.2.3. Pumping Test. In this paper, a small-scale pumping test was used to measure the pumping pressure of concrete. The pumping test used HBT6006A-5 trailer pump to provide pumping power, and the maximum pump pressure was 7 MPa. The pump pipe system consisted of a horizontal straight pipe with a length of 59.65 m, a 180° horizontal curved pipe with a bending radius of 0.35 m, a 90° vertical curved pipe with a bending radius of 0.35 m (used to connect the horizontal pipe and the vertical pipe), and a vertical pipe with a height of 3 m. A 180° elbow was used at the end of the vertical pipe to connect to the inlet of the trailer pump so that the concrete can be pumped circularly. The layout plan of the pump pipe is depicted in Figure 4. The inner diameter of the pump pipe was 100 mm, and I, II, and III represented the location of the pressure sensors. The average horizontal pushing speed of the piston was 0.53 m/s and 0.71 m/s, and the corresponding concrete pumping flow was 15 m^3/h and 20 m^3/h. According to the pump pressure difference measured by the pressure sensor, the pump pressure loss (MPa/m) of the horizontal pipe was calculated, as shown in Table 7.

2.3. Calibration Test. The contact model between concrete particles used the Hertz–Mindlin with JKR (Johnson–Kendall–Roberts) Cohesion model [37]. In the concrete separate single phase element mode, fine aggregate accounted for a large proportion in concrete, which was crucial to the flow and other characteristics of concrete. However, due to the large size distribution of fine aggregate, the pursuit of real particle size distribution of fine aggregate was not of great significance to the study of concrete fluidity and led to excessive consumption of calculation time [38, 39]. In order to ensure the efficiency of calculation, uniform sphere can be used instead of fine aggregate in DEM model [23, 40]. Gu et al. [41] proposed that the ratio of sample size to average particle size should be greater than 11.5 to avoid possible scale effects. Therefore, the coarse aggregate elements in the DEM model of concrete in this paper used the same particle size distribution as the test, and the mortar elements were represented by spheres of uniform size. In this paper, the DEM model of mortar was composed of particles with a diameter of 4 mm [31].

The DEM model of concrete included two phases: mortar particle and coarse aggregate particle [16]. In the concrete fluidity test and pumping test, the test equipment material (geometry phase) as the constraining boundary contacted with the mortar particle and coarse aggregate particle. Therefore, in the DEM model, the contact parameters between geometry and mortar particle (MP) and between geometry and coarse aggregate particle (CAP) must be considered. In separate single-phase element mode, there were five groups of contact parameters that needed to be calibrated, including MP-MP, MP-CAP, MP-geometry, CAP-CAP, and CAP-geometry. In the mesocalibration test of mortar particles, the fine aggregate particles of 4 mm were used as the research object to calibrate the contact parameters of MP-MP, MP-CAP, and MP-geometry. The test equipment material used for fluidity test and calibration test in this paper was stainless steel with a density of 7750 kg/m^3, shear modulus of 72.797 GPa, and Poisson's ratio of 0.305.

2.3.1. Coefficient of Restitution. In this paper, MP-geometry restitution coefficient (e_{mg}) was measured with reference to Barrios' test [42]; see Figure 5. MP fell freely from a fixed height H and rebounded to the height of h after colliding with the geometry plate [43]. H and h values were recorded with the high-speed camera. e_{mg} can be calculated using

$$e_{mg} = \sqrt{\frac{h}{H}}. \quad (1)$$

In the e_{mg} test, the free fall particles were 4 mm glass spheres wrapped in paste. In the CAP-geometry restitution coefficient (e_{cg}) test, the free-falling particles were 12 mm glass spheres wrapped in paste. The geometry plate used in

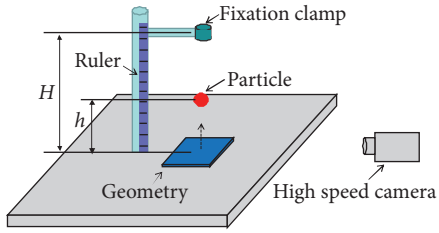

Figure 5: Test device for restitution coefficient.

the test was a stainless steel plate of the same material as the slump plate.

In this paper, the MP-MP restitution coefficient (e_{mm}) test and MP-CAP restitution coefficient (e_{mc}) test were carried out by using the glass plate with the same material and process as the fine aggregate instead of the impacted particles; that is, the geometry plate in Figure 5 was replaced by the glass plate with the same material as the fine aggregate [44]. The CAP-CAP restitution coefficient (e_{cc}) test was carried out using glass plates of the same material as the coarse aggregate instead of the impacted particles. The particles were released from four different fixed heights of 100 mm, 90 mm, 80 mm, and 70 mm and collided with the plate after free fall. The test was repeated 10 times for each fixed height to obtain the average rebound height h.

2.3.2. Coefficient of Rolling Friction. The rolling friction coefficient of concrete particle was measured by inclined test [43], as shown in Figure 6. In the CAP-geometry rolling friction coefficient ($\mu_{r\text{-}cg}$) test and MP-geometry rolling friction coefficient ($\mu_{r\text{-}mg}$) test, the same stainless steel plate as the slump plate was used as the inclined plate [44]. In the CAP-CAP rolling friction coefficient ($\mu_{r\text{-}cc}$) test, the glass plate of the same material as the coarse aggregate was used as the inclined plate. In the MP-MP rolling friction coefficient ($\mu_{r\text{-}mm}$) test and MP-CAP rolling friction coefficient ($\mu_{r\text{-}mc}$) test, the glass plate of the same material as the fine aggregate was used as the inclined plate. In the test of measuring the rolling friction coefficient, the mortar particles were tested with glass spheres with particle size of 4 mm, and the coarse aggregate particles were tested with glass spheres with particle sizes of 16 mm, 14 mm, 12 mm, and 10 mm.

We slowly increased the tilt angle of the inclined plate and recorded the critical rolling friction angle of the particles. The force of the particle on the geometry plate is shown in Figure 7. The value of $\mu_{r\text{-}cg}$ is equal to the tangent of the inclination angle ($\theta_{r\text{-}cg}$) of the plate [44]:

$$\mu_{r-cg} = \tan\theta_{rc-cg}. \quad (2)$$

The test procedures of $\mu_{r\text{-}cg}$, $\mu_{r\text{-}mc}$, $\mu_{r\text{-}cc}$, $\mu_{r\text{-}mg}$, and $\mu_{r\text{-}mm}$ tests were the same, and the test for each particle size was repeated 10 times to obtain the average critical rolling angle.

2.3.3. Coefficient of Static Friction. The static friction coefficient of concrete particle was measured by inclined test [43], same as rolling friction coefficient test. Bonding three glass aggregates of the same particle size together can prevent the aggregate from rolling before sliding on the inclined plate [45], as shown in Figure 8. In the tests of CAP-geometry static friction coefficient ($\mu_{s\text{-}cg}$) and MP-geometry static friction coefficient ($\mu_{s\text{-}mg}$), the same stainless steel plate as the slump plate was used as the inclined plate [44]. In the CAP-CAP static friction coefficient ($\mu_{s\text{-}cc}$) test, the glass plate of the same material as the CAP was treated as the inclined plate. In the MP-MP static friction coefficient ($\mu_{s\text{-}mm}$) and MP-CAP static friction coefficient ($\mu_{s\text{-}mc}$) tests, the glass plate of the same material as the MP was regarded as the inclined plate. The static friction coefficient of particles can be calculated according to the critical sliding angle ($\theta_{s\text{-}cg}$) [44]:

$$\mu_{s-cg} = \tan\theta_{sc-cg}. \quad (3)$$

In the test of measuring the static friction coefficient, the MP were tested with 4 mm particles, and the CAP were tested with 16 mm, 14 mm, 12 mm, and 10 mm particles. The glass aggregate directly extracted from concrete (wrapped with paste) was used as sliding particles to carry out static friction coefficient test. The test procedures of $\mu_{s\text{-}cg}$, $\mu_{s\text{-}mc}$, $\mu_{s\text{-}cc}$, $\mu_{s\text{-}mg}$, and $\mu_{s\text{-}mm}$ were the same. Each particle size test was repeated 10 times to obtain the average critical sliding angle.

2.3.4. Surface Energy. The cohesion between fresh concrete particles was expressed by surface energy (γ) [33]. In this paper, the cohesion force ($F_{pullout}$) between fresh concrete particles was determined by inclined test; see Figure 9. For the calculation process, see [43].

The paste on the surface of MP was the same as that on the surface of CAP, so it can be considered that the surface energy of MP was equal to that of CAP [46, 47]. In the test of measuring surface energy, the coarse aggregate of 16 mm, 14 mm, 12 mm, and 10 mm was used for surface energy test. The surface energy test of each particle size was repeated 10 times to obtain the average value of the critical rolling angle (θ_{rc}).

3. Simulation of Pumping Concrete

3.1. DEM Contact Model. In this paper, Hertz–Mindlin with JKR Cohesion [37] was used as the contact model of concrete particles. Hertz–Mindlin with JKR cohesion took into account the influence of cohesion in the contact zone of particles, which was suitable for the DEM simulation of wet particles. The JKR model modified the normal force on the basis of the Hertz–Mindlin (no slip) model. The tangential forces of JKR model and Hertz–Mindlin (no slip) model were the same.

Figure 10 is the relationship between the normal force and the overlap between particles in the Hertz–Mindlin model and the JKR model. The negative overlap represented the separation between the two particles. When $\gamma = 0$, the normal force of JKR was equal to that of Hertz–Mindlin (no slip) model.

3.2. The Volume of Coarse Aggregate and Mortar. Concrete was regarded as a discontinuous system, consisting of two independent phases, that is, the coarse aggregate of

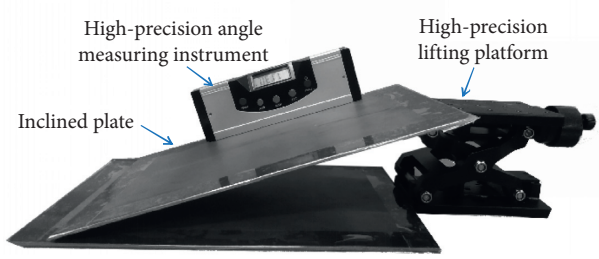

Figure 6: Inclined test device.

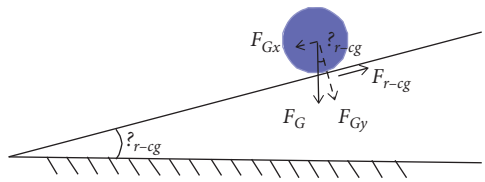

Figure 7: Balance of force in rolling friction test.

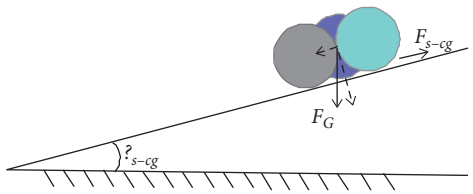

Figure 8: Balance of force in static friction test.

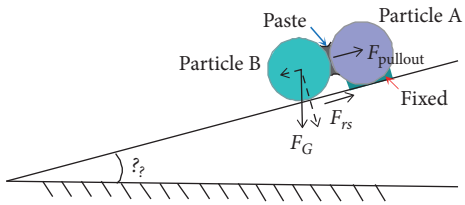

Figure 9: Balance of force in $F_{pullout}$ test.

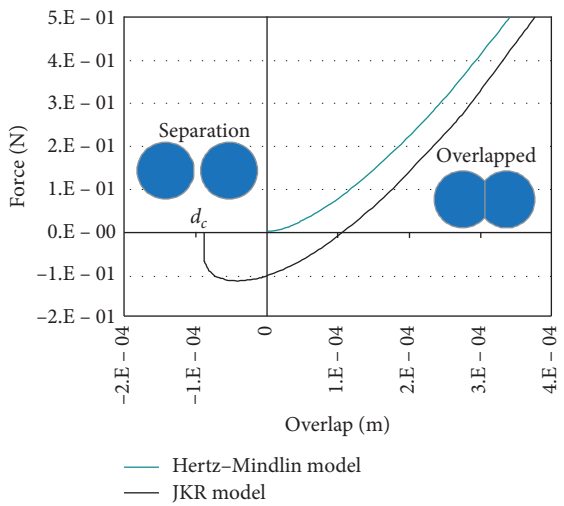

Figure 10: The relationship between normal force and overlap in JKR model.

solid phase and the mortar of liquid phase (see Figure 11(a)) [49]. In fresh concrete, the paste wrapped around the aggregate moved with the aggregate, so the paste around the aggregate needed to be taken into account when calculating the volume fraction of coarse aggregate particles in the DEM model [19]. In this paper, the Excess Paste Theory was used to calculate the volume fraction of coarse aggregate and mortar in the DEM model of fresh concrete. The relative measured value of aggregate packing density in concrete was expressed by coefficient ζ:

$$\zeta = \frac{V_a}{V_b} \leq 1, \tag{4}$$

where V_a is specific aggregate volume; V_b is bulk aggregate volume and represents the volume of aggregate (see Figure 11(b)) in the compacted state. The volume of aggregate in compacted state can be calculated according to ASTM C 29 [50].

In the Excess Paste Theory, the volume of paste V_p was divided into two parts: void paste V_{pv} and excess paste V_{pex}. When the aggregate was in a compacted state, the void paste was considered to fill in the gap between the aggregates (see Figure 11(b)). The excess paste was the remaining paste part, that is, a layer of paste (δ_{pex}) wrapped around each aggregate particle. The volume fraction (V_{pv}) of void paste can be calculated by

$$V_{pv} = \left(\frac{1}{\zeta} - 1\right) \cdot V_a. \tag{5}$$

V_{pv} was subtracted from V_p to calculate V_{pex}:

$$V_{\text{pex}} = V_p - V_{pv}. \tag{6}$$

The aggregate used in this paper was spherical aggregate. Specific aggregate volume (V_a) and excess paste (V_{pex}) were calculated by

$$V_a = \frac{4\pi}{3} \sum N_i R_i^3, \tag{7}$$

$$V_{\text{pex}} = \frac{4\pi}{3} \sum N_i \left(\left(R_i + \delta_{\text{pex}}\right)^3 - R_i^3\right), \tag{8}$$

where R_i is the radius of aggregate and N_i is the number of aggregates in part i.

After determining the aggregate particle gradation, the Klein method can be used to calculate the thickness of the remaining paste layer (δ_{pex}) [51]. The δ_{pex} was proportional to the radius R_i of aggregate, calculated according to (9). In this equation, φ_{pex} was a constant, calculated by (10). It should be ensured that the minimum diameter of aggregate was greater than the minimum value of δ_{pex}, so as to provide a more accurate range for δ_{pex} [48].

$$\delta_{\text{pex}} = R_i \cdot \left(1 + \varphi_{\text{pex}}\right) - R_i, \tag{9}$$

$$\varphi_{\text{pex}} = 1 - \sqrt[3]{1 - \frac{V_p}{V_a}}. \tag{10}$$

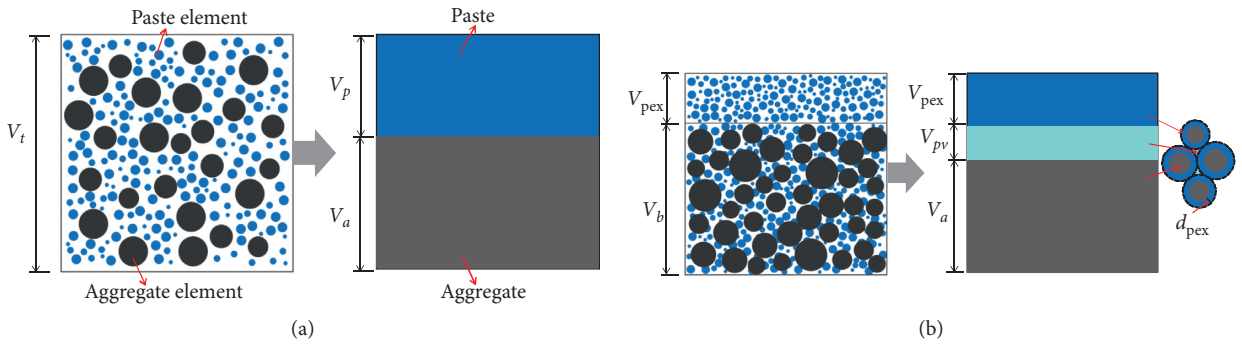

FIGURE 11: Schematic of Excess Paste Theory: (a) the real system; (b) the volume of each part of the system in a compacted state and excess paste thickness [48].

In the DEM model of fresh concrete, the volume of coarse aggregate (V_c) and the volume of mortar (V_m) were calculated by

$$V_c = V_a + V_{\text{pex}}, \tag{11}$$

$$V_m = V_t - V_c, \tag{12}$$

where V_t is the total volume of concrete.

3.3. Results of Calibration Test

3.3.1. The Test Results of Restitution Coefficient. The restitution coefficient test results of B1 concrete are shown in Figure 12(a). The rebound height h decreased with the decrease of fixed height H. The restitution coefficient was calculated according to (1), and the values of restitution coefficient measured at different fixed heights were basically the same. The average restitution coefficients of nine kinds of concrete particles were calculated according to the fixed height H and rebound height h measured by the test, as displayed in Figure 12(b). The coefficient of restitution of concrete particles increased with the increase of water-binder ratio, the restitution coefficient of group A>the restitution coefficient of group B>the restitution coefficient of group C. The recovery coefficient was less affected by coarse aggregate content, and the restitution coefficient of concrete with different coarse aggregate content was basically the same.

3.3.2. The Test Result of Rolling Friction Coefficient. According to the critical rolling angle (θ_{rc}) measured by the inclining test, the rolling friction coefficient of B1 concrete was calculated, as shown in Figure 13(a). The average value of $\mu_{r\text{-}cg}$ of B1 concrete was 0.083, the average value of $\mu_{r\text{-}mc}$ was 0.063, the average value of $\mu_{r\text{-}cc}$ was 0.062, the average value of $\mu_{r\text{-}mg}$ was 0.086, and the average value of $\mu_{r\text{-}mm}$ was 0.084. The average rolling friction coefficients of nine kinds of concrete particles are displayed in Figure 13(b). The rolling friction coefficient of concrete particles increased with the decrease of water-binder ratio, the rolling friction coefficient of group A<the rolling friction coefficient of group B<the rolling friction coefficient of group C. The rolling friction coefficient was less affected by the coarse aggregate content.

3.3.3. The Test Result of Static Friction Coefficient. The static friction coefficient test results of B1 concrete are shown in Figure 14(a). The average values of $\mu_{s\text{-}cg}$, $\mu_{s\text{-}mc}$, $\mu_{s\text{-}cc}$, $\mu_{s\text{-}mg}$, and $\mu_{s\text{-}mm}$ were 0.178, 0.163, 0.162, 0.181, and 0.182, respectively. Figure 14(b) exhibits the average static friction coefficient of nine kinds of concrete. The effect of water-binder ratio on the static friction coefficient of concrete particles was similar to that of the rolling friction coefficient. The static friction coefficient of group A<the static friction coefficient of group B<the static friction coefficient of group C. The content of coarse aggregate had little effect on the static friction coefficient of concrete particles, and the static friction coefficient of concrete with different coarse aggregate content was basically the same.

3.3.4. The Test Result of Surface Energy. The test results of critical rolling angle (θ_{yc}) of B1 concrete are shown in Figure 15. According to the test results of the inclined test in Figure 9, the average surface energy (γ) of 9 kinds of concrete was calculated by the method in [43]. The surface energy (γ) of A1, A2, A3, B1, B2, B3, C1, C2, and C3 is 0.368 J/m^2, 0.368 J/m^2, 0.369 J/m^2, 0.374 J/m^2, 0.374 J/m^2, 0.373 J/m^2, 0.383 J/m^2, 0.384 J/m^2, and 0.383 J/m^2, respectively.

3.4. Establishment of the DEM Model of Pumping Concrete

3.4.1. DEM Model of Slump Test. The slump DEM model was established in accordance with the actual size of the slump cone, and then the density, shear modulus, and Poisson's ratio of the test equipment materials were input. This paper used EDEM software to establish a concrete separate single-phase element mode [16], which regarded concrete as being composed of coarse aggregate wrapped by paste and fine aggregate wrapped by paste. The particle size gradation of CAP was generated in accordance with Table 2. The MP was represented by using 4 mm particles. Then the test results of restitution coefficient, rolling friction coefficient, static friction coefficient, and surface energy in Section 3.3 were inputted into the concrete DEM model as the

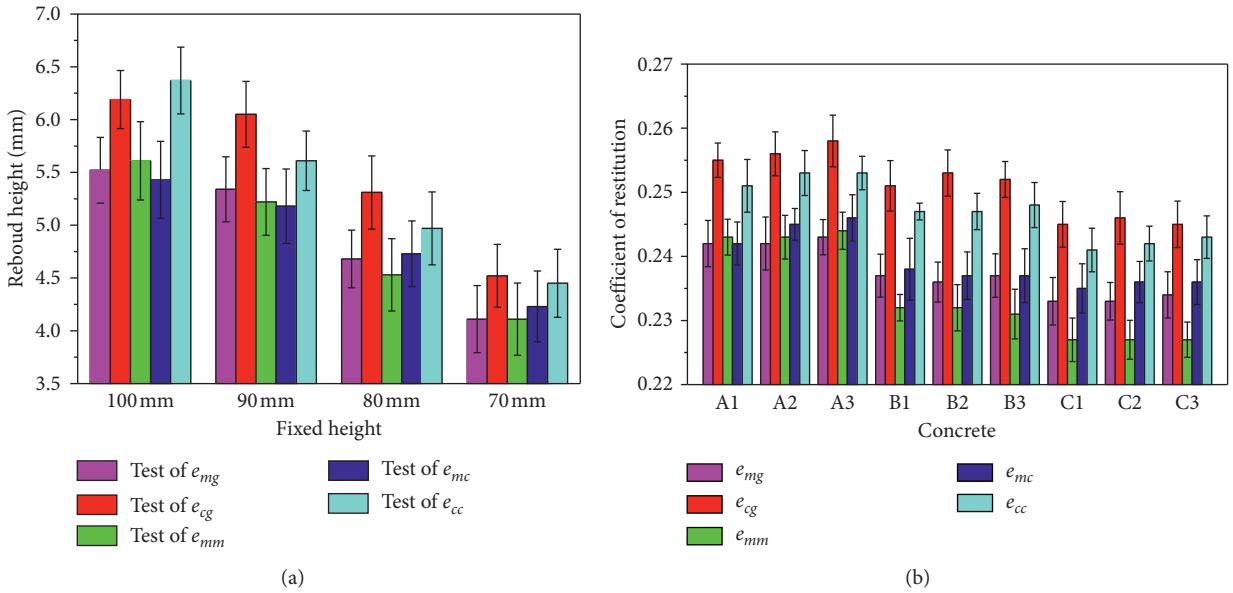

Figure 12: The test results of restitution coefficient. (a) The restitution coefficient test results of B1 concrete. (b) The restitution coefficient test results of nine kinds of concrete.

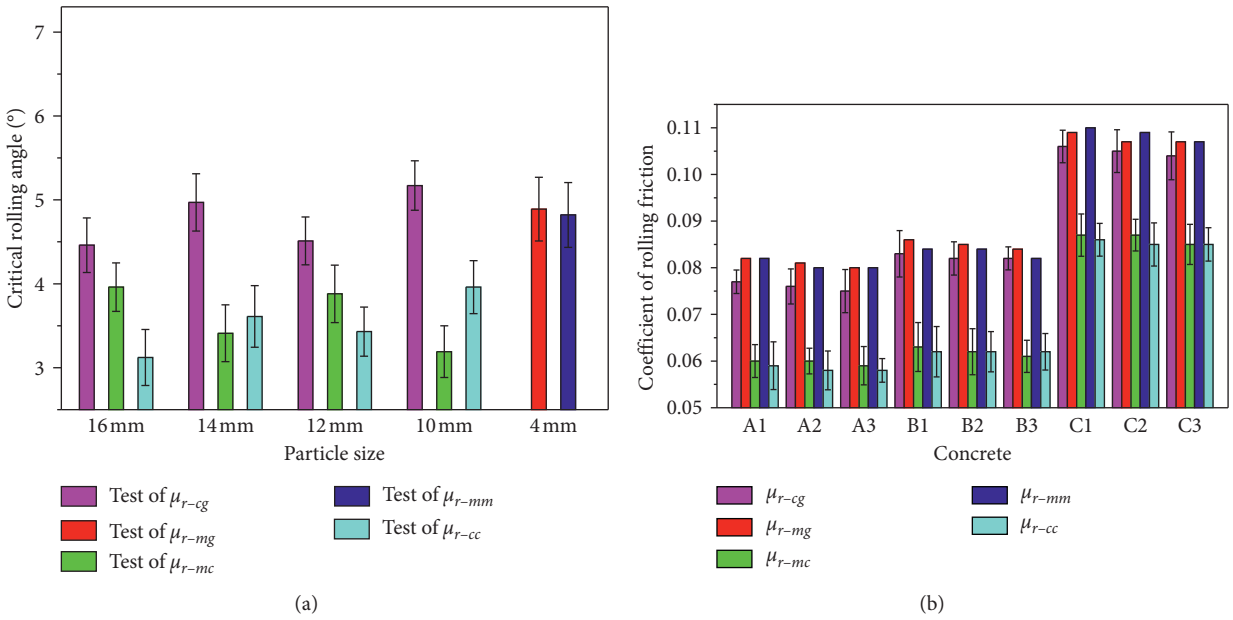

Figure 13: The test results of rolling friction coefficient. (a) The rolling friction coefficient test results of B1 concrete. (b) The rolling friction coefficient test results of nine kinds of concrete.

contact parameters of CAP-MP, CAP-CAP, MP-MP, CAP-geometry, and MP-geometry. Finally, the CAP and MP of concrete were generated in the slump cone.

3.4.2. DEM Model of Pumping Concrete. In the process of concrete entering from the horizontal pipe through the curved pipe to the vertical pipe, the flow pattern of concrete particles in the pump pipe changes greatly. In this paper, the local pumping test was selected for DEM simulation to study the flow behavior of concrete in the process of passing through the bend pipe. The pumping concrete model based on DEM with detailed configuration is shown in Figure 16. The pump pipe consisted of a horizontal pipe that is 3200 mm long, a vertical pipe that is 1200 mm high, and a 90-degree bend pipe (the bending radius of the pipe was 350 mm). The inner diameter of pump pipe was 100 mm, and the length of concrete in pump pipe was 935 mm. A piston was set at the entrance of the horizontal pipe. In this paper, the piston was used to push the concrete to realize the

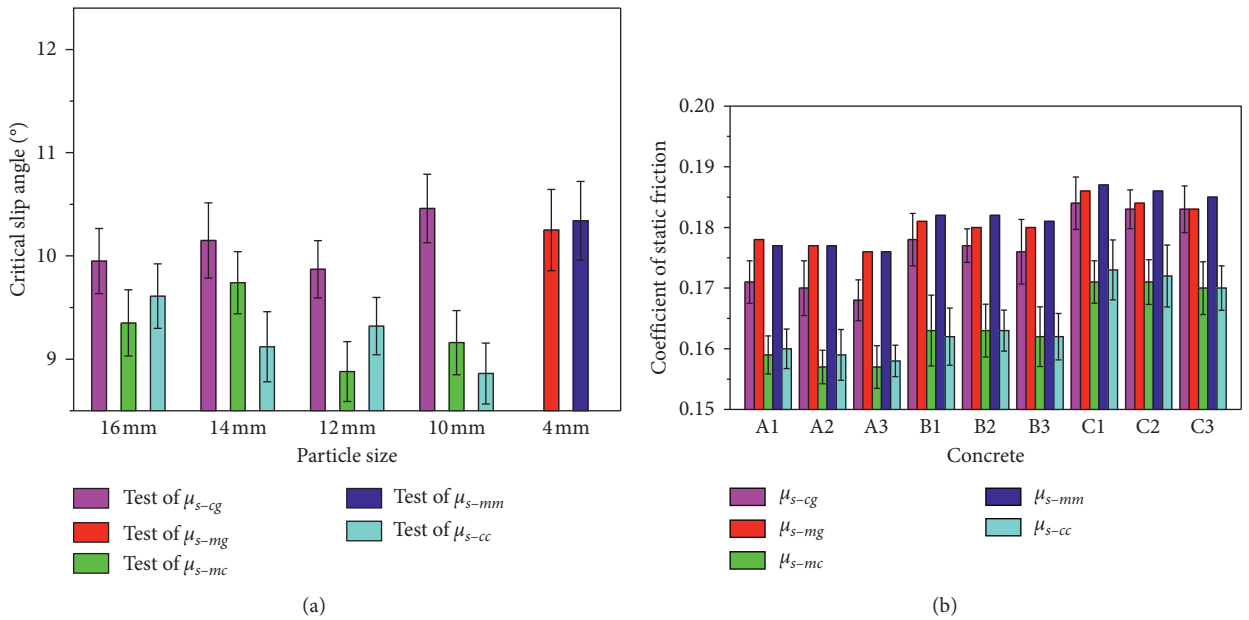

Figure 14: The test result of static friction coefficient. (a) The static friction coefficient test results of B1 concrete. (b) The static friction coefficient test results of nine kinds of concrete.

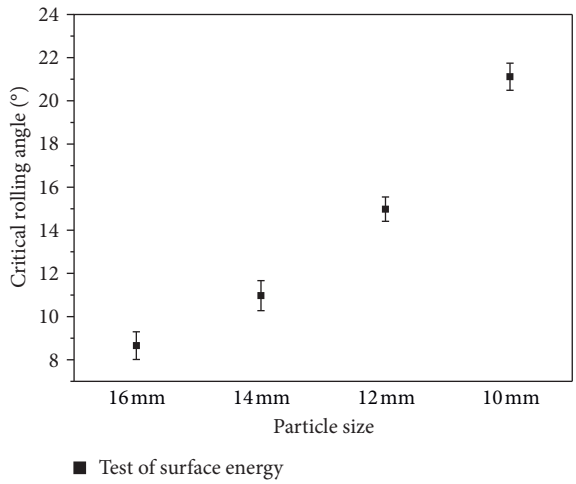

Figure 15: The test results of critical rolling angle of B1 concrete.

pumping behavior in the pump pipe. The trajectory of the piston is shown in the "pumping direction" in the figure. In this paper, the pumping concrete simulation was carried out at the speed of 0.53 m/s and 0.71 m/s, and the corresponding pumping flow was 15 m^3/h and 20 m^3/h.

4. DEM Simulation Results of Concrete Fluidity

4.1. DEM Simulation Results of Slump Test. The slump cone in DEM was lifted upward at the speed of 0.06 m/s. Figure 17 shows the process of B1 concrete slump test simulated by DEM. The simulation process of slump DEM can be divided into three stages: when the slump cone started to lift off, the inertial force and cohesive force between concrete particles limited the flow speed of concrete, and the concrete flowed slowly; then, the gravitational potential energy of concrete in the slump cone was rapidly converted into kinetic energy, and the concrete flowed rapidly; finally, under the influence of the friction force of slump plate and the cohesion between particles, the flow velocity of concrete gradually decreased and tended to be stable. The three stages of DEM simulation were highly consistent with the test process.

The simulation results of concrete slump and slump-flow are shown in Table 8. Compared with the slump test results, the relative errors of the slump simulation values were 0.45%, 0.00%, 0.44%, 0.46%, 0.00%, 0.89%, 0.00%, 0.47%, and 0.46%; the relative errors of slump-flow simulation values were 0.54%, 0.18%, 0.35%, 0.18%, 0.18%, 0.20%, 0.19%, 0.19%, and 0.00%. The DEM simulation results of concrete slump were highly consistent with the test results, which verified the accuracy of the DEM parameter calibration method used in this paper.

4.2. DEM Simulation Results of Pumping Concrete

4.2.1. Pumping Pressure. According to the pressure of B1 concrete particles on the piston in DEM model, the pumping pressure-time curve was drawn, as shown in Figure 18. When the concrete was pumped at the speed of 0.53 m/s, the pumping pressure of concrete at the initial stage of pumping was not stable; after 0.2 s, the pumping pressure of concrete was basically stable, and the average pumping pressure at this stage was 0.0431 MPa; at 4.27 s, the concrete particles began to enter the bend pipe, and the pumping pressure increased rapidly; after 5.31 s, the concrete began to pump out of the bend pipe and into the vertical pipe, and the pumping pressure fluctuated in a relatively large range (the average pumping pressure was 0.4572 MPa); after 6.04 s, the concrete began to pass through the bend pipe completely, and the pumping pressure decreased slowly; after 7.08 s, the

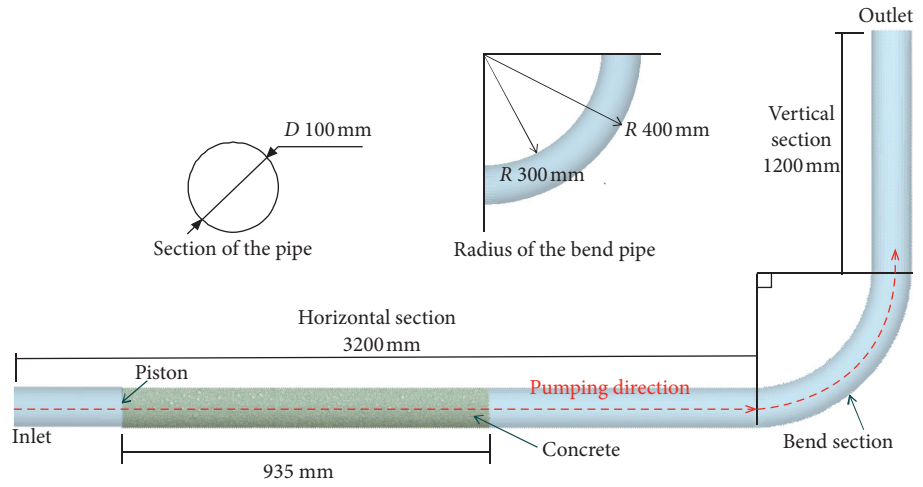

Figure 16: DEM model of pumping concrete.

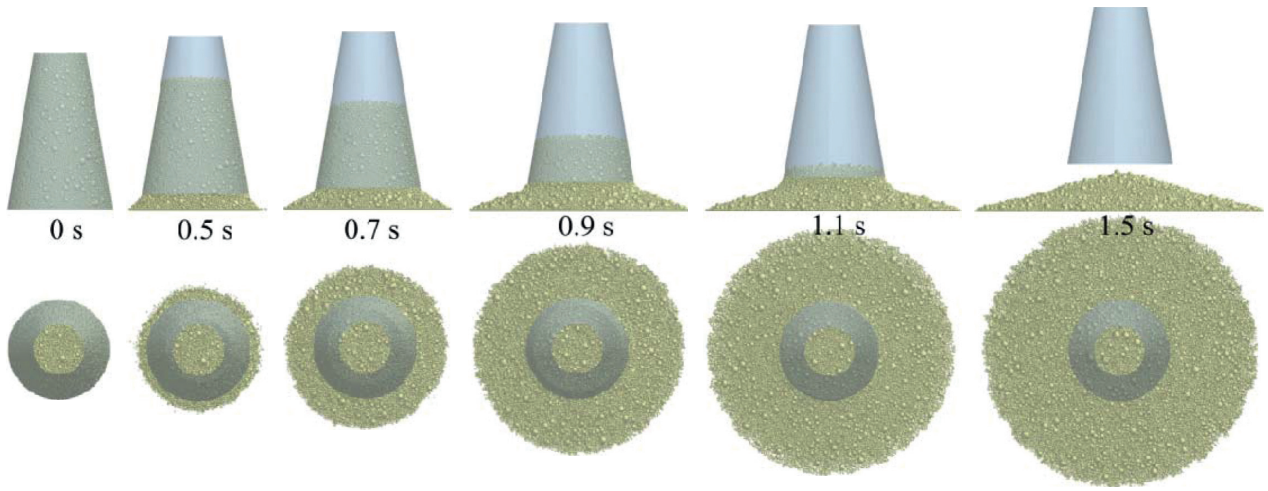

Figure 17: Slump DEM simulation of B1 concrete.

Table 8: Simulation results of slump and slump-flow of fresh concrete (mm).

	A1	A2	A3	B1	B2	B3	C1	C2	C3
Slump	223	224	225	220	221	222	212	214	218
Slump-flow	558	560	563	550	552	552	513	517	522

concrete completely entered the vertical pipe, and the pumping pressure was relatively stable, with the average pumping pressure of 0.2685 MPa. The pumping pressure-time curve of concrete pumping speed of 0.71 m/s was similar to that of pumping speed of 0.53 m/s. The average pumping pressure of concrete with pumping speed of 0.71 m/s in horizontal pipe, bend pipe, and vertical pipe was 0.0505 MPa, 0.5460 MPa, and 0.2949 MPa, respectively. The pumping pressure of concrete with pumping speed of 0.71 m/s in horizontal pipe, bend pipe, and vertical pipe increased by 0.0074 MPa, 0.0888 MPa, and 0.0264 MPa, respectively. The pumping pressure of concrete in the horizontal pipe was converted into pressure loss per meter (MPa/m), as shown in Table 7.

According to the rheological test results of concrete and lubricating layer in Table 6, the pumping pressure P (Pa) of concrete in pump pipe was calculated by (13) [52, 53] with the values shown in Table 7:

$$P = \frac{2L}{R}\left[\tau_{0LL} + \frac{Q/\pi R^2 k - R/4\mu\tau_{0LL} + R/3\mu\tau_0}{1 + R/4\mu \cdot \mu_{LL}/e} \cdot \frac{\mu_{LL}}{e}\right], \quad (13)$$

where τ_{0LL} is the interface yield stress measured with a "tribometer", Pa; τ_0 is the yield stress of the bulk concrete, Pa; μ is plastic viscosity of the bulk concrete measured by the viscometer, Pa·s; μ_{LL} is theoretical plastic viscosity of the lubricating layer, Pa·s; e is thickness of the lubricating layer, the value equal to 3 mm [36, 54], mm; k represents the pipe-filling coefficient; R is the pipe radius, m; L is the pipe length, m; Q is the pumping flow rate of concrete, m^3/s.

According to the pumping pressure difference of pressure sensors I and II in the pumping test in Figure 4, the pumping pressure loss of the horizontal pipe was calculated, as shown in Table 7. The amount of cementitious material, water consumption, and pumping speed had great influence

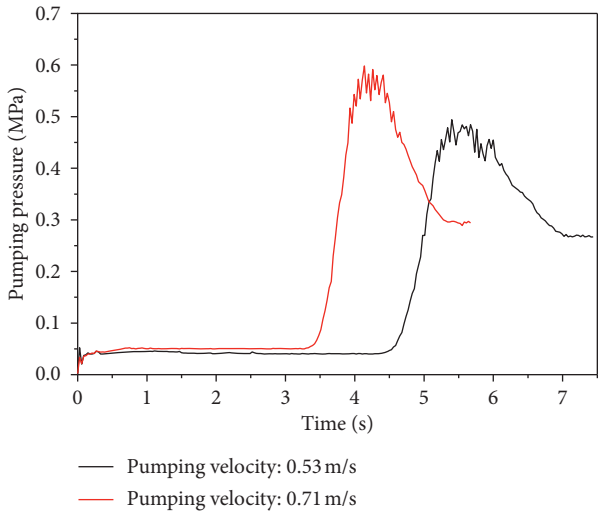

Figure 18: The DEM simulation results of B1 concrete pumping pressure.

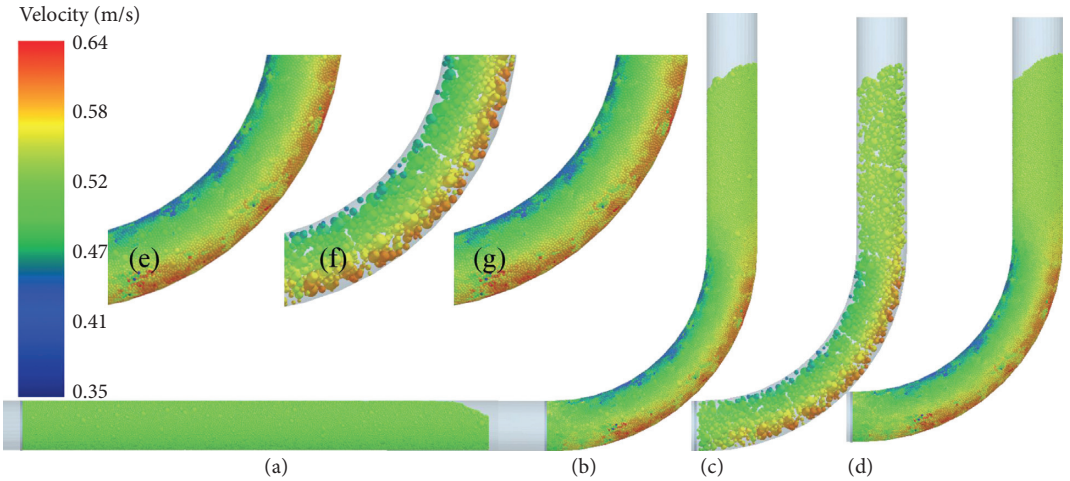

Figure 19: Velocity distribution nephogram of B1 concrete in pump pipe. (a) Concrete in horizontal pipe. (b) Concrete in bend pipe. (c) CAP in bend pipe. (d) MP in bend pipe. (e), (f), and (g) are local enlarged views of (b), (c), and (d), respectively.

on the pumping pressure of concrete, while the content of coarse aggregate had little effect on the pumping pressure of concrete. The relative error between the simulation value and the test result was 4.59%, and the relative error between the calculated value and the test result was 152.71%. The simulation result was obviously better than the calculation value.

4.2.2. Movement Behavior Analysis of Aggregate in Pump Pipe. The velocity distribution nephogram of B1 concrete with pumping speed of 0.53 m/s in the pump pipe is shown in Figure 19. In the horizontal pipe, the flow velocities of CAP and MP were basically the same; see Figure 19(a). After the concrete entered the bend pipe, the velocity of concrete near the back of the bend pipe was higher, while that near the inner side of the bend pipe was lower (Figure 19(b)). The velocity change of CAP near the back of the bend pipe was more obvious than that of the MP, and the velocity change of the MP near the inner side of the bend pipe was more obvious than that of the CAP; see Figures 19(c) and 19(d), which changed the relative spatial distribution of the CAP in the pump pipe.

When the concrete in the pump pipe kept stable flow state, the relative spatial distribution position of particles was relatively fixed, that is, the contact number between particles kept in a relatively stable range. When the flow state of concrete in the pump pipe changed, the relative spatial distribution position of concrete particles also changed, which led to the change of the contact number between particles. In this paper, the contact number between particles was adopted to evaluate the flow state of concrete in the pump pipe. Figure 20 shows the flow state of CAP and MP in the pump pipe of B1 concrete at the pumping speed of 0.53 m/s. Figure 20(a) shows the contact number of CAP-CAP and CAP-pipe. The state of CAP fluctuated greatly at the beginning of pumping; after 1.5 s, it gradually stabilized,

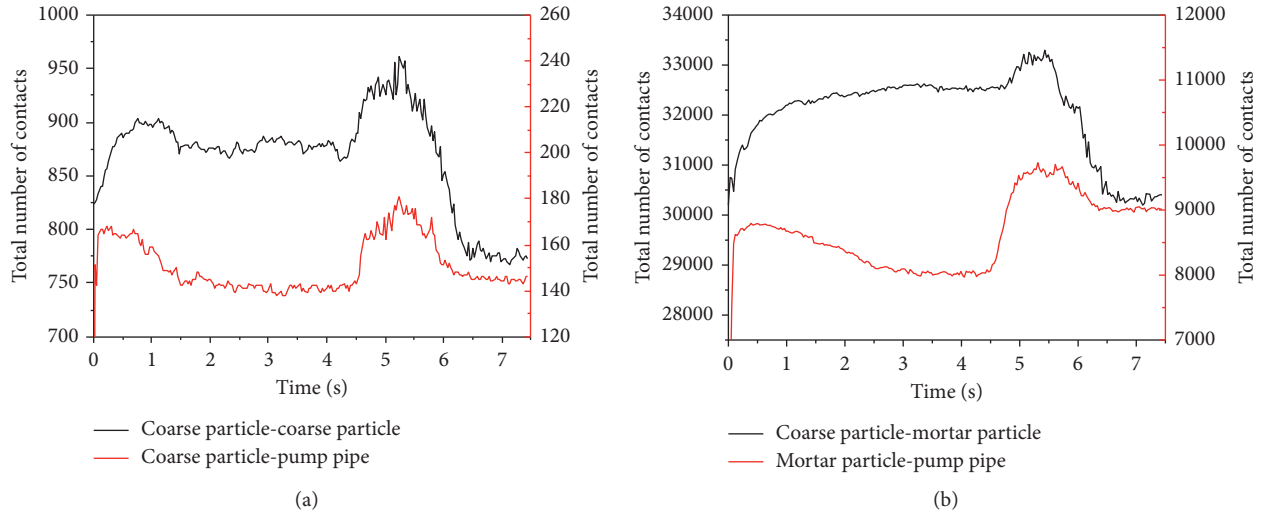

Figure 20: Contact number of B1 concrete particle in pump pipe. (a) Contact number of CAP-CAP and CAP-pump pipe. (b) Contact number of CAP-MP and MP-pipe.

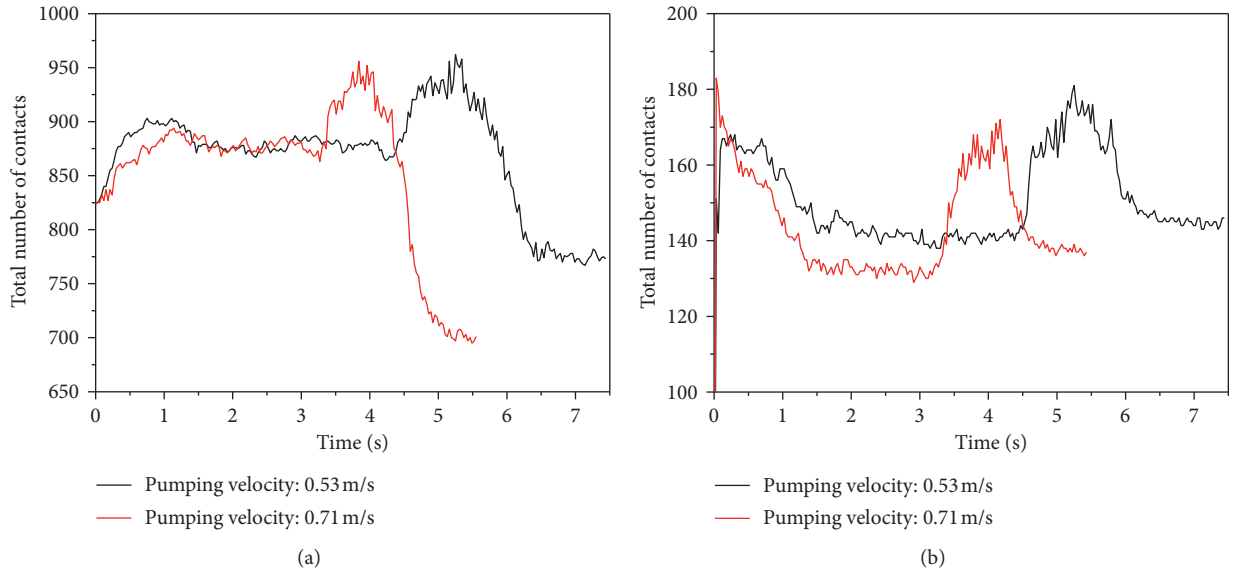

Figure 21: Influence of pumping speed on coarse aggregate movement in pump pipe. (a) Contact number of CAP-CAP. (b) Contact number of CAP-pipe.

and the average contact number of CAP-CAP was about 875; at 4.27 s, the concrete particles began to enter the bend pipe, and the contact number of CAP-CAP increased rapidly; at 5.25 s, the contact number reached the maximum value (962); after 5.31 s, the concrete began to pump out of the bend pipe, and the contact number of CAP-CAP began to decrease rapidly; after 6.04 s, the concrete began to pass through the bend completely, and the contact number decreased slowly and stably; after 7.08 s, the concrete completely entered into the vertical pipe, and the contact number of CAP-CAP was stable at about 775. The development trend of the contact number of CAP-Pipe was roughly the same as that of CAP-CAP. When the concrete passed through the bend, the contact number of CAP-pipe and CAP-CAP increased by 20.99% and 9.04%, respectively. The increase range of CAP-pipe contact number was obviously higher than that of CAP-CAP. The CAP-pipe contact number of concrete after passing through the bend pipe was slightly higher than the CAP-pipe contact number before passing through the bend pipe. However, the CAP-CAP contact number after passing through the bend was significantly lower than the CAP-CAP contact number before passing through the bend. The contact number of MP-pipe after passing through the bend was higher than that before passing through the bend, as shown in Figure 20(b). When the concrete passed through the bend pipe, the contact

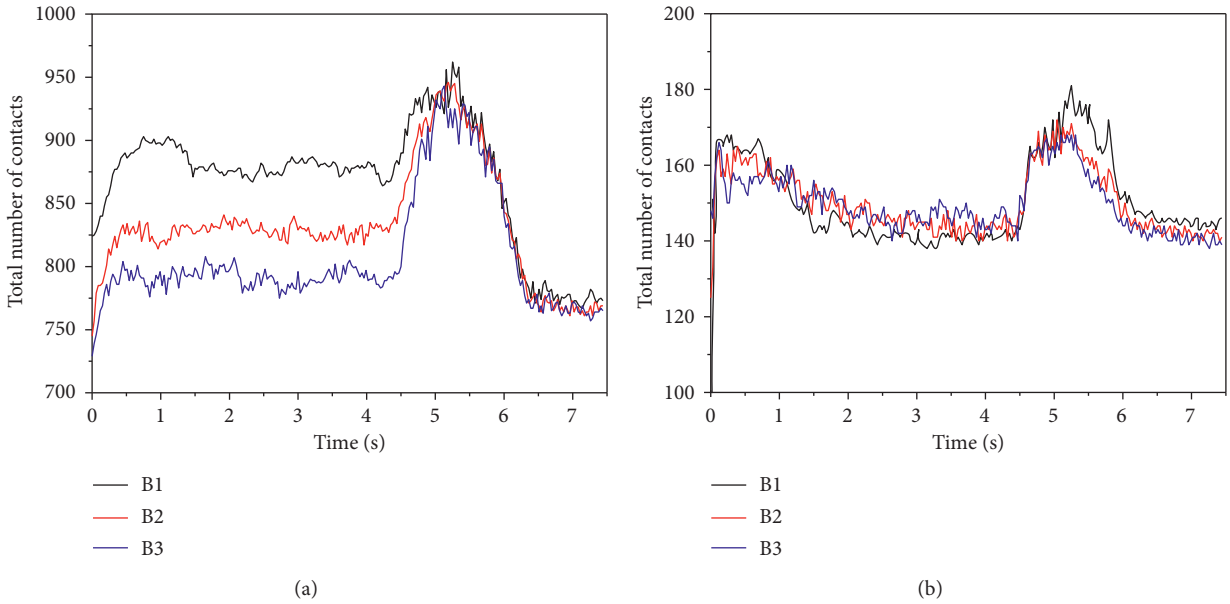

Figure 22: Influence of coarse aggregate content on aggregate movement in pump pipe. (a) Contact number of CAP-CAP. (b) Contact number of CAP-pipe.

number of CAP and MP in concrete changed rapidly, which increased the risk of uneven accumulation of coarse aggregate and pump blockage.

(1) Influence of Pumping Speed on Coarse Aggregate Movement in Pump Pipe. In the horizontal pipe, the average values of the CAP-CAP contact numbers of the B1 concrete at pumping speeds of 0.53 m/s and 0.71 m/s were 882 and 881, respectively, as shown in Figure 21(a). Under the pumping speed of 0.53 m/s and 0.71 m/s, the maximum CAP-CAP contact number of concrete at the bend was 962 and 956, respectively. The pumping speed had little effect on the CAP-CAP contact number in the horizontal pipe and bend pipe. After the concrete entered the vertical pipe from the bend pipe, the influence of pumping speed on the coarse aggregate movement behavior increased. At the pumping speed of 0.53 m/s and 0.71 m/s, the CAP-CAP contact number of concrete in the vertical pipe decreased by 18.95% and 27.37% compared with the maximum CAP-CAP contact number at the bend pipe, respectively. The pumping speed had a great influence on the CAP-pipe contact number, as shown in Figure 21(b). The CAP-pipe contact number decreased with the increase of pumping speed.

(2) Influence of Coarse Aggregate Content on Aggregate Movement in Pump Pipe. When the pumping speed was 0.53 m/s, the CAP-CAP contact number of concrete with different coarse aggregate content in the horizontal pipe and in the bend pipe displayed a large difference, as shown in Figure 22(a). The CAP-CAP contact numbers of B1, B2, and B3 concrete in horizontal pipes were 876, 836, and 798, respectively. The CAP-CAP contact numbers decreased with the decrease of coarse aggregate content. After the concrete entered the bend pipe, the CAP-CAP contact numbers of B1, B2, and B3 concrete increased by 19.36%, 13.16%, and 18.17%, respectively. After passing through the bend, the CAP-CAP contact number of the three concretes showed similar changes. When the concrete with different content of coarse aggregate was pumped horizontally, the spatial distribution position of coarse aggregate in the pump pipe was related to the content of coarse aggregate. When the concrete passed through the elbow, the spatial distribution position of coarse aggregate in the pump pipe changed greatly, and this change of distribution position was not affected by the content of coarse aggregate.

The change trend of CAP-Pipe contact number of concrete with different coarse aggregate content was basically the same, as shown in Figure 22(b). The CAP-pipe contact numbers of B1, B2, and B3 concrete in the horizontal pipe were 141, 144, and 148. In the bend pipe, the maximum CAP-pipe contact numbers of B1, B2, and B3 concrete were 181, 172, and 168. The CAP-pipe contact numbers of B1, B2, and B3 concrete in the vertical pipe were 144, 141, and 139, respectively. On the whole, the content of coarse aggregate had little effect on the CAP-pipe contact number.

5. Conclusions

In this paper, high-precision glass sphere was used as aggregate to prepare fresh concrete. And then slump test, rheological test, and pumping test were carried out, and the slump test and pumping test of concrete were accurately simulated by DEM. Firstly, glass aggregate was used to calibrate the contact parameters of concrete DEM model, and then the slump DEM model was established to verify the reliability of mesocalibration test. Finally, the DEM model of concrete pumping was established, and the influence of pumping speed and aggregate content on concrete pumping was analyzed. According to the test and simulation results, the following conclusions are obtained:

(1) The influence of high-precision glass coarse aggregate content on slump, rheological properties, and pumping performance of concrete was less than that of cementitious materials and water-binder ratio.

(2) By comparing the slump simulation results with the test results, the mesocalibration test method in this paper can accurately establish the quantitative relationship between concrete mix ratio and DEM contact parameters.

(3) The pumping pressure of concrete simulated by DEM was similar to the test results, and its accuracy was better than that calculated by the rheological properties of concrete and lubricating layer. Moreover, the concrete DEM model can well describe the flow behavior of concrete particles in the pump pipe.

Data Availability

The data used to support the findings of this study are included within the article.

Conflicts of Interest

The authors declare that they have no conflicts of interest.

Acknowledgments

The authors would like to acknowledge the financial support by the National Natural Science Foundation of China (51808015) and National Key R&D Program of China (2017YFB0310100).

References

[1] E. Secrieru, D. Cotardo, V. Mechtcherine, L. Lohaus, C. Schröfl, and C. Begemann, "Changes in concrete properties during pumping and formation of lubricating material under pressure," *Cement and Concrete Research*, vol. 108, pp. 129–139, 2018.

[2] E. Secrieru, W. Mohamed, S. Fataei, and V. Mechtcherine, "Assessment and prediction of concrete flow and pumping pressure in pipeline," *Cement and Concrete Composites*, vol. 107, p. 103495, 2020.

[3] G. Liu, W. Cheng, L. Chen, G. Pan, and Z. Liu, "Rheological properties of fresh concrete and its application on shotcrete," *Construction and Building Materials*, vol. 243, p. 118180, 2020.

[4] M. S. Choi, Y. J. Kim, K. P. Jang, and S. H. Kwon, "Effect of the coarse aggregate size on pipe flow of pumped concrete," *Construction and Building Materials*, vol. 66, pp. 723–730, 2014.

[5] D. Feys, G. De Schutter, K. H. Khayat, and R. Verhoeven, "Changes in rheology of self-consolidating concrete induced by pumping," *Materials and Structures*, vol. 49, no. 11, pp. 4657–4677, 2016.

[6] Y. W. D. Tay, Y. Qian, and M. J. Tan, "Printability region for 3D concrete printing using slump and slump flow test," *Composites Part B: Engineering*, vol. 174, p. 106968, 2019.

[7] R. J. Myers, G. Geng, J. Li et al., "Role of adsorption phenomena in cubic tricalcium aluminate dissolution," *Langmuir*, vol. 33, no. 1, pp. 45–55, 2017.

[8] C. Karakurt, A. O. Çelik, C. Yılmazer, V. Kiriççi, and E. Özyaşar, "CFD simulations of self-compacting concrete with discrete phase modeling," *Construction and Building Materials*, vol. 186, pp. 20–30, 2018.

[9] V. N. Nerella, F. Galvani, L. Ferrara, and V. Mechtcherine, "Normal and tangential interaction between discrete particles immersed in viscoelastic fluids: experimental investigation as basis for Discrete Element Modelling of fresh concrete," in *Proceedings of the 8th International RILEM Symposium on Self-Compacting Concrete - SCC 2016*, Washingston, DC, USA, May 2016.

[10] V. Mechtcherine, F. P. Bos, A. Perrot et al., "Extrusion-based additive manufacturing with cement-based materials - production steps, processes, and their underlying physics: a review," *Cement and Concrete Research*, vol. 132, p. 106037, 2020.

[11] P. J. M. Monteiro, G. Geng, D. Marchon et al., "Advances in characterizing and understanding the microstructure of cementitious materials," *Cement and Concrete Research*, vol. 124, Article ID 105806, 2019.

[12] H. Hoornahad and E. A. B. Koenders, "Tracking the rheological behavior change of a fresh granular-cement paste material to a granular material based on DEM," *Advanced Materials Research*, vol. 446–449, pp. 3803–3809, 2012.

[13] V. Mechtcherine and S. Shyshko, "Simulating the behaviour of fresh concrete with the Distinct Element Method - deriving model parameters related to the yield stress," *Cement and Concrete Composites*, vol. 55, pp. 81–90, 2015.

[14] S. Shyshko and V. Mechtcherine, "Developing a Discrete Element Model for simulating fresh concrete: experimental investigation and modelling of interactions between discrete aggregate particles with fine mortar between them," *Construction and Building Materials*, vol. 47, pp. 601–615, 2013.

[15] S. Remond and P. Pizette, "A DEM hard-core soft-shell model for the simulation of concrete flow," *Cement and Concrete Research*, vol. 58, pp. 169–178, 2014.

[16] H. Hoornahad and E. A. B. Koenders, "Simulating macroscopic behavior of self-compacting mixtures with DEM," *Cement and Concrete Composites*, vol. 54, pp. 80–88, 2014.

[17] Z. Li, G. Cao, and K. Guo, "Numerical method for thixotropic behavior of fresh concrete," *Construction and Building Materials*, vol. 187, pp. 931–941, 2018.

[18] G. Cao, Z. Li, and K. Guo, "Analytical study on the change of fluidity of fresh concrete containing mineral admixture with rest time," *Journal of Advanced Concrete Technology*, vol. 15, no. 11, pp. 713–723, 2017.

[19] X. Zhang, Z. Zhang, Z. Li, Y. Li, and T. Sun, "Filling capacity analysis of self-compacting concrete in rock-filled concrete based on DEM," *Construction and Building Materials*, vol. 233, p. 117321, 2020.

[20] Y. Zhan, J. Gong, Y. Huang, C. Shi, Z. Zuo, and Y. Chen, "Numerical study on concrete pumping behavior via local flow simulation with discrete element method," *Materials*, vol. 12, no. 9, pp. 1415–1435, 2019.

[21] Y. Tan, G. Cao, H. Zhang et al., "Study on the thixotropy of the fresh concrete using DEM," *Procedia Engineering*, vol. 102, pp. 1944–1950, 2015.

[22] W. Cui, W.-s. Yan, H.-f. Song, and X.-l. Wu, "Blocking analysis of fresh self-compacting concrete based on the DEM," *Construction and Building Materials*, vol. 168, pp. 412–421, 2018.

[23] W. Cui, T. Ji, M. Li, and X. Wu, "Simulating the workability of fresh self-compacting concrete with random polyhedron

aggregate based on DEM," *Materials and Structures*, vol. 50, no. 1, pp. 1–12, 2016.

[24] G. Cao, H. Zhang, Y. Tan et al., "Study on the effect of coarse aggregate volume fraction on the flow behavior of fresh concrete via DEM," *Procedia Engineering*, vol. 102, pp. 1820–1826, 2015.

[25] M. A. Haustein, G. Zhang, and R. Schwarze, "Segregation of granular materials in a pulsating pumping regime," *Granular Matter*, vol. 21, no. 4, 2019.

[26] C. J. Coetzee, "Review: calibration of the discrete element method," *Powder Technology*, vol. 310, pp. 104–142, 2017.

[27] S. Shyshko and V. Mechtcherine, "Simulating the workability of fresh concrete," in *Proceedings of the International RILEM Symposium on Concrete Modelling*, pp. 173–181, Beijing, China, October 2008.

[28] M. Rackl and K. J. Hanley, "A methodical calibration procedure for discrete element models," *Powder Technology*, vol. 307, pp. 73–83, 2017.

[29] C. J. Coetzee, "Calibration of the discrete element method and the effect of particle shape," *Powder Technology*, vol. 297, pp. 50–70, 2016.

[30] T. Roessler and A. Katterfeld, "DEM parameter calibration of cohesive bulk materials using a simple angle of repose test," *Particuology*, vol. 45, pp. 105–115, 2019.

[31] X. Zhang, Z. Li, Z. Zhang, and Y. Li, "Discrete element analysis of the rheological characteristics of self-compacting concrete with irregularly shaped aggregate," *Arabian Journal of Geosciences*, vol. 11, no. 19, pp. 1–17, 2018.

[32] W. Cui, W.-s. Yan, H.-f. Song, and X.-l. Wu, "DEM simulation of SCC flow in L-Box set-up: influence of coarse aggregate shape on SCC flowability," *Cement and Concrete Composites*, vol. 109, p. 103558, 2020.

[33] U. Zafar, C. Hare, A. Hassanpour, and M. Ghadiri, "Drop test: a new method to measure the particle adhesion force," *Powder Technology*, vol. 264, pp. 236–241, 2014.

[34] B. M. Ghodki, M. Patel, R. Namdeo, and G. Carpenter, "Calibration of discrete element model parameters: soybeans," *Computational Particle Mechanics*, vol. 6, no. 1, pp. 3–10, 2018.

[35] S. H. Kwon, K. P. Jang, J. H. Kim, and S. P. Shah, "State of the art on prediction of concrete pumping," *International Journal of Concrete Structures and Materials*, vol. 10, no. S3, pp. 75–85, 2016.

[36] D. Feys, K. H. Khayat, A. Perez-Schell, and R. Khatib, "Development of a tribometer to characterize lubrication layer properties of self-consolidating concrete," *Cement and Concrete Composites*, vol. 54, pp. 40–52, 2014.

[37] K. L. Johnson, K. Kendall, and A. D. Roberts, "Surface energy and the contact of elastic solids," *Proceedings of The Royal Society A*, vol. 324, no. 1558, pp. 301–313, 1971.

[38] A. V. Rahul, M. Santhanam, H. Meena, and Z. Ghani, "3D printable concrete: Mixture design and test methods," *Cement and Concrete Composites*, vol. 97, pp. 13–23, 2019.

[39] K. El Cheikh, S. Rémond, N. Khalil, and G. Aouad, "Numerical and experimental studies of aggregate blocking in mortar extrusion," *Construction and Building Materials*, vol. 145, pp. 452–463, 2017.

[40] Z. Zhang, Y. Cui, D. H. Chan, and K. A. Taslagyan, "DEM simulation of shear vibrational fluidization of granular material," *Granular Matter*, vol. 20, no. 4, pp. 1–20, 2018.

[41] X. Gu, L. Lu, and J. Qian, "Discrete element modeling of the effect of particle size distribution on the small strain stiffness of granular soils," *Particuology*, vol. 32, pp. 21–29, 2017.

[42] G. K. P. Barrios, R. M. de Carvalho, A. Kwade, and L. M. Tavares, "Contact parameter estimation for DEM simulation of iron ore pellet handling," *Powder Technology*, vol. 248, pp. 84–93, 2013.

[43] Y. Li, J. Hao, C. Jin, Z. Wang, and J. Liu, "Simulation of the flowability of fresh concrete by discrete element method," *Frontiers in Materials*, vol. 7, 2021.

[44] A. P. Grima, *Quantifying and Modelling Mechanisms of Flow in Cohesionless and Cohesive Granular Materials*, University of Wollongong, Wollongong, Australia, 2011.

[45] J. Ai, J.-F. Chen, J. M. Rotter, and J. Y. Ooi, "Assessment of rolling resistance models in discrete element simulations," *Powder Technology*, vol. 206, no. 3, pp. 269–282, 2011.

[46] S. K. Wilkinson, S. A. Turnbull, Z. Yan, E. H. Stitt, and M. Marigo, "A parametric evaluation of powder flowability using a Freeman rheometer through statistical and sensitivity analysis: a discrete element method (DEM) study," *Computers & Chemical Engineering*, vol. 97, pp. 161–174, 2017.

[47] E. Murphy and S. Subramaniam, "Binary collision outcomes for inelastic soft-sphere models with cohesion," *Powder Technology*, vol. 305, pp. 462–476, 2017.

[48] H. Hoornahad and E. A. B. Koenders, "Towards simulation of fresh granular-cement paste material behavior," *Advanced Materials Research*, vol. 295–297, pp. 2171–2177, 2011.

[49] J. H. Lee, J. H. Kim, and J. Y. Yoon, "Prediction of the yield stress of concrete considering the thickness of excess paste layer," *Construction and Building Materials*, vol. 173, pp. 411–418, 2018.

[50] ASTM C29/C29M, *Standard Test Method for Bulk Density and Voids in Aggregate*, ASTM C29/C29M, West Conshohocken, PA, USA, 1997.

[51] N. S. Klein, S. Cavalaro, A. Aguado, I. Segura, and B. Toralles, "The wetting water in cement-based materials: modeling and experimental validation," *Construction and Building Materials*, vol. 121, pp. 34–43, 2016.

[52] H. D. Le, E. H. Kadri, S. Aggoun, J. Vierendeels, P. Troch, and G. De Schutter, "Effect of lubrication layer on velocity profile of concrete in a pumping pipe," *Materials and Structures*, vol. 48, no. 12, pp. 3991–4003, 2015.

[53] E. Secrieru, J. Khodor, C. Schröfl, and V. Mechtcherine, "Formation of lubricating layer and flow type during pumping of cement-based materials," *Construction and Building Materials*, vol. 178, pp. 507–517, 2018.

[54] D. Kaplan, F. d. Larrard, and T. Sedran, "Design of concrete pumping circuit," *ACI Materials Journal*, vol. 102, pp. 100–117, 2005.